Design of Highly Efficient Nanoparticle Assisted Antireflection Coatings for Solar Cells

Doctoral Thesis (Dissertation)

to be awarded the degree

Doctor rerum naturalium (Dr. rer. nat.)

submitted by

Bhaskar Singh
from Adda Bazar, India

approved by the Faculty of Natural and Material Sciences
Clausthal University of Technology

Date of oral examination

29.01.2021

Dean

Prof. Dr.-Ing. habil. Karl-Heinz Spitzer

Chairperson of the Board of Examiners

Prof. Dr. Sabine Beuermann

Supervising tutor

Prof. Dr. Daniel M. Schaadt

Reviewer

Prof. Dr.-Ing. habil. Joachim Deubener

ABSTRACT

Solar cells suffer a loss in efficiency due to the front surface reflection of the incident sunlight. To reduce this loss, an antireflection coating (ARC) is typically used. However, the conventional thin-film ARC in the solar cell is generally optimized for a single wavelength at a normal angle of incidence (AOI). On the contrary, a fixed solar cell on the roof receives the sunlight over a wide range of AOI resulting in an undesired loss of light photons. To overcome this issue, nanoparticles (NPs), which scatter the sunlight, have been suggested.

The scattering and absorption in metal NPs (Ag, Au, Cu, and Al) are highly influenced by their shape, size, and material composition, host medium, and volume fraction of NPs in the medium itself. The metal NPs scatter the sunlight efficiently at the resonance wavelength. An analytical framework, based on the transfer matrix method (TMM) and Mie theory, has been used in this thesis to study and optimize the scattering property of metal NPs. This simulation study also enables the power transfer from the metal NPs layer into a substrate layer. A comparative analysis between the performance of NPs and the bare substrate layer revealed that NPs based structures, which show high backscattering, are not suitable at the front for high power transfer in the substrate layer. Furthermore, Al – and Ag – NPs show high radiation in the substrate layer which increases with NPs' size in the visible range. This high radiation property of the NPs allows for significant improvements in the power transfer at a wide range of AOI.

The photon density in the solar cell is usually optimized through tailored ARCs. I develop another analytical model and present it in this thesis work to describe NPs based hybrid ARC, where NPs are embedded in a conventional thin-film ARC (SiN) on a substrate layer. A point dipole approach is implemented to calculate diffuse reflectance by NPs, while the TMM method is used for specular reflectance from the front surface. The simulation results show that embedding metal NPs in SiN ARC enhances the antireflection property in comparison to the conventional ARC at non-normal AOI of the sunlight. Electric field distribution patterns of radiation in the substrate layer by a single NP are also calculated for various AOI which support the improvements in the antireflection property. Weighted solar power transmittances from ARCs obtained from the model demonstrate that Ag – NPs

embedded in SiN ARC performs better than SiN ARC for AOI > 74°, whereas Al – NPs based ARC performs better for AOI > 78°. The metal NPs based hybrid ARC were shown less efficient at normal and near-normal AOI. This is caused by parasitic absorption in the metal NPs. Since it's well known that dielectric NPs don't show this behavior in a narrow band spectrum range, hence I replaced the metal NPs with dielectric NPs and performed the same analysis with non-absorbing spherical dielectric (SiO_2) NPs. This new hybrid ARC design leads to enhanced antireflection property at non-normal incidence while showing insignificant change at normal and near-normal incidence. The highest improvement is noticed more than a factor of two at 85° AOI with the NPs' surface filling density of 70 %. Finally, I perform sunrise to sunset calculation of the normalized photocurrent density over the course of a year for five selected cities, which have also shown improvements in the SiO_2 – NPs' case.

ZUSAMMENFASSUNG

Solarzellen erleiden Effizienzverluste aufgrund der Reflexion des einfallenden Sonnenlichts an der Vorderseite. Um diesen Verlust zu verringern, wird üblicherweise eine Antireflexbeschichtung (ARC) verwendet. Die konventionelle Dünnschicht-ARC in der Solarzelle ist jedoch im Allgemeinen für eine einzige Wellenlänge bei normalem Einfallswinkel (AOI) optimiert. Im Gegensatz dazu empfängt eine feststehende Solarzelle auf dem Dach das Sonnenlicht über einen breiten Bereich von AOI, was zu einem unerwünschten Verlust von Lichtphotonen führt. Um dieses Problem zu lösen, wurden Nanopartikel (NPs) vorgeschlagen, die das Sonnenlicht streuen.

Die Streuung und Absorption in metallischen NPs (Ag, Au, Cu und Al) wird stark von ihrer Struktur, Größe und Materialzusammensetzung, dem Wirtsmedium und dem Volumenanteil der NPs im Medium selbst beeinflusst. Die metallischen NPs streuen das Sonnenlicht effizient bei der Resonanzwellenlänge. Ein analytischer Rahmen, der auf der Transfer-Matrix-Methode (TMM) und der Mie-Theorie basiert, wurde in dieser Doktorarbeit verwendet, um die Streueigenschaften von Metall-NPs zu untersuchen und zu optimieren. Diese Simulationsstudie ermöglicht auch den Leistungstransfer von der Metall-NPs-Schicht in eine Substratschicht. Eine vergleichende Analyse zwischen der Leistung von NPs und der blanken Substratschicht ergab, dass Strukturen auf NPs-Basis, die eine hohe Rückstreuung aufweisen, an der Vorderseite nicht für eine hohe Leistungsübertragung in der Substratschicht geeignet sind. Außerdem zeigen Al - und Ag - NPs eine hohe Strahlung in der Substratschicht, die mit der Größe der NPs im sichtbaren Bereich zunimmt. Diese hohe Strahlungseigenschaft der NPs ermöglicht signifikante Verbesserungen bei der Leistungsübertragung in einem weiten AOI-Bereich.

Die Photonendichte in der Solarzelle wird in der Regel durch maßgeschneiderte ARCs optimiert. Ich entwickle ein weiteres analytisches Modell und stelle in dieser Doktorarbeit vor, um auf NPs basierende hybride ARCs zu beschreiben, bei denen NPs in eine konventionelle Dünnschicht-ARC (SiN) auf einer Substratschicht eingebettet sind. Ein Punkt-Dipol-Ansatz wird implementiert, um die diffuse Reflexion durch NPs zu berechnen, während die TMM-Methode für die spiegelnde Reflexion von der vorderen Oberfläche verwendet wird. Die Simulationsergebnisse zeigen, dass die Einbettung von Metall-NPs in SiN-ARC die Antireflexionseigenschaft im Vergleich zur

konventionellen ARC bei nicht-normalem AOI des Sonnenlichts verbessert. Die Muster der elektrischen Feldverteilung der Strahlung in der Substratschicht durch einen einzelnen NP werden auch für verschiedene AOI berechnet, was die Verbesserungen der Antireflexionseigenschaften unterstützt. Die aus dem Modell gewonnenen gewichteten Solarleistungs-Transmissionswerte von ARCs zeigen, dass Ag - NPs, die in SiN ARC eingebettet sind, bei AOI > 74° besser abschneiden als SiN ARC, während ARC auf Al - NPs basierende ARC bei AOI > 78° besser abschneiden. Die auf Metall-NPs basierenden Hybrid-ARCs waren bei normaler und nahezu normaler AOI weniger effizient. Dies wird durch parasitäre Absorption in den Metall-NPs verursacht. Da bekannt ist, dass dielektrische NPs dieses Verhalten in einem schmalbandigen Spektralbereich nicht zeigen, ersetzte ich die Metall-NPs durch dielektrische NPs und führte dieselbe Analyse mit nicht-absorbierenden sphärischen dielektrischen (SiO_2) NPs durch. Dieses neue hybride ARC-Design führt zu einer verbesserten Antireflexionseigenschaft bei nicht normalem Einfall, während es bei normalem und nahezu normalem Einfall eine unbedeutende Änderung zeigt. Die höchste Verbesserung wird bei 85° AOI mit einer Oberflächenfülldichte der NPs von 70 % um mehr als den Faktor zwei bemerkt. Schließlich führe ich eine Berechnung der normierten Photostromdichte von Sonnenaufgang bis Sonnenuntergang über den Verlauf eines Jahres für fünf ausgewählte Städte durch, die ebenfalls Verbesserungen im Fall der SiO_2 - NPs gezeigt haben.

AFFIDAVIT

Hereby, I declare that the thesis has been written by me independently and all the sources used are quoted.

Parts of this thesis and figures have been published in the following articles.

[1] *B. Singh*, M. M. Shabat, and D. M. Schaadt, "Analytical modeling of power transfer via metallic nanoparticles in a solar cell absorber," *J. Quant. Spectrosc. Radiat. Transf.*, vol. 243, p. 106807, 2020.

[2] *B. Singh*, M. M. Shabat, and D. M. Schaadt, "Wide angle antireflection in metal nanoparticles embedded in a dielectric matrix for plasmonic solar cells," *Prog. Photovoltaics Res. Appl.*, vol. 28, pp. 682–690, 2020.

[3] *B. Singh*, M. M. Shabat, and D. M. Schaadt, "Silver nanoparticle-based anti-reflection coating for solar cells," in *SPIE Photonics for Solar Energy Systems VIII*, 2020, vol. 1, no. 1, p. 11366.

[4] *B. Singh*, M. M. Shabat, and D. M. Schaadt, "Large photocurrent density enhancement assisted by non-absorbing spherical dielectric nanoparticles in a GaAs layer," *Sci. Rep.*, 10:17107, 2020.

Clausthal-Zellerfeld, 29.01.2021

CONTENTS

LIST OF FIGURES

LIST OF TABLES

ACRONYMS

Si	Silicon
GaAs	Gallium arsenide
CIGS	Copper indium gallium selenide
AM	Air mass
QE	Quantum efficiency
EQE	External quantum efficiency
IQE	Internal quantum efficiency
PFD	Photon flux density
PV	Photovoltaic
AOI	Angle of incidence
ARC	Antireflection coating
NP	Nanoparticle
TE	Transverse electric
TM	Transverse magnetic
OPD	Optical path difference
SiN	Silicon nitride
TMM	Transfer Matrix Method
FDTD	Finite-Difference Time-Domain
CVD	Chemical vapor deposition
PVD	Physical vapor deposition
LSPR	Localized surface plasmon resonance
MG	Maxwell-Garnett
2D	Two-dimensional
UV	Ultra-violet

QW	Quantum well
TCAD	Technical computer added design
FEM	Finite element modelling

1

INTRODUCTION

Sustainable energy is one of the main issues with environmental, social, economic, and political aspects. Climate change, pollution, and lack of energy security are the outcomes of the misuse of non – renewable sources (Fossil fuels) such as oil, coal, and natural gas. Besides the side effects of these sources on human health and the environment, it remains the issue of energy available for the future generation. Studies show that Fossil fuels will irreversibly start to decline within the next few decades [5]. Therefore, coupled with the demand for energy in the future, the need for renewable energy (Green energy) becomes essential.

Solar energy is one of the main sources of renewable energy which is available on an abundant scale in the earth's atmosphere. This energy can be transformed into electrical energy by using solar cells.

1.1 SOLAR CELL

A solar cell is a p-n diode that converts the sunlight directly to electricity. The cell works on photoelectric effect and semiconductor physics concepts [6]. Semiconducting materials such as Si [7], GaAs [8], $CuIn_xGa_{(1-x)}Se_2$ (or CIGS) [9], etc. are generally used to make this kind of device. Currently, one of the most important challenges in this field is the efficiency of the solar cell. The efficiency is the measurement of solar power conversion into electricity. For many decades, new technologies and new semiconducting materials are being developed and investigated by researchers to increase the efficiency of the cell [7]–[14].

1.1.1 Solar Cell Characteristics

When a solar cell is exposed to the sunlight, a photon with energy higher than the bandgap (E_g) of semiconducting material is absorbed by an electron (charge carrier) in the valance band and the electron enters in an excited state (in conduction band). The excited electron contributes to an electric charge of the cell output. The property of a solar cell is defined by four quantities such that short-circuit current density (J_{SC}), open-circuit voltage (V_{OC}), fill-factor (FF), and power conversion efficiency (η) which are obtained from the current-voltage (J-V) characteristics of the solar cell. The J-V characteristics of a solar cell is simply a superposition of p-n diode characteristics in dark and the photocurrent. The governing equation of the characteristics is given by

$$J = J_S \left[\exp\left(\frac{qV}{nkT}\right) - 1 \right] - J_{PH} \qquad (1.1)$$

where J is the total current density flowing through the solar cell; J_S is the dark saturation current density; V is the voltage across the cell terminals; q is the absolute value of electron charge; k is the Boltzmann's constant; T is the absolute temperature; n is the ideality factor and J_{PH} is the photocurrent density. A schematic of the ideal characteristic ($n = 1$) is shown in Figure 1.1.

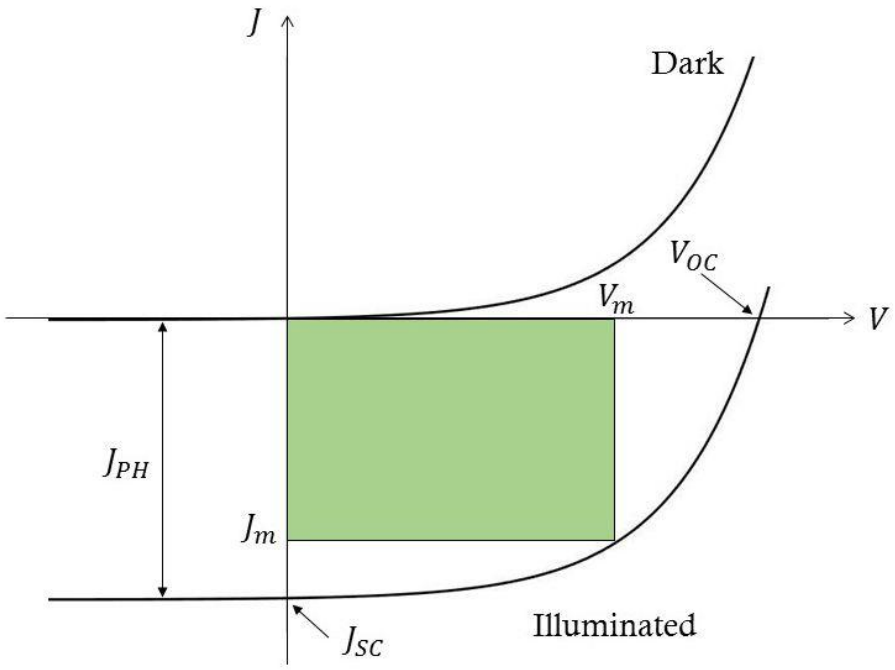

Figure 1.1 Ideal J-V characteristics of the solar cell under dark and illumination conditions.

The green shaded area in Figure 1.1 is the maximum power output from the solar cell. J_m and V_m are corresponding to the maximum power

output ($P_m = J_m * V_m$) from the solar cell. *FF* is the measure of the quality of a solar cell and is defined as

$$FF = \frac{P_m}{J_{SC} * V_{OC}} \tag{1.2}$$

The total power conversion efficiency of the solar cell is given by

$$\eta = \frac{P_m}{P_{in}} = \frac{FF * J_{SC} * V_{OC}}{P_{in}} \tag{1.3}$$

where P_{in} is the incident power on the cell. The total incident power for AM1.5 solar illumination is ~844 W/m^2.

The J-V characteristics of a solar cell depend on the semiconducting material properties, cell resistance, cell operating temperature, light intensity, and the ideality factor. The cell resistance reduces the efficiency of the solar cell by dissipating power in the resistance. These parasitic resistances are series resistance (R_S) and shunt resistance (R_{SH}). In this case, the governing equation of the J-V characteristics is found to be modified from eq. (1.1) to

$$J = J_S \left[\exp\left(\frac{q(V - JR_s)}{nkT} \right) - 1 \right] + \frac{V - JR_s}{R_{SH}} - J_{PH} \tag{1.4}$$

The increase in cell operating temperature reduces the band gap of semiconducting material. This causes a slight increase in J_{SC}, however at the same time V_{OC} decreases because of the temperature dependence of J_S. J_{SC} linearly depends on the light intensity which means if the illumination on a cell changes from 1 sun (AM1.5 illumination) to 10 suns, J_{SC} will increase 10 times. But this doesn't mean a 10 times increase in efficiency because V_{OC} increases logarithmically with the light intensity. [15]

Table 1 Charge carrier recombination type and the corresponding ideality factor. SRH: Shockley-Read-Hall

Recombination Type	Ideality factor
SRH, band to band (low-level injection)	1
SRH, band to band (high-level injection)	2
Auger recombination	0.66
Depletion region (in the junction)	2

The ideality factor (n) of a solar cell (p-n diode) is a measure of how closely the cell follows the ideal diode equation. The ideal diode equation is derived with the assumptions of charge carrier recombination such as via band to band or via traps in the bulk area of the cell (not in the junction). However, the recombination occurs in other ways too which are summarized with the corresponding ideality factor in Table 1. [16]

1.1.2 Quantum Efficiency

The quantum efficiency (QE) is the ratio of no. of charge carriers collected by the solar cell to no. of photons incident on the solar cell. This can be separated into two quantities such that external quantum efficiency (EQE) and external quantum efficiency (IQE) of the solar cell which are defined as

$$\mathrm{EQE} = \frac{no.\ of\ collected\ electrons/sec}{no.\ of\ incident\ photons/sec} \tag{1.4}$$

$$\mathrm{IQE} = \frac{no.\ of\ collected\ electrons/sec}{no.\ of\ absorbed\ photons/sec} \tag{1.5}$$

In the ideal case, $\mathrm{EQE} = \mathrm{IQE} = 1$, however, in reality, they are always less than 1.

The photocurrent density can be obtained directly from IQE as follows

$$J_{PH} = q * \int_{\lambda_g}^{\infty} A(\lambda) *\ PFD(\lambda) * IQE(\lambda)\, d\lambda \tag{1.6}$$

where λ_g is the wavelength corresponding to the band gap of semiconducting material; $PFD(\lambda)$ is the photon flux density (cf. Figure 1.2) [17] and $A(\lambda)$ is the percent of photons got absorbed in the semiconducting material corresponding the wavelength λ.

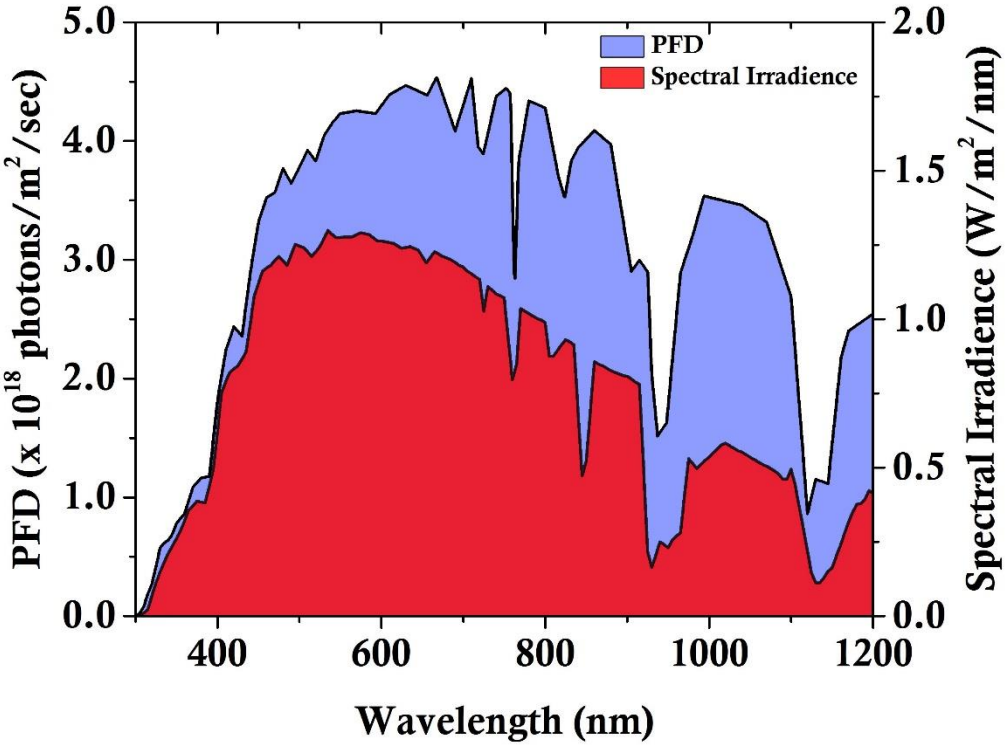

Figure 1.2 The PFD spectra and spectral irradiance of AM1.5 solar spectrum.

In order to find an upper theoretical efficiency limit, Shockley and Queisser [18] derived a thermodynamic limit for a p-n junction solar cell in the early 60s. This maximum efficiency limit is called Shockley – Queisser limit or SQ limit, achievable for any semiconducting materials i.e. 33.5 % for GaAs and 32 % for Si. Non-radiative recombination of photon generated charge carriers in Si is detrimental for cell efficiency. GaAs, however, is comparatively more efficient because of its direct band gap with predominant radiative recombination. The SQ limit shows a broad maxima with the semiconductor band gap and Si and GaAs lie within this maxima. It has always been a goal for experimental scientists to achieve the SQ efficiency limit of any semiconductor,

experimentally. However, unwanted photon loss in the cell limits the efficiency to reach its theoretical maximum.

1.2 FIRST – AND SECOND – GENERATION SOLAR CELLS

First-generation solar cells are the conventional or traditional solar cells that are wafer-based and made of crystalline-Si (c-Si) [7] such as polycrystalline Si (poly-Si) and monocrystalline Si (mono-Si). These cells are entirely based on the concept of the p-n junction and are the commercially predominant PV technology. Solar cells made of c-Si are around 160 – 240 μm thick. Second-generation solar cells are thin-film solar cells that are based on amorphous Si [7], CIGS [9], GaAs [8], etc. These solar cells are commercially significant in building integrated photovoltaics or in a small power system.

1.3 THIRD – GENERATION SOLAR CELLS

In third-generation solar cells, new methods are applied to increase the photon absorption density in the solar cell to overcome the SQ limit by introducing an intrinsic layer [19], quantum wells [11], [13], [20], waveguides [21], [22], antireflection coating (ARC) [23], [24], back mirror contacts [24], etc. to utilize most of the photons of the solar spectrum in the earth's atmosphere [25].

The intrinsic layer in a solar cell increases space charge region and low energy band gap quantum well/waveguide layers increase the absorption spectrum range in the cell, which means that more photon absorption and hence the efficiency increases. Though, this creates recombination sites at the interface.

With these methods, the efficiency enhancement is a trade-off between charge carrier escape and recombination loss. This decides the thickness of the intrinsic layer [19] and/or no. of the quantum well layers [26] in the cell. Furthermore, the photon loss happens not only inside the cell but also at the surface. The front surface of a solar cell causes high sunlight reflection due to an abrupt refractive index change at the air (surrounding medium)/cell interface. A high number of photons get lost at the interface and don't go through the absorption process. The ARC [23] is typically used to reduce this loss.

In this doctoral thesis, I present a theoretical framework on the light photon management in Si and GaAs solar cells with hybrid ARC using metal / dielectric nanoparticles (NPs) embedded in a traditional single-layer thin film ARC (also called $\lambda/4$ coating) [27]. I also optimize the performance of the hybrid ARC on a wide-angle of incidence (AOI), since commercially available solar cells are usually coated with an ARC, which is such that the reflectance is minimal for a wavelength near the maximum of the solar spectrum under normal incidence. But in reality, a fixed solar cell on a house roof receives the sunlight throughout the day at various angles of incidence.

2

THEORETICAL BACKGROUND OF LIGHT REFLECTION

2.1 INTRODUCTION

In this chapter, I set down a theoretical foundation for the thesis. I start with a general discussion of the light reflection and its impact on a solar cell panel. The reflection at a surface is an angle-dependent quantity, hence I also discuss here the AOI of the sunlight on a solar cell surface. The ARC concept is described to reduce the light reflection at the front surface of the cell. For wide-angle antireflection, I propose to introduce NPs in the ARC layer. Therefore, scattering of the light due to nanostructures and its application have also been explained. An extended effective medium theory has been applied to model the metal NPs' scattering in a surrounding medium as in Chapter 3. To provide the

theoretical background, I give a short introduction to the effective medium theory at the end of this chapter.

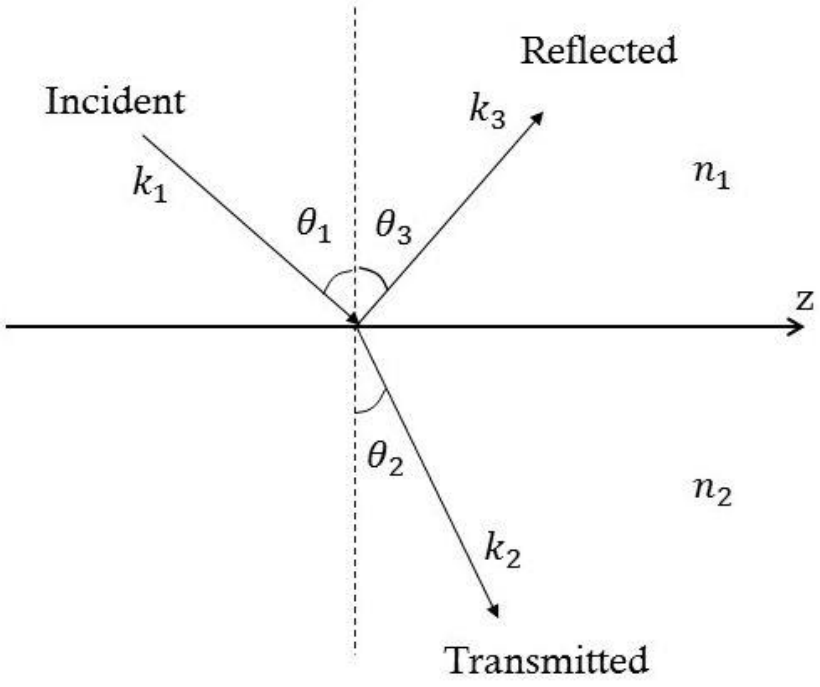

Figure 2.1 Reflection and transmission of an incident plane wave at an interface boundary.

2.2 REFLECTION AND TRANSMISSION

The reflection and transmission are a natural phenomenon which occurs at an interface where the refractive index (or the dielectric permittivity) changes [28]. High reflection is advantageous in some circumstances such as mirrors but not acceptable in solar cells [23].

A plane wave incident on the interface will split into two waves as a reflected wave propagating back into the first medium (n_1) and a transmitted wave proceeding into the second medium (n_2) as shown in Figure 2.1. k_1, k_2, and k_3 are the wave vectors corresponding to the incident, transmitted, and reflected waves with corresponding angles θ_1, θ_2, and θ_3 from the normal. n_1 and n_2 are the indices of refraction of incident and transmitted medium, respectively. For the conservation of energy, all three wave vectors must lie in a plane known as the plane of incidence (cf. Figure 2.1). And, the following relation must hold:

$$n_1 \sin(\theta_1) = n_2 \sin(\theta_2) = n_1 \sin(\theta_3) \tag{2.1}$$

Eq. (2.1) implies that the angle of reflection (θ_3) must be equal to the AOI (θ_1) and hence Snell's law,

$$n_1 \sin(\theta_1) = n_2 \sin(\theta_2) \tag{2.2}$$

An electromagnetic wave (the sunlight) consists of an electric field and a magnetic field. Based on the direction of the electric and magnetic field in the plane of incidence, the incident wave on the interface can be divided into two parts: TE Wave (s – polarized light) and TM Wave (p – polarized light).

2.2.1 Reflection and Transmission of TE Wave

When the incident wave has the electric field vector transverse to the plane of incidence, it is known as TE (transverse electric) Wave or s – polarized light.

From Fresnel equations, the reflection (r_s) and transmission (t_s) coefficients for TE Wave can be given as (cf. Figure 2.1)

$$r_s = \frac{n_1 \cos(\theta_1) - n_2 \cos(\theta_2)}{n_1 \cos(\theta_1) + n_2 \cos(\theta_2)} \tag{2.3}$$

$$t_s = \frac{2n_1 \cos(\theta_1)}{n_1 \cos(\theta_1) + n_2 \cos(\theta_2)} \tag{2.4}$$

2.2.2 Reflection and Transmission of TM Wave

When the incident wave has the magnetic field vector perpendicular to the plane of incidence, it is known as TM (transverse magnetic) Wave or p – polarized light. From Fresnel equations, the reflection (r_p) and transmission (t_p) coefficients for TM Wave can be given as (cf. Figure 2.1)

$$r_p = \frac{n_1 \cos(\theta_2) - n_2 \cos(\theta_1)}{n_1 \cos(\theta_2) + n_2 \cos(\theta_1)} \tag{2.5}$$

$$t_p = \frac{2n_1 \cos(\theta_1)}{n_1 \cos(\theta_2) + n_2 \cos(\theta_1)} \tag{2.6}$$

From eq. (2.3), (2.4), (2.5), and (2.6), it is clear that the reflection and transmission coefficient on a solar cell surface is highly dependent on the AOI of the sunlight. Therefore, I must introduce the AOI of the sunlight for a real-life scenario at a specified location in the earth's atmosphere.

2.3 ANGLE OF INCIDENCE OF THE SUNLIGHT

AOI of the sunlight on a solar cell surface, changes continuously from morning to evening in a full day, is the angle between the sun's ray and the normal on a solar cell surface which is given by [29]

$$\begin{aligned}\cos(\mathrm{AOI}) = {} & \sin(L) * \sin(\delta) * \cos(\beta) - \cos(L) * \sin(\delta) \\ & * \sin(\beta) * \cos(Z_s) + \cos(L) * \cos(\delta) * \cos(h) \\ & * \cos(\beta) + \sin(L) * \cos(\delta) * \cos(h) * \sin(\beta) \\ & * \cos(Z_s) + \cos(\delta) * \sin(h) * \sin(\beta) * \sin(Z_s)\end{aligned} \tag{2.7}$$

where L is local latitude: the angle between a line from the center of the earth to a point P on the earth surface and the equatorial plane, δ is solar declination, β is solar cell surface layer tilt angle from the horizontal, h is hour angle, and Z_s is surface azimuth angle (cf. Figure 2.2 & Figure 2.3, adapted from [29]).

2.3.1 Surface azimuth angle

The surface azimuth angle (Z_s) is the angle between the normal to the solar cell surface from due south for the Northern Hemisphere or due north for the Southern Hemisphere (cf. Figure 2.2). For a south-facing tilted solar cell surface in the Northern Hemisphere, $Z_s = 0°$. And, for a north-facing tilted solar cell surface in the Southern Hemisphere, $Z_s = 180°$.

2.3.2 Solar zenith angle

The solar zenith angle (ϕ) at a point P on the earth's surface is the angle between the sun's rays and the vertical OP (cf. Figure 2.3). For a horizontal plane, the zenith angle and AOI are the same.

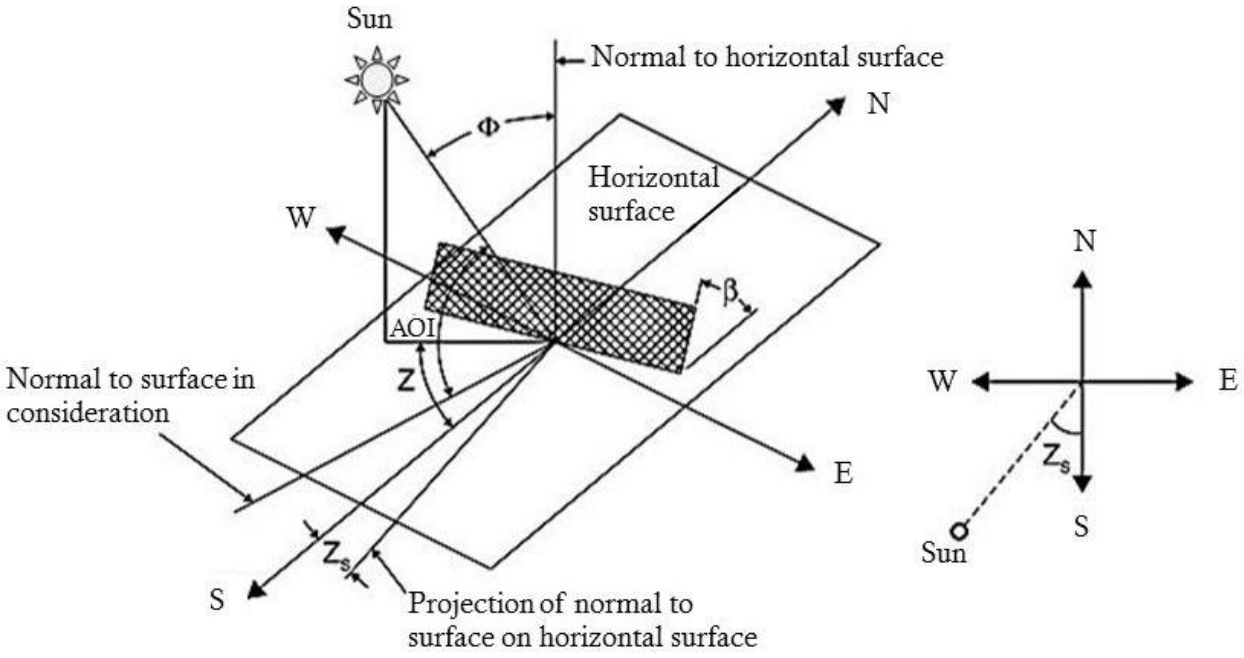

Figure 2.2 Illustration of solar angles at a plane (E: East, W: West, N: North, S: South).

2.3.3 Tilt angle and Hour angle

The tilt angle (β) is the angle between the horizontal surface and the solar cell surface (cf. Figure 2.2). The hour angle (h) of a point, P, on the earth's surface is the angle measured on the earth's equatorial plane between the projection of

OP and the projection of the sun and the earth center to center line (cf. Figure 2.3). The hour angle in degrees is

$$h = \pm 0.25 * (No.\ of\ minutes\ from\ local\ solar\ noon)$$

where the plus sign is for afternoon hours and the minus sign for the morning hours.

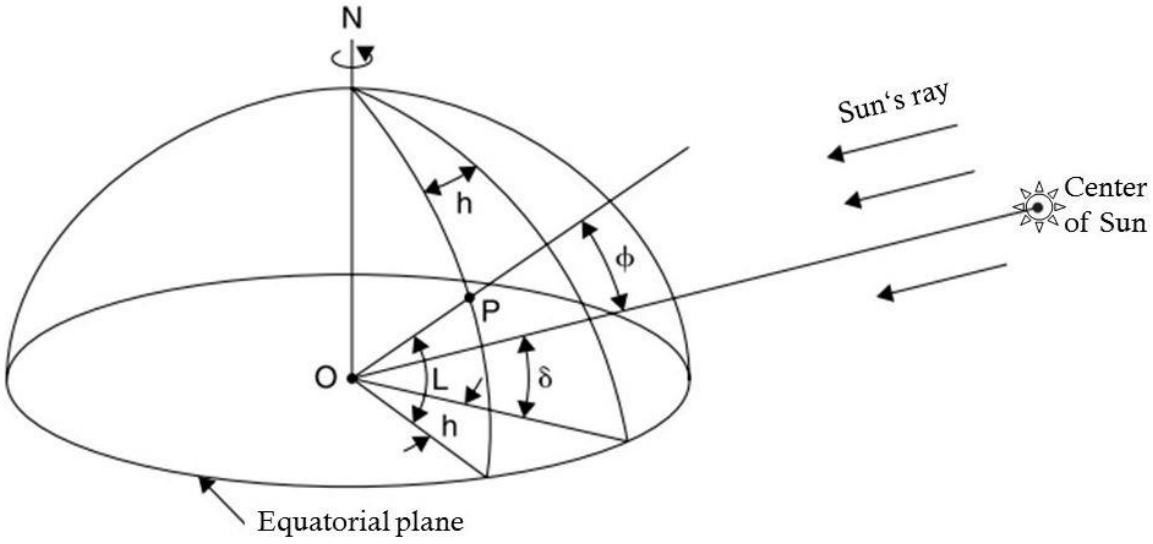

Figure 2.3 Latitude, solar angle, and declination.

2.3.4 Solar declination

Solar declination angle (δ) is the angle between the sun and earth center line and the projection of this line on the equatorial plane (cf. Figure 2.3). The solar declinations north of the equator are positive and south are negative, is given by

$$\delta = 23.45 * \sin\left[\frac{360}{365} * (284\ +\ N)\right] \qquad (2.8)$$

where N is no. of n^{th} day of the year.

Some data of declinations δ is given in Table 2.

Table 2 Day number in a year and corresponding solar declinations (δ).

Month	Day number	Average day of the month		
		Date	N	δ (°)
January	i	17	17	- 20.92
February	31 + i	16	47	-12.95
March	59 + i	16	75	-2.42
April	90 + i	15	105	9.41
May	120 + i	15	135	18.79
June	151 + i	11	162	23.09
July	181 + i	17	198	21.18
August	212 + i	16	228	13.45
September	243 + i	15	258	2.22
October	273 + i	15	288	-9.60
November	304 + i	14	318	-18.91
December	334 + i	10	344	-23.05

Lord Rayleigh [30] stated that the reflectivity of the outer surface of an object (i.e. Solar cell) could be reduced when the transition of refractive index between the object and surrounding medium is gradual. Later, H. Taylor discovered a decrease in reflection associated with a tarnish (coating) that develops on a glass surface [31]. F. Wright performed various chemical experiments to produce the "tarnish" and proposed an explanation of the effect that small pits on a glass surface results in a decrease of the refractivity at the surface by giving a gradual transition in the refractive index from glass to air instead of an abrupt change. This gradual transition leads to decrease in reflectivity and conceptualize the ARC development [31].

2.4 THIN – FILM ANTIREFLECTION COATING (ARC) IN SOLAR CELLS

Decades of optical and optoelectronic device development have led to the search for ways to maximize sunlight collection. The ARCs have played a major role in this regard in solar cell development. Various methods and strategies have been unfolded to minimize the front surface reflection such as Single – Layer ARC [23], [32], Double – Layer ARC [23], [33], Multilayer ARC [34], [35], Textured surface ARC [36]–[38], etc. Some of them are explained in the following sections.

2.4.1 Single – Layer ARC

Single – Layer ARCs are used in laser, photodiodes, etc. where the reflection needs to be minimum at a single wavelength or throughout a narrow band [23]. In solar cells, this is used to get minimum reflection at 550 nm wavelength at which spectral irradiance of the solar spectrum is maximum (cf. Figure 1.2). The reflection from any surface of a non-absorbing material with a surrounding environment can be calculated by Fresnel equations (cf. Section 3.2.2) [33].

The reflection from a single – layer ARC is a result of constructive and destructive interference of the reflected light wave ($w1$ & $w2$) from the first interface (1) and internal interface (2) (cf. Figure 2.4 (a)). Considering that the refractive index of the non-absorbing material is n_s at a desired wavelength (λ), the surrounding environment medium have the refractive index n_0, and the required refractive index of ARC is n_{ARC}, the optical path difference (OPD) between the reflected light $w1$ & $w2$ at normal incidence ($AOI = 0°$) is given by

$$OPD = 2 * n_{ARC} * d_{ARC} \tag{2.9}$$

where d_{ARC} is the thickness of ARC. The reflected light can be discussed in two different cases.

Case 1: When the reflected light $w1$ & $w2$ are in phase, it leads to the constructive interference at the interface 1. In this case, OPD is given by

$$OPD = m * \lambda \quad where\ m = 1,2,3 \ldots \tag{2.10}$$

Case 2: When the reflected light $w1$ & $w2$ are out of phase, it leads to the destructive interference at the interface 1. In this case, OPD is given by

$$OPD = \left(m + \frac{1}{2}\right) * \lambda \quad where\ m = 0,1,2,3 \ldots \tag{2.11}$$

The perfect single – layer ARC works under the destructive interference condition (Case 2).

Therefore, from eq. (2.9) and (2.11), the required thickness of ARC (d_{ARC}) can be given by

$$d_{ARC} = \frac{\lambda}{4 * n_{ARC}} \tag{2.12}$$

In the case of destructive interference, the reflectance $R1$ & $R2$ at interfaces 1 & 2 must be equal to perfectly cancel out each other (cf. Figure 2.4 (a)). Therefore, from Fresnel equations at normal incidence

$$\frac{n_{ARC} - n_0}{n_{ARC} + n_0} = \frac{n_s - n_{ARC}}{n_s + n_{ARC}} \tag{2.13}$$

$$\Rightarrow \quad n_{ARC} = \sqrt{n_s * n_0} \tag{2.14}$$

with $n_0 < n_{ARC} < n_s$. From eq. (2.4) and (2.6), one needs to deposit a 73 nm coating with an $n_{ARC} = 1.87$ (e.g., Si_3N_4 [40]) to get the minimum reflection at

550 nm for silicon (Si) or GaAs ($n_s = 3.5$). In the glass (BK7) industry, single layer MgF_2 is the most commonly used ARC [32].

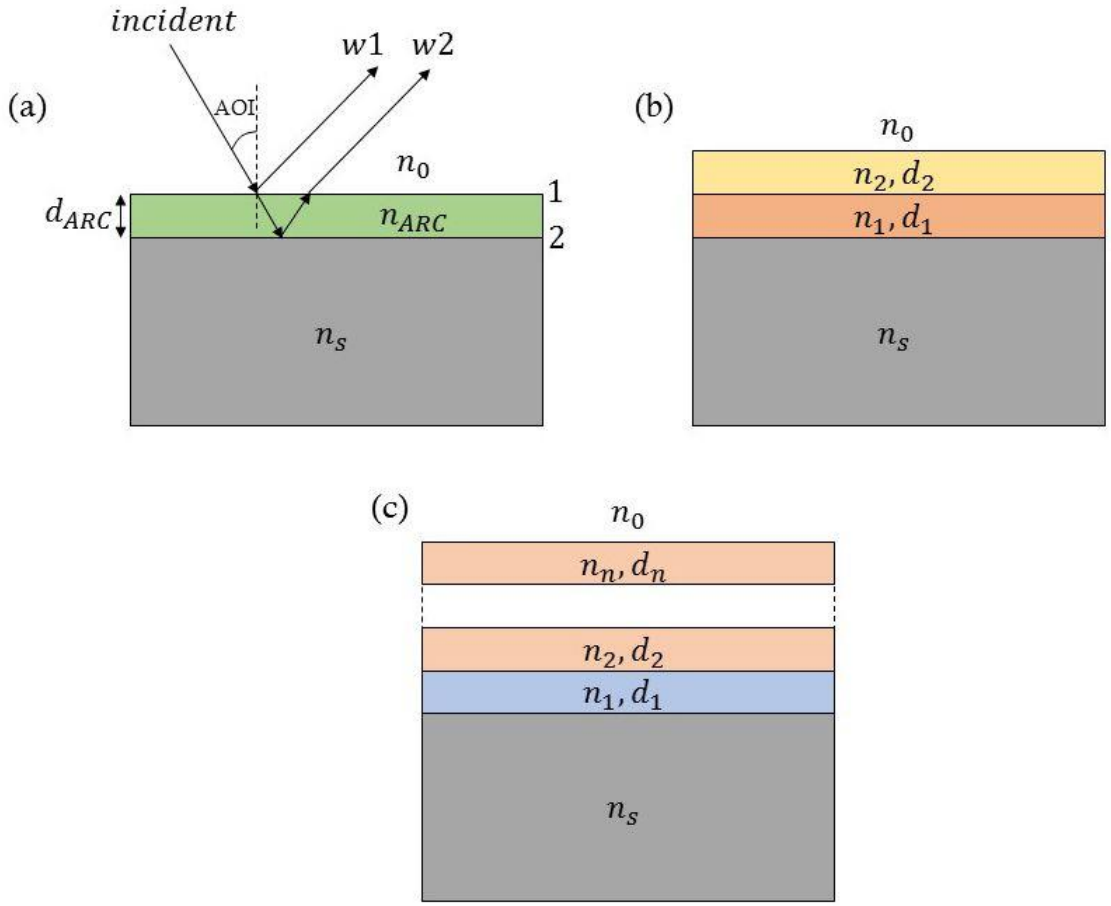

Figure 2.4 Schematic of various antireflection coating designs (a) Single-Layer ARC, (b) Double-Layer ARC, and (c) Multilayer ARC.

The major problem with single layer ARC is that they reduce the reflectivity for a single wavelength and AOI. The reflectivity increases for other AOIs because it causes constructive interference at the surface. Furthermore, there are limited

number of natural materials in the atmosphere with a low refractive index for transparent media. For example, for glass ($n = 1.5$), the refractive index of the single-layer ARC is equal to 1.22, from eq. 2.14. In nature, no other material is found with this refractive index and hence any material, with a refractive index close to this value, can be used which will certainly not minimize the reflection efficiently.

2.4.2 Double – Layer ARC

Further reduction in the reflection can be achieved by a double layer ARC, also called V-shaped ARC (named after its V-shaped spectra). These coatings are also famous in laser and solar cell applications when minimum reflection is required only at a specific band of wavelength [32]. For this, the thickness and refractive indices of layers must agree with the following equations to reduce the reflection down to zero:

$$n_1 * d_1 = n_2 * d_2 = \frac{\lambda}{4} \tag{2.15}$$

$$n_1 * n_2 = n_0 * n_s \tag{2.16}$$

where n_1, d_1, n_2, and d_2 are the thickness and refractive indices of two layers with $n_0 < n_1 < n_2 < n_s$ (cf. Figure 2.4 (b)).

In Si-solar cells, many combinations of thin-film layers have shown interesting low reflection results such as MgF_2 ($n = 1.38$) and CeO_2 ($n = 2.2$); MgF_2 ($n = 1.38$) and ZnS ($n = 2.3$) [23], [33], etc.

2.4.3 Multilayer ARC

Multilayer ARCs are used for broadband antireflection. These ARCs are a combination of several continuous dielectric thin film layers as shown in Figure 2.4 (c) [34], [35], [41]. The total reflectance from a multilayer ARC is generally modelled with Transfer Matrix Method (TMM) [28], [42], Finite Difference Time Domain method (FDTD) [35], etc. The TMM method is explained in detail in Section 3.2.2.

The TiO_2/SiO_2 multilayer is the most widely used combination for multilayer ARC which has shown promising antireflective properties for glass [43]–[45] and Si [46] in visible wavelengths.

From a fabrication point of view, thin-film ARCs can be made with various thin – film deposition techniques such as spin – coating [47], [48], dip – coating [49]–[52], chemical vapor deposition (CVD) [53], plasma – enhanced chemical vapor deposition (PECVD) [54]–[56], thermal evaporation [57], magnetron sputtering [58], etc.

In textured surface ARC, the surface has a pattern of structure (i.e. pyramids [38], moth's eye [59], etc.) with a cross-sectional dimension less than the light wavelength. These patterns perform a medium with spatially varying refractive index. If the cross-sectional dimension is equal to or larger than the

the incident light wavelength, it scatters the light with not much help in transmission.

2.5 LIGHT SCATTERING BY NANOSTRUCTURES

Light scattering by subwavelength nanostructures is one of the fundamental problems of electrodynamics. The physical understanding of this began with an electric dipole concept, introduced by Lord Rayleigh [60]. It starts with assuming that the electromagnetic field is constant in the region of interest as the size of the nanostructure is small comparing to the light wavelength. Then the homogeneous field of the incident light induces a polarization which in result scatters the light. The polarization is determined by the dielectric function of materials [61].

The linear optical phenomena of any media with known dielectric functions can in principle be modelled by solving Maxwell's equations [62]. However, the exact solution of light scattering by small particles was published by Clebsh [63] in 1863, a year before Maxwell's work about the electromagnetic theory of light. The breakthrough in understating light scattering by spherical nanostructures came from the work of Mie [64].

2.5.1 Mie Theory

The light scattering by spherical nanostructures such as spherical NPs has been theoretically formulated by G. Mie [64]. The solutions for the interaction of a plane electromagnetic wave by homogeneous NPs of an arbitrary index of refraction and any diameter embedded in a homogeneous dielectric medium, as shown in Figure 2.5, are famously known as Mie theory [64], [65], and

expressed as infinite series for total extinction (Q_{ext}), scattering (Q_{sca}) and backscattering (Q_b) efficiency of a homogeneous NP which are as follows

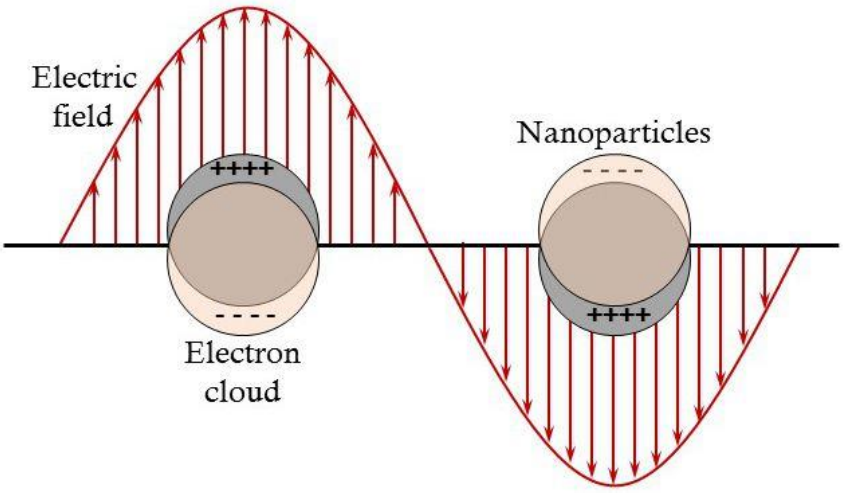

Figure 2.5 Schematic of the electromagnetic field interaction with spherical NPs.

$$Q_{ext} = \frac{2}{x^2} * \sum_{n=1}^{\infty} (2n+1) * Re[a_n + b_n] \tag{2.17}$$

$$Q_{sca} = \frac{2}{x^2} * \sum_{n=1}^{\infty} (2n+1) * [(a_n)^2 + (b_n)^2] \tag{2.18}$$

$$Q_b = \frac{1}{x^2} * \left| \sum_{n=1}^{\infty} (2n+1) * (-1)^n * (a_n + b_n) \right|^2 \tag{2.19}$$

where $a_n = \frac{m\psi_n(mx)\psi_n'(x) - \psi_n(x)\psi_n'(mx)}{m\psi_n(mx)\xi_n'(x) - \xi_n(x)\psi_n'(mx)}$,

$b_n = \frac{\psi_n(mx)\psi_n'(x) - m\psi_n(x)\psi_n'(mx)}{\psi_n(mx)\xi_n'(x) - m\xi_n(x)\psi_n'(mx)}$, and size parameter x is $2\pi n_h r/\lambda$. m is the ratio of the refractive index of NP (n_r) to that of the surrounding medium (n_h), r is the radius of the sphere, and λ is the wavelength of sunlight. ψ_n and ξ_n are Riccati-Bessel functions. a_n and b_n vanish as m approaches to unity; it means when the NP disappears, so does the scattered field.

Subwavelength nanostructures have shown promising advantages in solar cell applications such as localized surface plasmon resonance (LSPR) in metal NPs and strong suppression of the light reflection at resonance wavelength [66], [67]. The electromagnetic light in metal nanostructures excites the collective oscillation of free electrons. And, it's prominent near the plasmon resonance wavelength. This phenomenon is known as LSPR, and the field of study is known as Plasmonics [66].

Spherical metal NPs are used extensively in solar cells due to their high scattering property in a wide range of the solar spectrum [14], [68]–[73]. The solar cell structures have been demonstrated with improved performance due to NPs such that Au – NPs at the front side of Si solar cells [14] and Ag – NPs at the front side of GaAs solar cells [72] reduce the incident sunlight reflection and enhance the efficiency of the cell. Temple et al. investigated the optical property of metal NPs and found out that Ag – NPs scatter more than 97 % of the visible range of the AM1.5 solar spectrum [74]. Cole et al. used Mie theory simulations and determined that a 30 % of surface coverage of Ag – NPs of radius 105 nm can scatter 98.9 % of photons in the range 380 nm – 820 nm [75]. Despite the various studies on these metal NPs, practical applications have many other challenges such as large ohmic losses in metals which suppress

NPs' resonances [76], or parasitic surface oxidizing in the environment which changes the optical properties of NPs [77]. These NPs also face high absorption at the resonance wavelength. Alternatively, all-dielectric nanostructures have emerged recently as a promising candidate [32], [78], [79]. These nanostructures have a high refractive index with electric and magnetic Mie resonances and allow simultaneous control of electric and magnetic components of the light at the nanoscale [80]. These nanostructures also do not show absorbing behavior in a narrow band range [81]. This has been captured the attention of the scientific community and being investigated widely. Dielectric NPs in the solar cell applications have been demonstrated experimentally [82]–[87] and theoretically [88]–[92] with improved device performance. Wan et al.'s TiO_2 – NPs coated solar cell exhibited ca. 30 % enhancement in the photocurrent [85]. Whereas, Ha et al. demonstrated experimentally more than 30 % efficiency gain by using dielectric SiO_2 – NPs on a GaAs solar cell [86]. These NPs are closely packed and work as an ARC. The wide-angle improvement was also noticed for the entire visible spectrum. Huang et al. measured the normalized current density of with/without sub-micrometer silica (SiO_2) spheres coated amorphous Si solar cells and noticed the enhancement after 40° AOI [93]. These high refractive index dielectric NPs possess high directionality at a specific wavelength which results in strong forward and low backward scattering [94], [95]. This behavior of NPs with equal electric and magnetic dipole moments was predicted by Kerker and colleagues [96]. Such NPs are also called sometimes Huygens element [97], [98]. Huygens elements are proposed to be used in metasurfaces and future photonic devices for the efficient light control at the nanoscale level [99].

The scattering property of other regular structures i.e. ellipsoid and cylinders with arbitrary radius can also be modelled with the so-called corrected Mie

theory. The optical properties of spheroidal particles such as plasmonic NPs with elongated shapes have been studied in detail with modifications of Mie theory known as the Gans modifications [100]. Maxwell – Garnett (MG) effective medium theory [101] providing an effective medium approach is also one of its kind which is explained in the next section.

2.6 MAXWELL – GARNET (MG) EFFECTIVE MEDIUM THEORY

The MG effective medium theory, developed by Maxwell Garnet [101], approximates the dielectric permittivity of an effective medium in terms of the dielectric permittivities of individual constituents of the complex medium. The theory is summarized in brief here[102]. If small spherical NPs of radius r and dielectric permittivity ε_r suspended in a host medium of permittivity ε_h (cf. Figure 2.6), with the effective dielectric permittivity of the system ε_{eff}, then from the Clausius-Mosotti equation,

$$\frac{\varepsilon_{eff} - \varepsilon_h}{\varepsilon_{eff} + 2\varepsilon_h} = \frac{f}{r^3} * \alpha \tag{2.20}$$

where α is the NP dipole polarizability and f is the volume fraction of embedded NPs (cf. Section 3.2). The NP dipole polarizability is given by

$$\alpha = \frac{\varepsilon_r - \varepsilon_h}{\varepsilon_r + 2\varepsilon_h} * r^3 \tag{2.21}$$

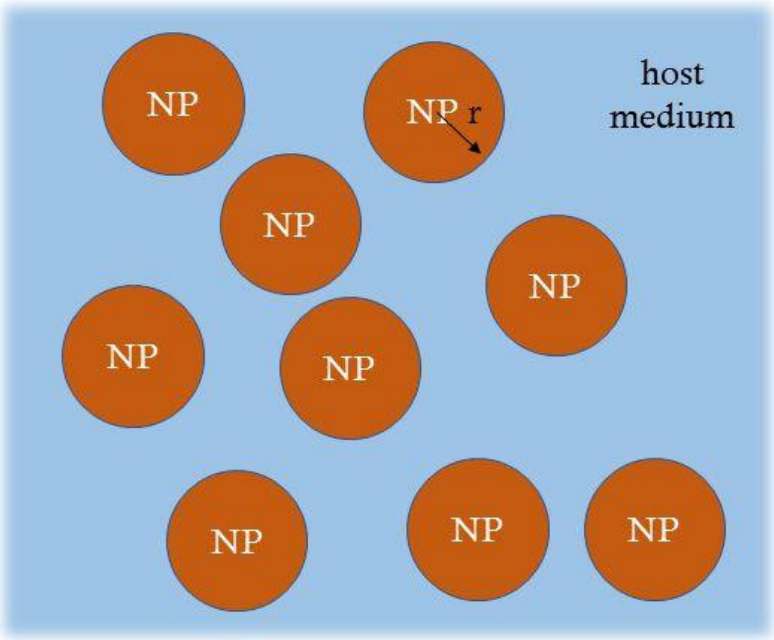

Figure 2.6 Spherical NPs in a host medium.

Substituting this in Eq. (2.20), it yields the effective dielectric permittivity as

$$\varepsilon_{eff} = \varepsilon_h * \frac{\varepsilon_r * (1 + 2f) + 2\varepsilon_h * (1 - f)}{\varepsilon_r * (1 - f) + \varepsilon_h * (2 + f)} \tag{2.22}$$

This equation is valid for $r \ll \lambda$, where λ is the incident sunlight wavelength.

In the present thesis, the optical properties of nanocomposite layer (spherical NPs' in a host medium) have been studied using the extended effective medium theory which is a modified version of the MG effective medium theory [103] (cf. Section 3.2). Moreover, this theory only considers the specular

behavior of the sunlight as specular reflection and specular transmission in a thin film (the nanocomposite layer in my case) and suppresses the radiation property of NPs. Therefore, the Dipole model [104] combined with Mie scattering has been adapted to describe the radiation profile of NPs, which is explained in Section 4.2.

3

EFFECTIVE MEDIA

3.1 INTRODUCTION

In this chapter, I present a study on the optical properties of metal NPs (Ag, Au, Al, and Cu) and a simulation study of metal NPs on n-GaAs absorber layer with different AOI of the sunlight. Some of the results have been published in Ref. [1]. Mie theory has been used to model the optical properties of NPs. These are given in terms of NPs' efficiencies such as scattering efficiency (Q_{sca}) and absorption efficiency (Q_{abs}) (cf. Section 2.5). The sum of both efficiencies is called extinction efficiency (Q_{ext}) of NPs. I have also calculated a dimensionless quantity, Q_{sca}/Q_{ext}, called radiative efficiency (Q_{rad}) of NPs. With the help of extended MG effective medium theory [103], I calculated an effective permittivity of the nanocomposite layer (NPs and host medium). The TMM

method has been implemented to calculate the optical properties of multilayer thin film [28]. When the light incident on an NP, it causes a radiation pattern with different wave vectors spreading over wide angles in the absorber layer [105]. Whereas, the effective medium theory leads to a specular transmission of the incident light in the absorber layer. This simplified analytical model does not consider the complete radiation profile of NPs and is sufficient to get a quick overview on the usage of different metal NPs and their sizes in the nanocomposite layer for high power transfer for which the complete picture of scattering profile is unnecessary. The model is purely based on Mie theory, thereby ignoring any quantum effects such as the coupling effects on the dielectric function of NP and the substrate due to the high-efficiency energy transfer channel between the plasmons in NPs and the band electrons of the substrate [106].

3.2 METHODS

3.2.1 Extended MG Effective Medium Theory

Doyle [103] suggested an approach that allows effective electric dipole polarizability obtained from Mie theory and to be used in the MG effective medium theory. In this approximation, the effective electric dipole polarizability (α_1) of an isolated sphere in a host medium is given as

$$\alpha_1 = i * \frac{3r^3}{2x^3} * a_1 \tag{3.1}$$

where the size parameter x is $2\pi n_h r/\lambda$, n_h is a ratio of the refractive index of NP to that of surrounding medium (the host medium), r is the radius of the sphere, a_1 is the scattering coefficient (cf. Section 2.5) and λ is the wavelength of sunlight.

Putting this value in the MG effective medium theory expression yields an extended MG effective medium theory for spheres of nonzero size as

$$\frac{\varepsilon_{eff} - \varepsilon_h}{\varepsilon_{eff} + 2\varepsilon_h} = \frac{2\pi i N_0 r^3 \alpha_1}{x^3} \tag{3.2}$$

where $i^2 = -1$; ε_{eff} and ε_h are the effective permittivity of the nanocomposite (NPs and the host medium) layer and the host medium, respectively. The NPs' density N_0 is related with volume-filling factor $f = 4\pi N_0 r^3/3$. The expression of f is obtained as follows:

The volume of the nanocomposite layer is $V_{NC} = l * b * d$, where d is the thickness, l is the length, and b is the breadth of the layer. The volume of a spherical NP is $V_{NP} = (4/3)\,\pi r^3$. So, the number of NPs in the layer can be given as $N_{NPs} = (l/p) * (b/p)$, where p is the period of NPs array distributed in two-dimensional (2D) in the layer. Thus, the volume fraction (f) of NPs in the layer is given by, $f = (N_{NPs} * V_{NP})/V_{NC}$ [42]. The dipole approximation is valid for small volume fractions ($f < 0.5$) [107].

3.2.2 Transfer Matrix Method (TMM)

In order to calculate transmission from the nanocomposite layer, the TMM method, also called 2x2 matrix method, has been applied which allows to determine reflection, transmission, and absorption in a multilayer thin film [28]. The method is summarized as follows. I assume that a plane wave incidents on a multilayer thin-film structure which is having l layers between air and a semi – infinite substrate $(0, s)$ (cf. Figure 3.1). Each layer ($j = 1,2,3 \ldots m$) has a thickness of d_j with complex refractive index n_j. When, the plane wave incident at the interfaces of the multilayer thin film, it follows Snell's law (Section 2.2). If the electric field in j^{th} layer propagating in positive x-direction is E_j^+ and in negative x-direction is E_j^-, a transmission matrix for the j^{th} layer can be written as

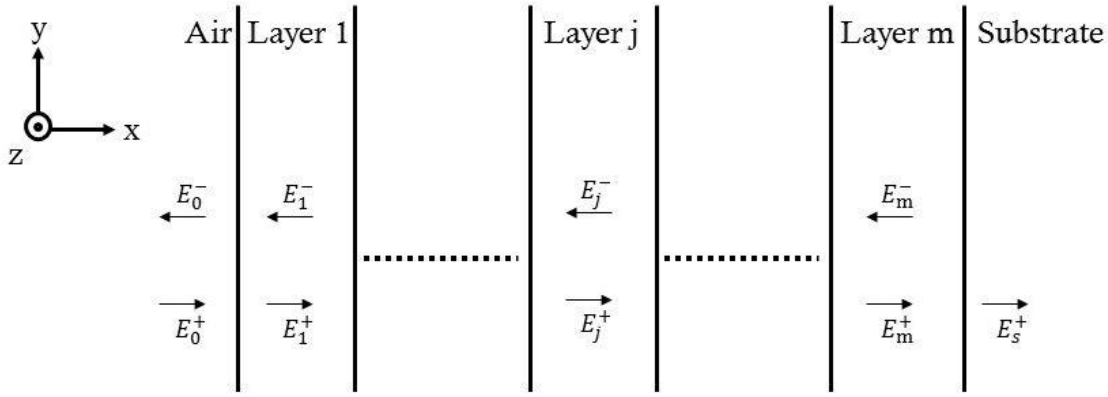

Figure 3.1 Schematic diagram of a multilayer thin-film structure with m layers between air and semi-infinite substrate.

$$M_{jk} = \frac{1}{t_{jk}} * \begin{bmatrix} 1 & r_{jk} \\ r_{jk} & 1 \end{bmatrix} \tag{3.3}$$

where t_{jk} and r_{jk} are Fresnel transmission and reflection coefficients at an interface jk, which are defined as (cf. Section 2.2)

$$\left.\begin{aligned} r_{jk} &= \frac{n_j \cos(\theta_j) - n_k \cos(\theta_k)}{n_j \cos(\theta_j) + n_k \cos(\theta_k)}, \\ t_{jk} &= \frac{2.n_j \cos(\theta_j)}{n_j \cos(\theta_j) + n_k \cos(\theta_k)} \end{aligned}\right\} for\ s-polarized\ light\ (TE) \tag{3.4}$$

and

$$\left.\begin{aligned} r_{jk} &= \frac{n_j \cos(\theta_k) - n_k \cos(\theta_j)}{n_j \cos(\theta_k) + n_k \cos(\theta_j)}, \\ t_{jk} &= \frac{2.n_j \cos(\theta_j)}{n_j \cos(\theta_k) + n_k \cos(\theta_j)} \end{aligned}\right\} for\ p-polarized\ light\ (TM) \tag{3.5}$$

A propagation matrix for the plane wave propagating through the j^{th} layer is given by

$$P_j = \begin{bmatrix} e^{-i.(2\pi/\lambda).d_j.n_j.\cos(\theta_j)} & 0 \\ 0 & e^{i.(2\pi/\lambda).d_j.n_j.\cos(\theta_j)} \end{bmatrix} \tag{3.6}$$

where λ is the wavelength of the incident wave and θ_j is the angle of refraction.

By using the transmission and propagation matrices, a total transfer matrix $\boldsymbol{M}$, for the whole stacks of layers which relates the incident electric field at the first interface (air/layer-1) with the transmitted electric field through the last interface (layer- l/substrate), is given by

$$\begin{bmatrix} E_0^+ \\ E_0^- \end{bmatrix} = \boldsymbol{M} \begin{bmatrix} E_s^+ \\ 0 \end{bmatrix} = M_{01} * P_1 * M_{12} * P_2 \dots\dots P_l * M_{ls} \begin{bmatrix} E_s^+ \\ 0 \end{bmatrix} = \begin{bmatrix} \boldsymbol{M_{11}} & \boldsymbol{M_{12}} \\ \boldsymbol{M_{21}} & \boldsymbol{M_{22}} \end{bmatrix} \tag{3.7}$$

The transmission and reflection coefficients can be expressed from eq. (3.7) as $t = \frac{1}{\boldsymbol{M_{11}}}$; $r = \frac{\boldsymbol{M_{21}}}{\boldsymbol{M_{11}}}$.

Taking into account the above results, the reflectance is given as $R = |r|^2$ and the transmittance is given as $T = \frac{n_s \cos(\theta_s)}{n_0 \cos(\theta_0)} . |t|^2$, where s and 0 are corresponding to the substrate and the incident medium (air).

Since the transmittance needs to be maximized where the solar spectrum has a maximum intensity, I have calculated weighted solar power transfer (P_w):

$$P_w = \frac{\int_{\lambda_{min}}^{\lambda_{max}} T(\lambda) * S(\lambda)\, d\lambda}{\int_{\lambda_{min}}^{\lambda_{max}} S(\lambda)\, d\lambda} \tag{3.8}$$

where $T(\lambda)$ and $S(\lambda)$ are the transmittances and the intensity of the AM1.5 solar spectrum at wavelength λ. λ_{min} and λ_{max} are the minimum and maximum allowed wavelengths.

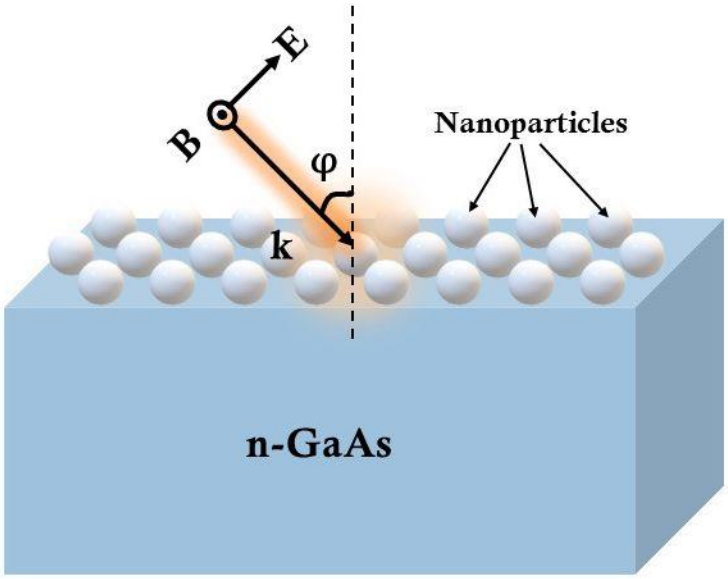

Figure 3.2 Schematic of the simulated device structure. E, B, and k are electric field, magnetic field, and wave vector of the incident electromagnetic wave, respectively. φ is the AOI.

The nanocomposite layer made of a 2D array of metal NPs (Ag, Au, Al, and Cu) of an equal period in a dielectric matrix (air in my case) bounded with air and n – GaAs absorber layer has been investigated. There are three layers (air, the nanocomposite layer, and n – GaAs layer) in the simulated device structure, each has a wavelength-dependent index of refraction. A schematic of the simulated device structure is shown in Figure 3.2. Data of the index of

refraction for n – GaAs absorber layer is taken from Ref. [108] and shown in Figure 3.4. Optical constants of metals are taken from Ref. [109] and shown in Figure 3.5. Linear interpolation is applied to fit the optical constants for the desired step size. The AM1.5 solar spectrum, used in the calculation, is shown in Figure 3.3 [25]. The angular dependent solar spectrum is ignored as it has no effect on the transmittance calculation. The n-GaAs layer is assumed to be non-absorbing.

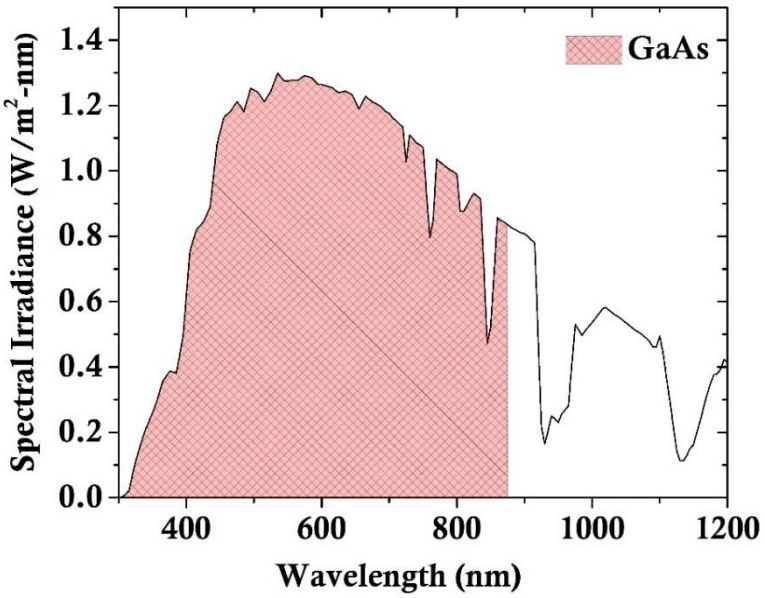

Figure 3.3 AM1.5 solar spectrum. Only red shaded are is available for n-GaAs absorber layer.

The dielectric permittivity of metal NPs (ε_r) of radius r is calculated by Drude model which is described as follows [110]

$$\varepsilon_r = \varepsilon_b + \Delta\varepsilon \tag{3.11}$$

$$\Delta\varepsilon = 1 + \frac{\omega_p^2}{\omega^2 + i\gamma\omega} - \frac{\omega_p^2}{\omega^2 + i\gamma(r)\omega} \tag{3.12}$$

$$\gamma(r) = \gamma + A * \frac{\nu_F}{r} \tag{3.13}$$

where ε_b is the bulk metal-dielectric permittivity, ω_p is the plasma frequency (= 5.8 x 10^{15} s^{-1}), γ is the electron scattering rate (= $0.01\omega_p$), and ν_F is the Fermi velocity (= 1.39 x 10^6 m/s). A is a dimensionless constant of order 1.

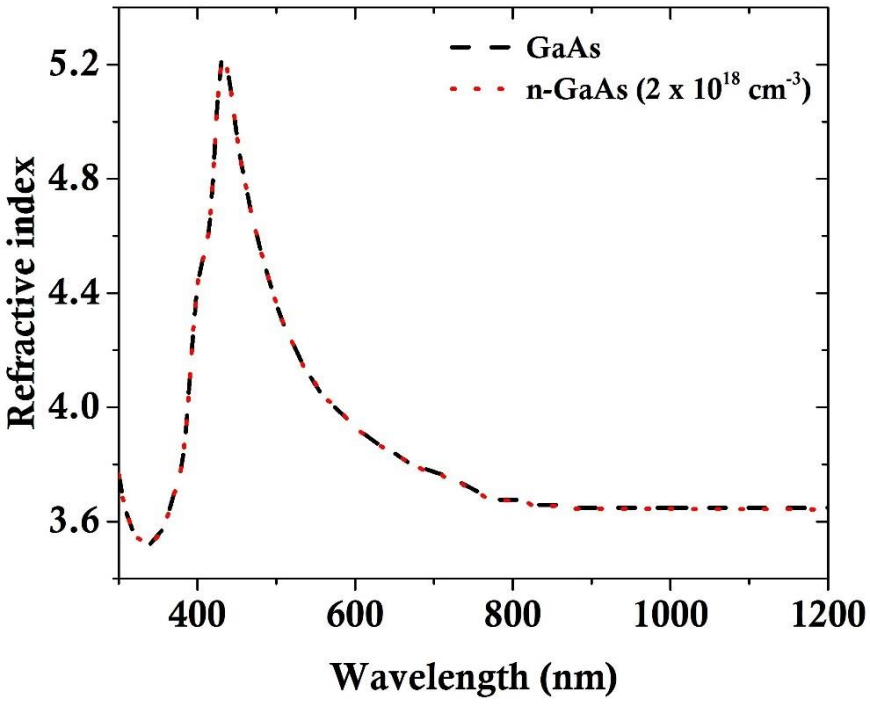

Figure 3.4 Real part (n) of the complex refractive index of GaAs and n – doped GaAs.

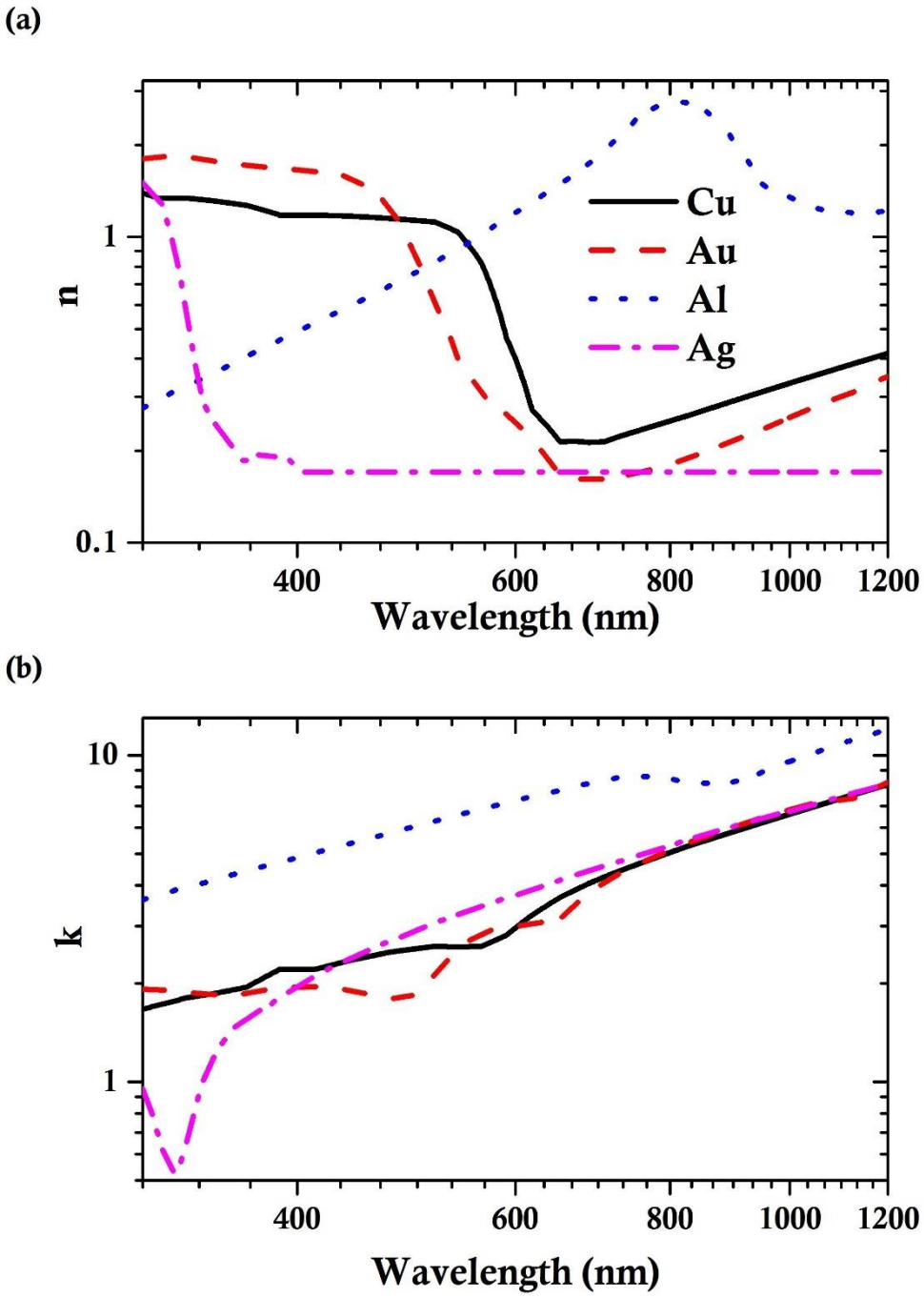

Figure 3.5 Complex refractive index of bulk metals (log scale) (a) real part (n), and (b) imaginary part (k).

3.3 RESULTS AND DISCUSSION

3.3.1 Radiative and Backscattering Efficiency

The efficiency curves (Q_{rad} and Q_b) have been illustrated for metal NPs of various sizes with the light operating wavelength 300 nm – 1200 nm. Q_{rad} and Q_b of Silver NPs (Ag – NPs), Gold NPs (Au – NPs), Copper NPs (Cu – NPs), and Aluminum NPs (Al – NPs) are shown in Figure 3.6, Figure 3.7, Figure 3.8, and Figure 3.9, respectively. Ag –, Au– and Cu – NPs show strong localized surface plasmon resonance in the visible region [74]. Metal NPs not only scatter the sunlight efficiently at resonance wavelength but also absorb. Dips in Q_{rad} spectra show the absorbance in metal NPs. Q_{rad} of Ag – NPs of diameters ≥ 100 nm have been observed more than 80 % in the visible range which is desirable for high power transfer (cf. Figure 3.6 (a)). Whereas Au – NPs of diameters ≥ 120 nm have Q_{rad} higher than 70 %, only for higher wavelength (550 nm – 900 nm). For wavelength range 350 nm – 500 nm, Q_{rad} of Au – NPs is below 60 % which is detrimental for high power transfer (cf. Figure 3.7 (a)) because the solar spectrum has a high no. of photons near 500 nm (cf. Figure 1.2). Similarly, Q_{rad} of Cu – NPs of diameter ≥ 120 nm is higher than 70 % in 650 nm – 800 nm spectrum range (cf. Figure 3.8 (a)) and below 60 % in 300 nm – 500 nm spectrum range. Al – NPs show weakly localized surface plasmon resonance compared to other metal NPs (Ag, Au, and Cu) [74]. However, Q_{rad} of Al – NPs is more than 80 % in the visible range for larger NPs (160 nm – 200 nm). For 40 nm diameter, it goes minimum such that 80 – 90 % of the incident sunlight got absorbed over all the wavelength (cf. Figure 3.9 (a)).

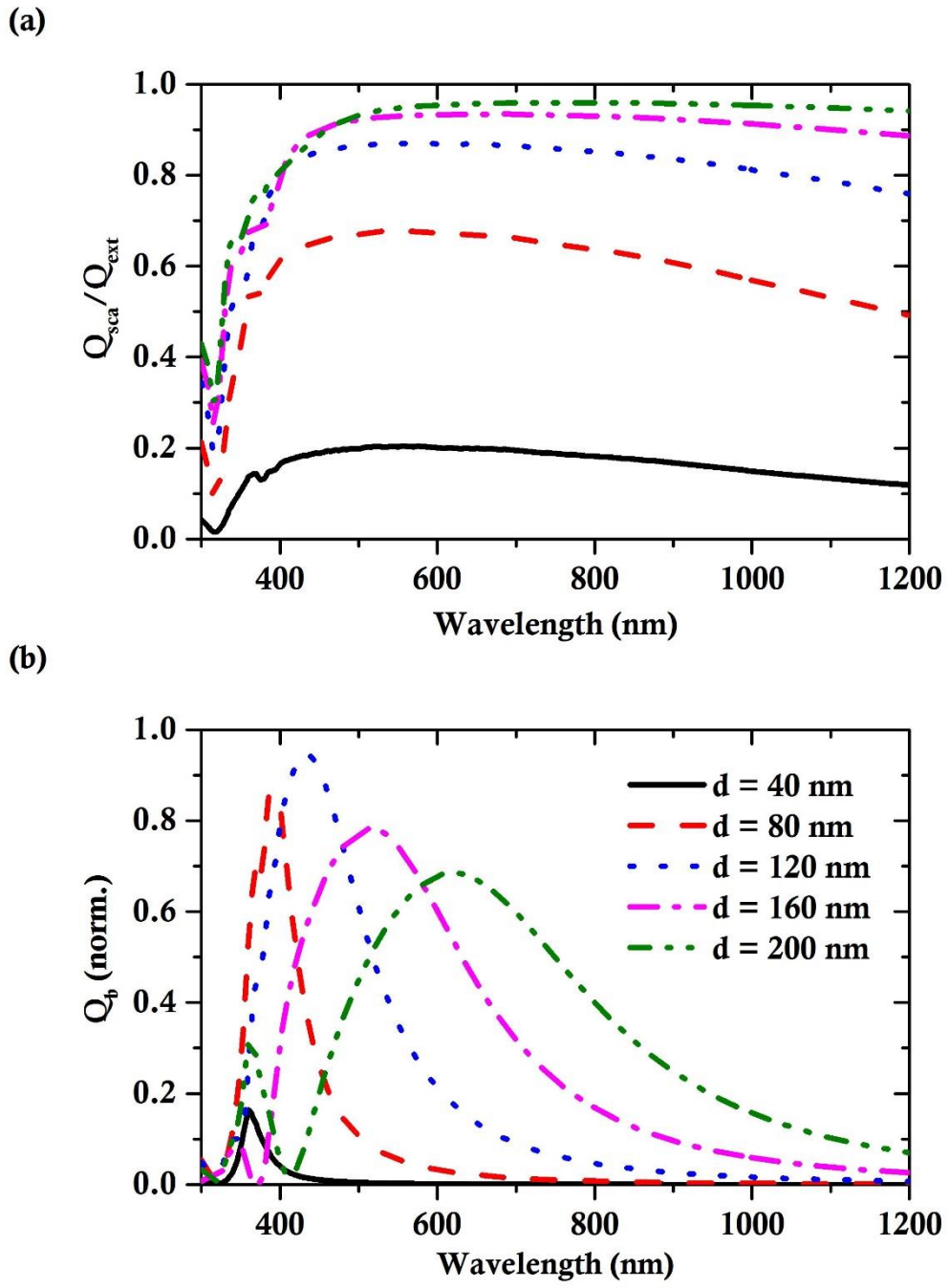

Figure 3.6 (a) Radiative efficiency ($Q_{rad} = Q_{sca}/Q_{ext}$), and (b) normalized backscattering efficiency (Q_b) of Ag-NPs of sizes 40 nm – 200 nm.

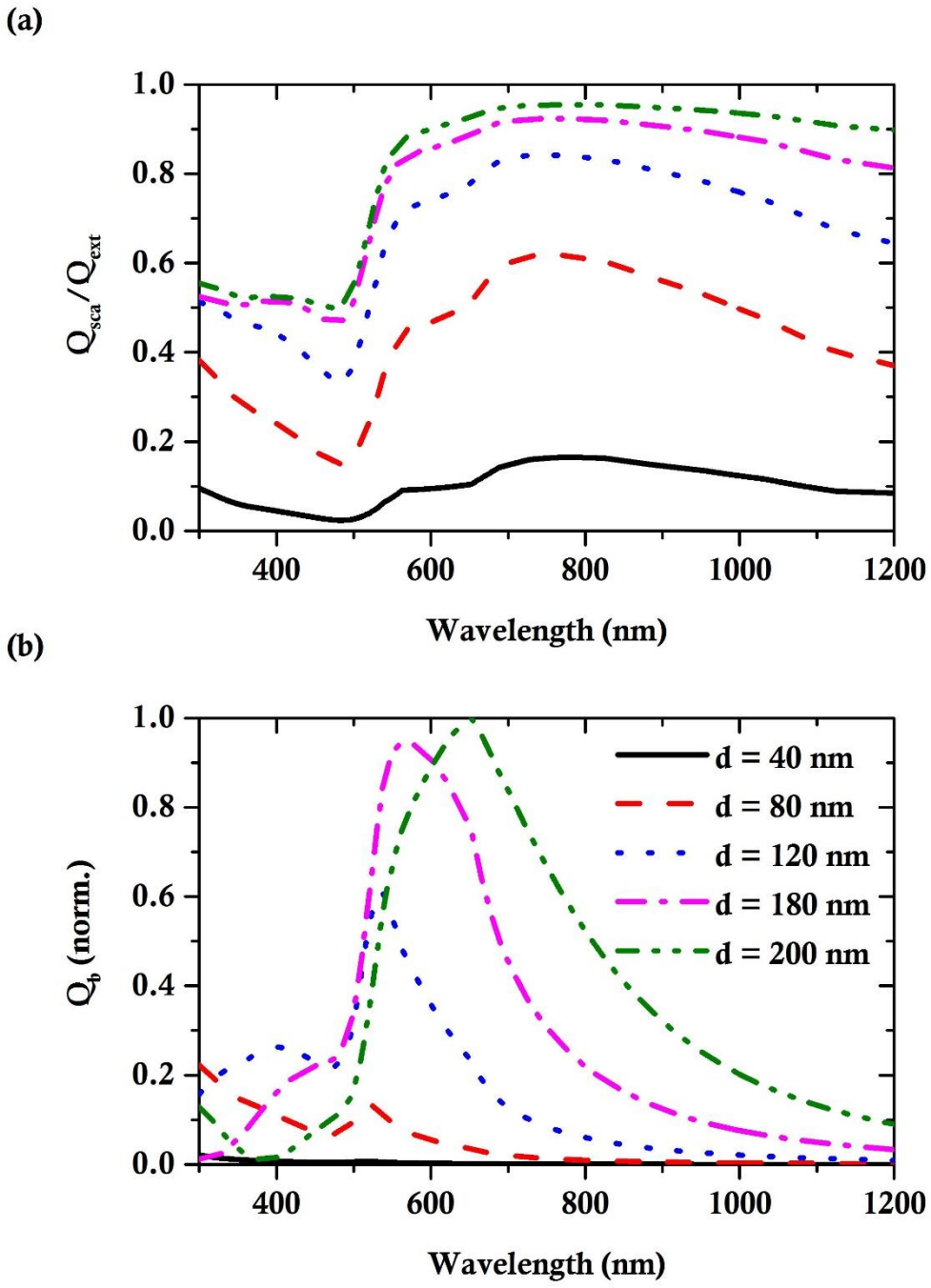

Figure 3.7 (a) Radiative efficiency ($Q_{rad} = Q_{sca}/Q_{ext}$), and (b) normalized backscattering efficiency (Q_b) of Au-NPs of sizes 40 nm – 200 nm.

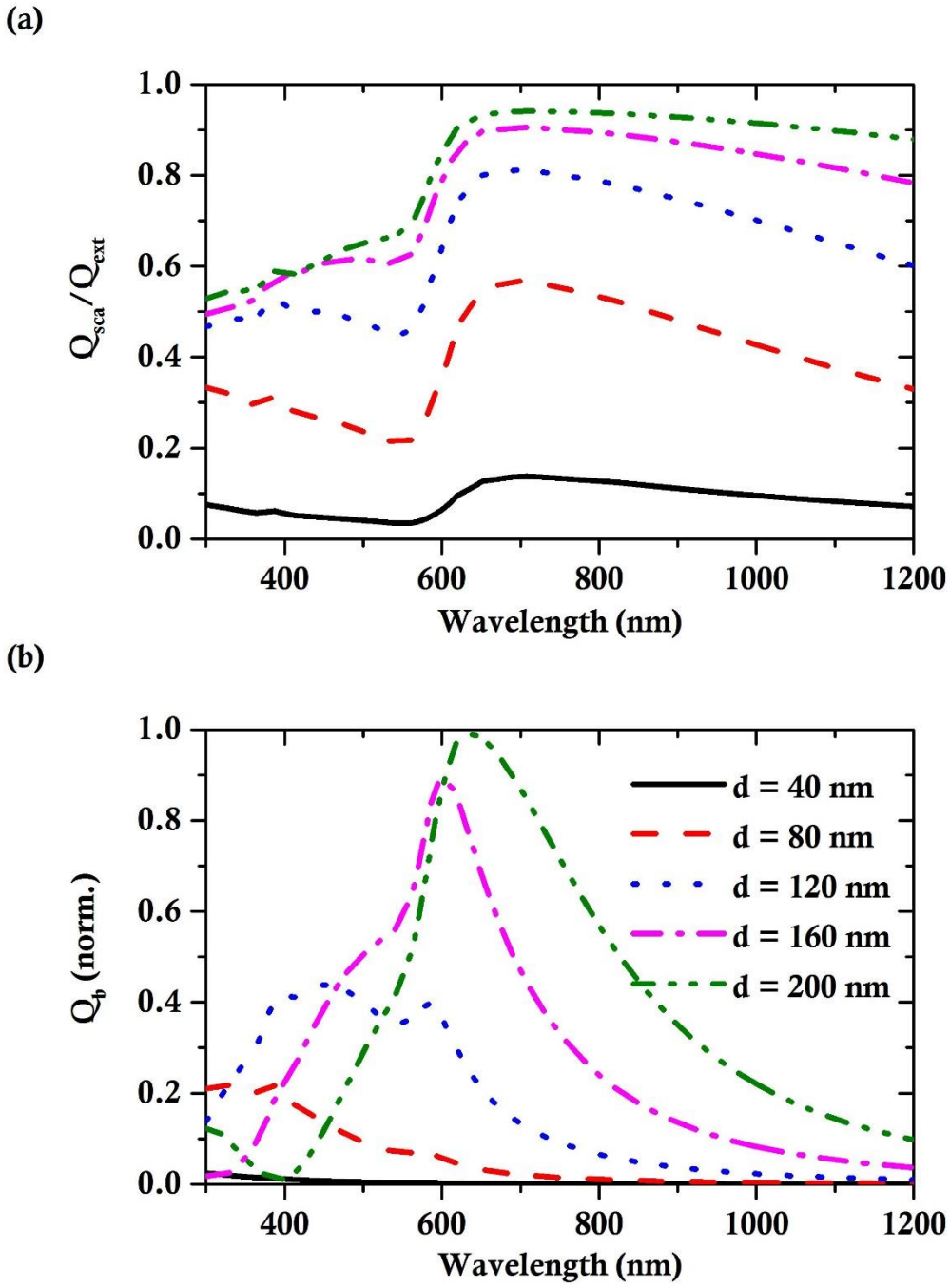

Figure 3.8 (a) Radiative efficiency ($Q_{rad} = Q_{sca}/Q_{ext}$), and (b) normalized backscattering efficiency (Q_b) of Cu-NPs of sizes 40 nm – 200 nm.

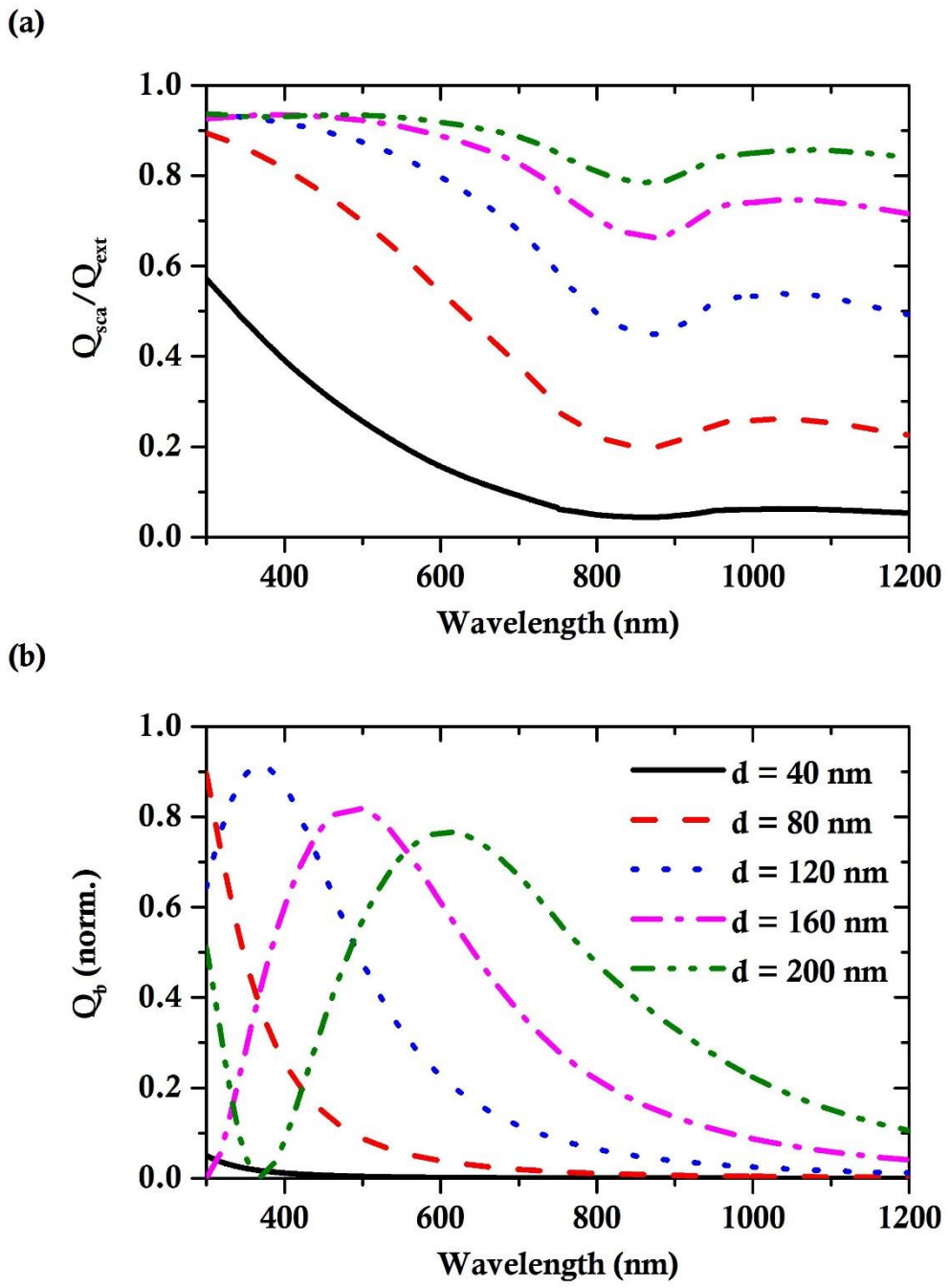

Figure 3.9 (a) Radiative efficiency ($Q_{rad} = Q_{sca}/Q_{ext}$), and (b) normalized backscattering efficiency (Q_b) of Al-NPs of sizes 40 nm – 200 nm.

Q_b of Ag – NPs increases and then decreases with the NPs' size and also, the curves become wider with the NPs' size (cf. Figure 3.6 (b)). Additionally, the resonance peak shifts towards high wavelength with the NPs' size. The highest Q_b peak is noticed at 408 nm for 120 nm NPs' size. Q_b of Au – NPs and Cu – NPs increases with the NPs' size and the highest is between 550 nm – 800 nm wavelength range (cf. Figure 3.7 (b) & Figure 3.8 (b)). Q_b of Al – NPs of smaller sizes are negligible in the visible range, but for the large NPs' size, it increases dramatically (cf. Figure 3.9 (b)). Same as Ag – NPs, Q_b of Au – NPs, Cu – NPs and Al – NPs become wider with wavelength and shifts to higher wavelengths with the NPs' size.

The optical properties of metals can be divided into free-electron and interband regions. The localized surface plasmon resonance in metals is predominantly due to the behavior of free electrons in the conduction band. Whereas interband transitions either damp or prohibit this transition. Noble metals such as Ag, Au, and Cu are distinguished by a threshold wavelength below which the optical properties of metals are dominant by the interband transition. This transition occurs at wavelengths 327 nm, 517 nm, and 590 nm approximately for Ag –, Au – and Cu – NPs, respectively. Al – NPs have a weak interband region near 827 nm [74]. Our calculations have shown the same behavior for these NPs. Ag –, Au – and Cu – NPs absorb the sunlight maximum at these wavelengths (cf. Figure 3.6 (a), Figure 3.7 (a), & Figure 3.8 (a)). Al – NPs show high absorption in the 800 nm – 900 nm wavelength range (cf. Figure 3.9 (a)).

In Figure 3.6 (a), Ag – NPs of diameters 160 nm – 200 nm show more than 90 % scattering of the sunlight over the spectral range 500 nm – 1200 nm. This

result coincides with the previously reported outcome such as optimal photon scattering could be achieved from large Ag – NPs [75]. Q_{rad} of Ag – NPs is high for larger NPs, which is a consequence of the localized surface plasmon resonance. The optical cross section is also high in this case which means that there is less parasitic absorption and more scattering. On the other hand, when the scattering is high so as the backscattering such that Q_b curves of Ag – NPs of smaller diameters are narrower compared to the larger ones (cf. Figure 3.6 (b)). Single-mode of dipole scattering in Ag – NPs is also noticed as the dominant one. Whereas the higher-order mode is only visible in larger particles, but the resonance peak of this mode is weaker which can be seen at wavelength 350 nm for NPs of size 200 nm as shown in Figure 3.6 (b). The higher-order mode is not visible in other metal NPs.

3.3.2 Power Transfer from the Nanocomposite Layer

P_w of metal NPs are illustrated in a contour plot using a matrix of NPs' diameter and AOI (cf. Figure 3.10, Figure 3.11, Figure 3.12, and Figure 3.13). There are four contour plots for each metal NPs with different volume fraction of NPs in the nanocomposite layer such as f = 0.10, f = 0.20, f = 0.30 and f = 0.40. For reference, I calculated P_w of an air / n-GaAs interface at 0°- 80° AOI. At 0° AOI, the reference P_w is obtained as 63.93 %. In contour plots, NPs of 0 nm diameter (on Y – axis) is corresponding to the reference (transmission from air / n-GaAs interface). 0° AOI is corresponding to the normal incidence.

P_w from the nanocomposite layer (Ag – NPs in the air medium) into n-GaAs layer are shown in Figure 3.10. It is noticed that P_w is high for NPs of diameters

20 nm – 200 nm range at f = 0.10 (cf. Figure 3.10 (a)). At the volume fraction f = 0.20, the maximum P_w = 77 % is achieved for NPs of diameters 60 nm – 120 nm (cf. Figure 3.10 (b)). As the volume fraction of NPs increases, the size of NPs for maximum P_w decreases. At f = 0.30, the NPs' diameters for maximum P_w restricts to 60 nm – 100 nm range (cf. Figure 3.10 (c)). In this case, the maximum P_w at 0° AOI is 79 %, which is 23 % increase in P_w comparing to the reference. The increase in P_w has also been noticed for wide angles from 0° to 70° AOI. For f = 0.40, the maximum P_w reduced to 76 % and restricts to 50 nm – 90 nm diameter range (cf. Figure 3.10 (d)).

For Au – and Cu – NPs, I obtained maximum P_w as 71 % at f = 0.20 which is 10.75 % increase in the reference P_w (cf. Figure 3.11 & Figure 3.12). Both contour plots look the same because their efficiencies' profiles are almost the same (cf. Figure 3.7 & Figure 3.8).

P_w contour plots of Al – NPs are shown in Figure 3.13. For Al – NPs, it is noticed that P_w is high for diameters of 40 nm – 200 nm range at f = 0.10 (cf. Figure 3.13 (a)). At the volume fraction f = 0.20, the maximum P_w = 81 % is achieved for Al – NPs of diameters 60 nm – 140 nm (cf. Figure 3.13 (b)). Also, in Al – NPs, as the volume fraction of Al – NPs increases, the size of NPs for maximum P_w decreases. At f = 0.30, the maximum P_w at 0° AOI is 86 % and the Al – NPs' diameters for the maximum P_w restricts to 60 nm – 120 nm range (cf. Figure 3.13 (c)). At f = 0.40, P_w is obtained maximum as 88 % for Al – NPs of diameters 60 nm – 100 nm range which is 38.28 % increase in the reference P_w. Wide – angle enhancement in P_w has been also noticed in the contour plot (cf. Figure 3.13 (d)).

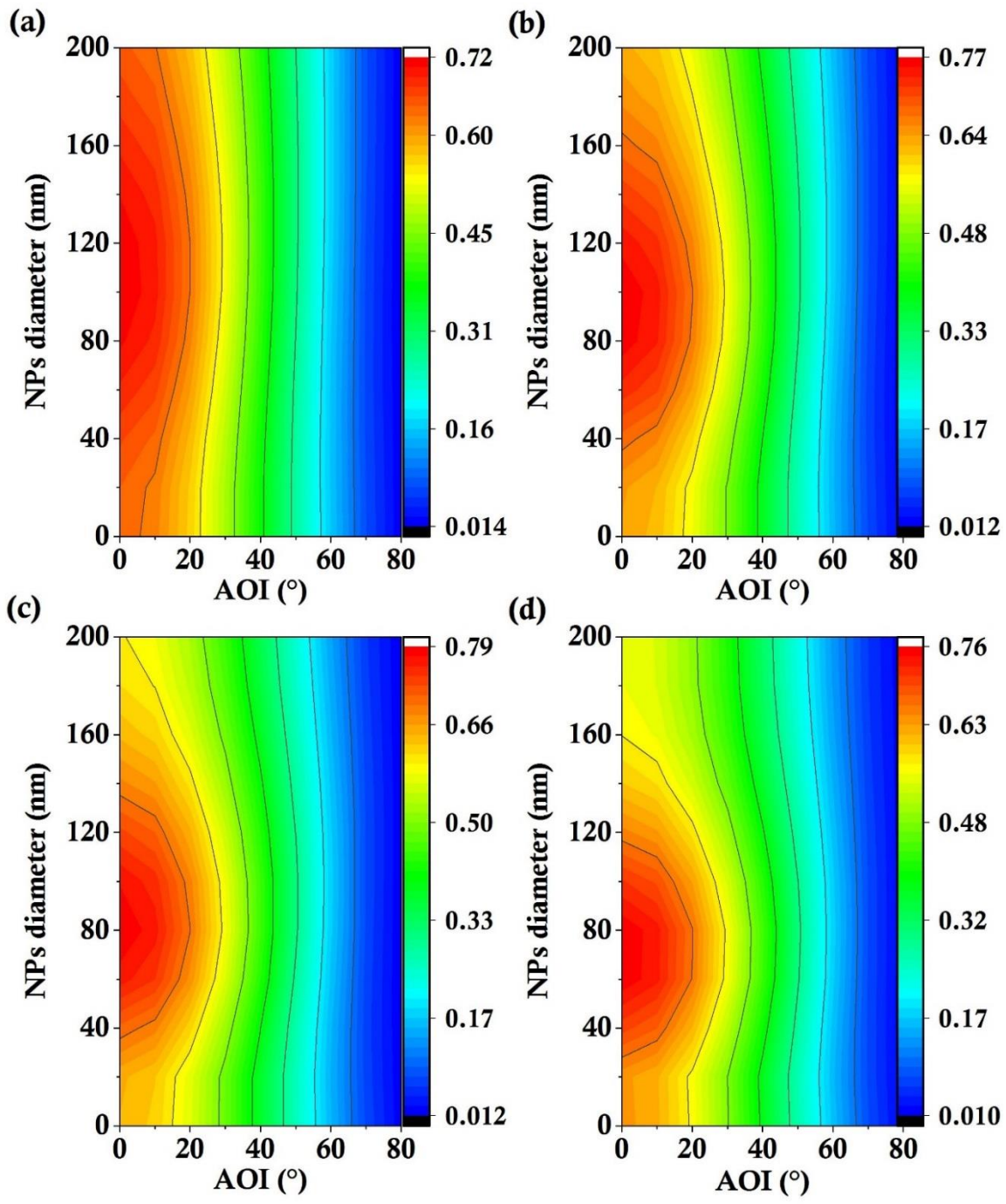

Figure 3.10 Weighted solar power transfer (P_w) from Ag – NPs nanocomposite layer on n-GaAs layer at volume fraction (a) f = 0.10, (b) f = 0.20, (c) f = 0.30, and (d) f = 0.40.

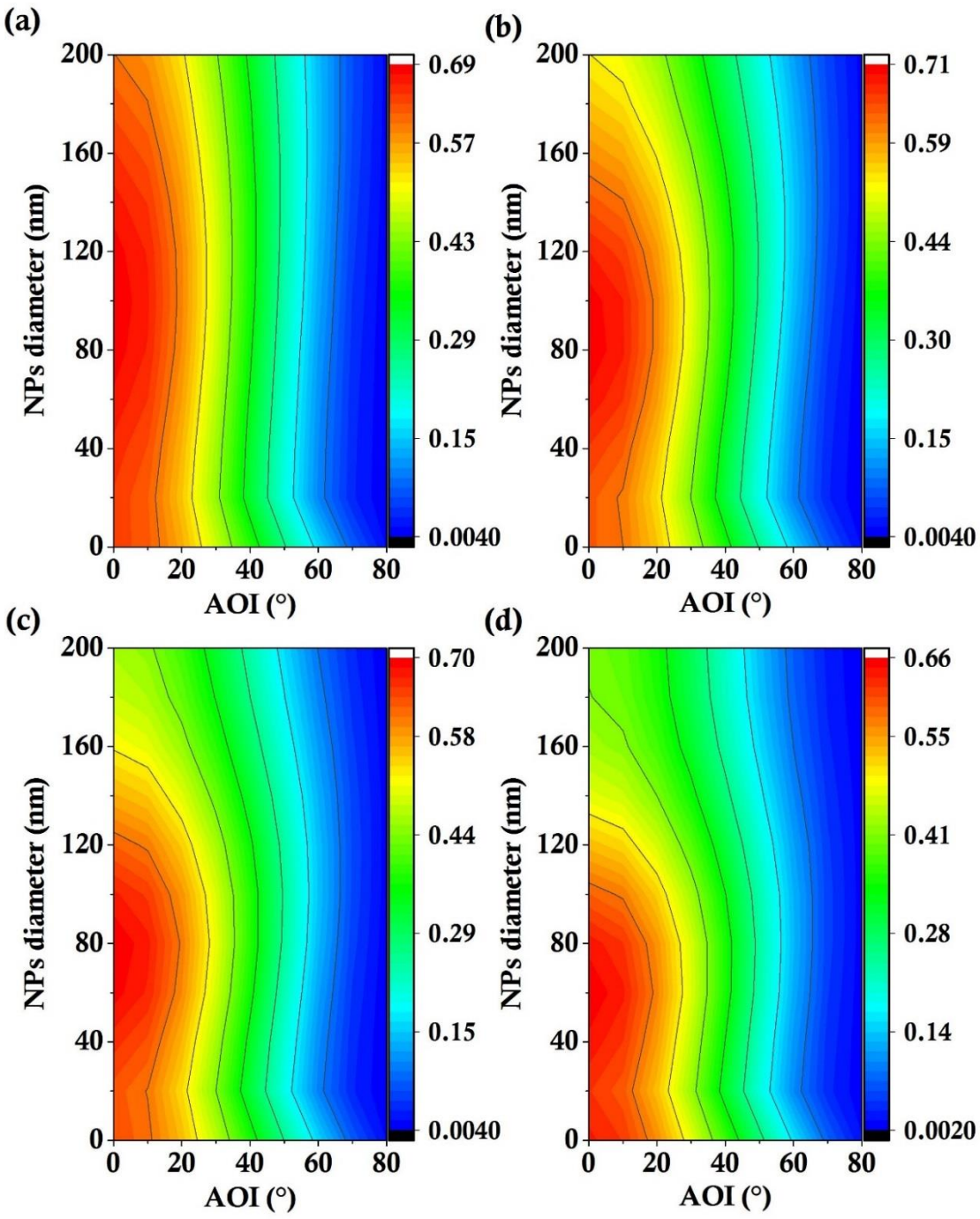

Figure 3.11 Weighted solar power transfer (P_w) from Au – NPs nanocomposite layer on n-GaAs layer at volume fraction (a) f = 0.10, (b) f = 0.20, (c) f = 0.30, and (d) f = 0.40.

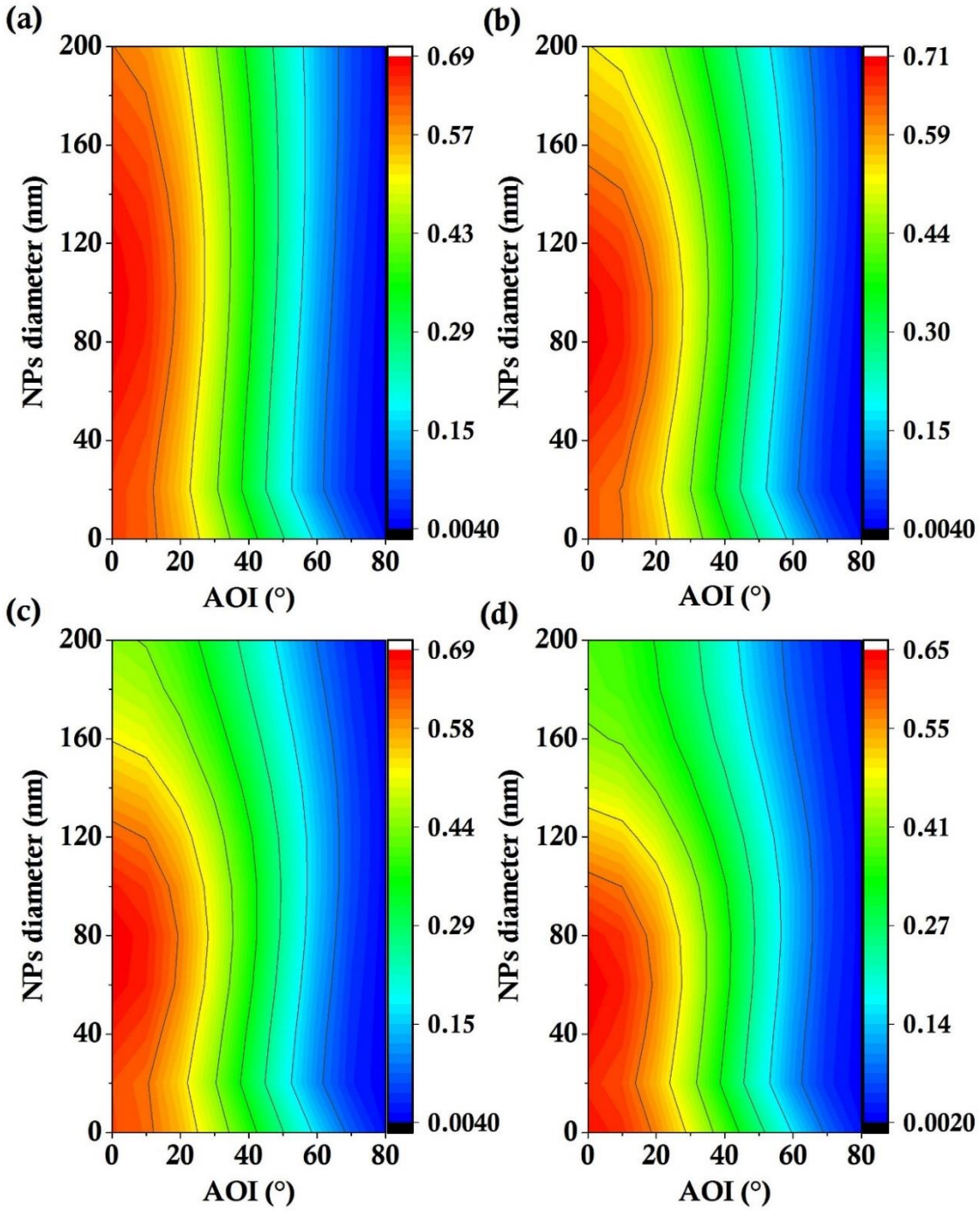

Figure 3.12 Weighted solar power transfer (P_w) from Cu – NPs nanocomposite layer on n-GaAs layer at volume fraction (a) f = 0.10, (b) f = 0.20, (c) f = 0.30, and (d) f = 0.40.

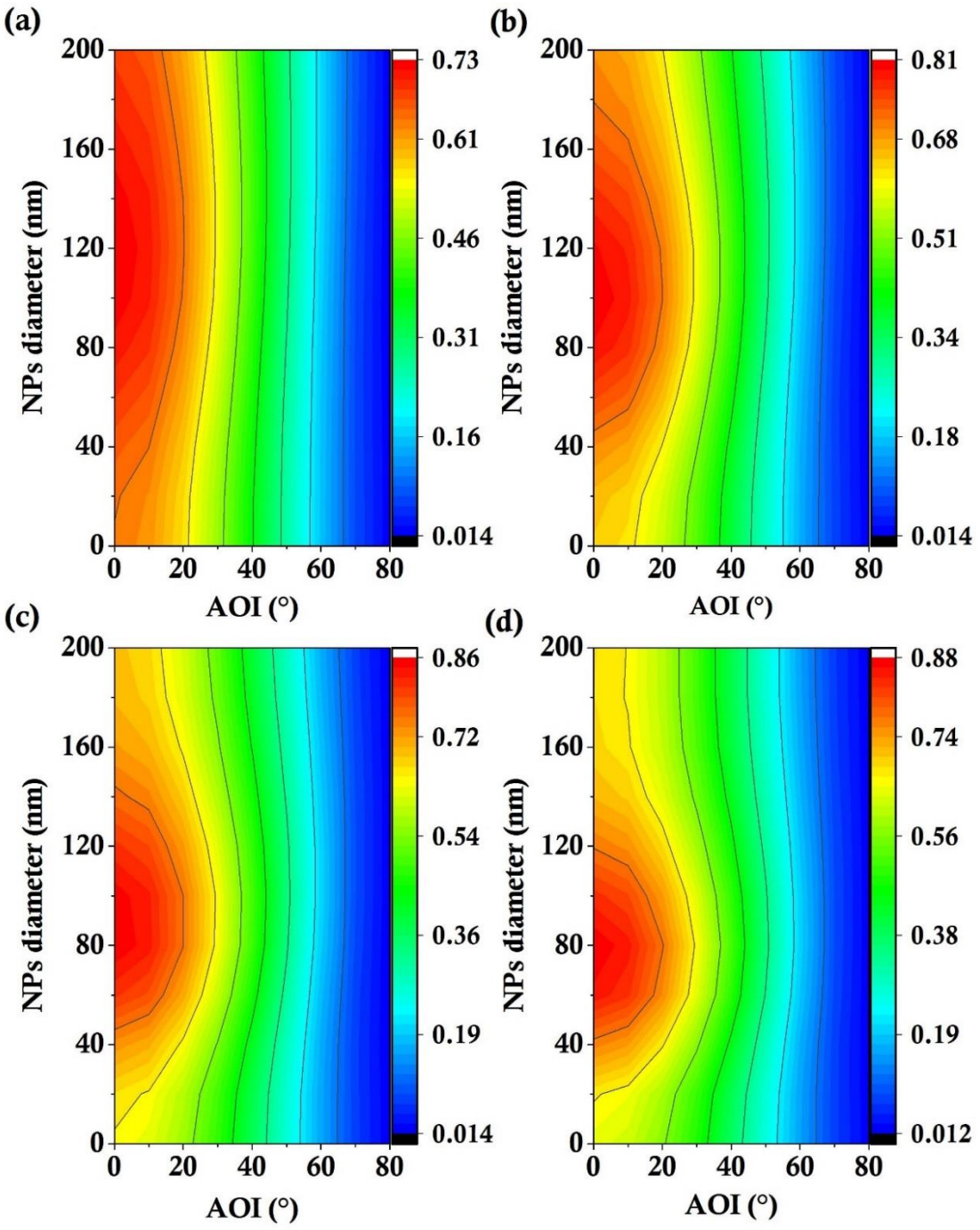

Figure 3.13 Weighted solar power transfer (P_w) from Al – NPs nanocomposite layer on n-GaAs layer at volume fraction (a) f = 0.10, (b) f = 0.20, (c) f = 0.30, and (d) f = 0.40.

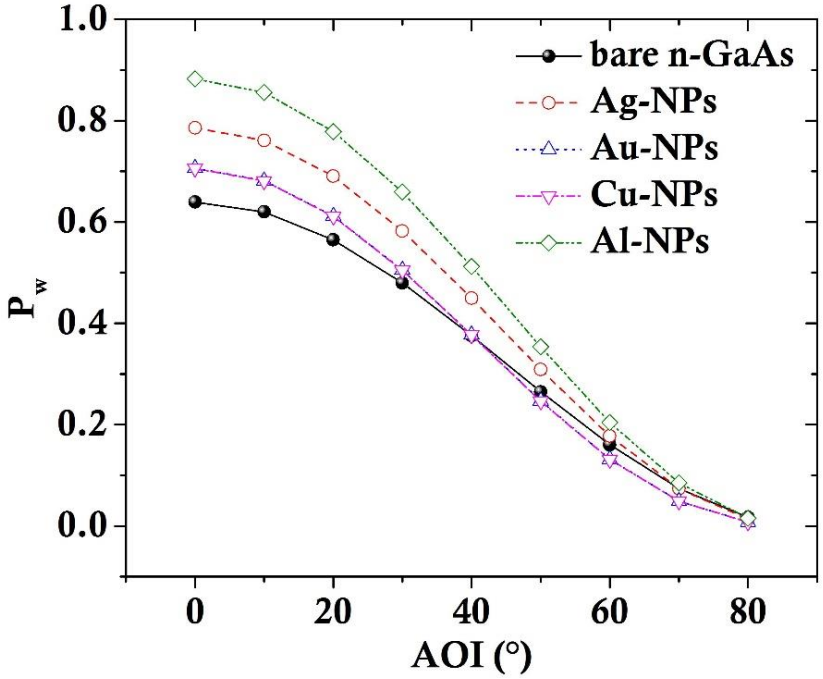

Figure 3.14 Summary of weighted solar power transfers (P_w) from nanocomposite layers with NPs: Ag – NPs (d = 80 nm, f = 0.30), Au – NPs (d = 80 nm, f = 0.20), Cu – NPs (d = 80 nm, f = 0.20), Al – NPs (d = 80 nm, f = 0.40) into n-GaAs layer. 0° AOI is corresponding to normal incidence.

The best weighted solar power transfer (P_w) from the 2D array of metal NPs distributed in the host medium (air) have been summarized in Figure 3.14. Ag – and Al – NPs have shown wide-angle improvements in the power transfer. Surprisingly, Al – NPs have performed better than all other metal NPs. The localized surface plasmon resonance for Al – NPs of smaller size lies in the UV range. As the NPs' size increases, the localized surface plasmon resonance shifts towards a higher wavelength and becomes wider. This is the reason that P_w is higher for 60 nm – 100 nm Al – NPs sizes. Q_{rad} of Al – NPs is not high in visible range for all sizes (cf. Figure 3.9 (b)). However, the product of the transmittance with the intensity of the solar spectrum becomes higher.

Cu – and Au – NPs have shown poor performance in my calculation comparing to Ag – NPs and Al – NPs. GaAs absorbs in the visible range. Cu – and Au – NPs have localized surface plasmon resonance in the middle of the visible range which is the reason for low Q_{rad} and for high Q_b. From P_w contour plots, it is obvious that high Q_b is destructive for high-power transfer in the absorber layer (n-GaAs). Core-shell NPs have been studied and demonstrated to reduce the backscattering and enhance the forward scattering which can be a solution of high Q_b [111].

Metal NPs support the localized surface plasmon resonance with high radiative efficiency. Ag – NPs are the preferred one in this case because of low absorption loss and high optical cross-section comparing to others (Cu –, Au – and Al – NPs) [112]. However, this is not the only factor when considering the choice of metals. For example, Ag forms an oxide layer when it comes in contact with the atmosphere. This oxide layer is absorbing and dampens the radiation property of NPs. Whereas, Au doesn't form the oxide layer and Al's oxide layer is non-absorbing which doesn't negatively affect the optical property of Al – NPs [113], [114]. The oxide layer which forms on Cu damps the resonance [115]. The selection of metal NPs also dictated from a fabrication point of view.

3.4 CONCLUSIONS

I performed a theoretical study on metal NPs (Ag, Au, Cu, and Al) with an absorber layer (n-GaAs) over a wide AOI of the AM1.5 solar spectrum. An analytical model is developed for the analysis of power transfer from the

nanocomposite layer of NPs of arbitrary sizes which are spread in a 2D array on the surface of the absorber layer. The analysis concluded that the scattering efficiency doesn't present a full picture of the high – power transfer in the absorber layer because the backscattering efficiency is also high when the scattering efficiency is high. NPs which have high backscattering efficiency, are good to use on the rear side but not on the front side. For the high – power transfer, balance among all the efficiencies such as scattering, absorption, and backscattering efficiency is required. The comparative study revealed that Al – NPs gives the best performance among Ag –, Au –, Cu –, and Al – NPs at normal incidence with a 38.28 % increase in the reference power transfer value. Wide-angle improvement has also been noticed in this case. As discussed in the introduction section of this chapter, only specular transmission of the incident sunlight in the absorber layer has been considered in the current model. However, NP behaves like a dipole scatterer [105]. The dipole scattering causes a radiation pattern of the transmitted sunlight in the absorber layer. Considering this factor, the weighted solar power transfer can be improved further which will be discussed in the next chapter.

4

NANOPARTICLES MEDIATED LIGHT TRANSMISSION

4.1 INTRODUCTION

In this chapter, I formulate hybrid NPs' based ARCs on a Si/GaAs – substrate and develop a model. The developed model is a combination of the Dipole model [104], the TMM method (cf. Section 3.2.2), and Mie theory (cf. Section 2.5.1). When the sunlight incident on a rough interface (hybrid ARC layer: NPs embedded in a SiN thin film, in my case), the reflectance from the interface divides into two parts – specular reflectance (R_s) and diffuse reflectance (R_d), similarly for transmittance as shown in Figure 4.1 [116]. The specularly reflected light is obtained by the efficient TMM method of multilayer structures. Whereas for the diffusely reflected light, angular power distribution

of radiation by an NP in the substrate is calculated. Some of the results have been published in Ref. [2]–[4]. In the current study, it is assumed that the specular and diffuse reflectance occurrences are independent of each other and don't interfere with each other.

4.2 DIPOLE MODEL

In a dipole model, the NP is assumed as a dipole oscillating at its resonant frequency. The dipole generally excites in the direction of polarization of the incident light (regardless of front and back illumination). Therefore, the excitation angle changes with the AOI of the sunlight. Mertz [104] has formulated a dipole radiating at a distance z_0 above a substrate in a medium of refractive index n_h and found an expression for the angular power distribution of the scattered light from the NP in air and in the neighboring substrate which is as follows

$$L_{\phi}(\theta) = L_{\parallel}^{s,p}(\theta) * \ sin^2(\phi) + L_{\perp}^{p}(\theta) * cos^2(\phi) + Re\left[L_X^p(\theta)\right] * \sin 2\phi \tag{4.1}$$

where θ is observation angle; s and p in the superscript are corresponding to s – and p – polarized light, respectively; ϕ is the inclination of the dipole from vertical and

$$L_{\parallel}^{s,p}(\theta) = L_{\parallel}^{s}(\theta) \ * sin^2(\varphi) + L_{\parallel}^{p}(\theta) * cos^2(\varphi), \tag{4.2}$$

$$L_{\parallel}^{s}(\theta_{in}) = \frac{n_0}{n_{in}} * |K_{\parallel}^{s}(\theta_{in})|^2 \tag{4.3a}$$

$$L_{\parallel}^{s}(\theta_{out}) = \frac{n_{out}}{n_0} * |K_{\parallel}^{s}(\theta_{out})|^2 \tag{4.3b}$$

$$L_{X}^{p}(\theta_{in}) = \frac{n_0}{n_{in}} * K_{\parallel}^{p}(\theta_{in}) * \ K_{\perp}^{p}(\theta_{in})^* \tag{4.3c}$$

$$L_{X}^{p}(\theta_{out}) = \frac{n_{out}}{n_0} * K_{\parallel}^{p}(\theta_{out}) * \ K_{\perp}^{p}(\theta_{out})^* \tag{4.3d}$$

with corresponding definitions for $L_{\parallel}^{p}$ and $L_{\perp}^{p}$ as $L_{\parallel}^{s}$. θ_{in} and θ_{out} are input and output angle of the incident light, similarly the refractive indices; φ is rotation angle in the plane. The definitions for Ks are,

$$K_{\parallel}^{p}(\theta_{in}) = \cos(\theta_0)\big[-\exp(-ik_0\, z_0\, cos\ (\theta_0)) + r_p \exp(ik_0\, z_0 \cos(\theta_0))\big] \tag{4.4a}$$

$$K_{\parallel}^{s}(\theta_{in}) = \exp(-ik_0\, z_0\, cos\ (\theta_0)) + r_s \exp(ik_0\, z_0 \cos(\theta_0)) \tag{4.4b}$$

$$K_{\perp}^{p}(\theta_{in}) = \sin(\theta_0)\big[-\exp(-ik_0\, z_0\, cos\ (\theta_0)) - r_p \exp(ik_0\, z_0 \cos(\theta_0))\big] \tag{4.4c}$$

for externally incident light, and

$$K_{\parallel}^{p}(\theta_{in}) = -t_p \cos(\theta_0) \exp(ik_0\, z_0 \cos(\theta_0)) \tag{4.5a}$$

$$K_{\parallel}^{s}(\theta_{in}) = t_s \exp(ik_0\, z_0 \cos(\theta_0)) \tag{4.5b}$$

$$K_{\perp}^{p}(\theta_{in}) = t_p \sin(\theta_0) \exp(ik_0\, z_0 \cos(\theta_0)) \tag{4.5c}$$

for internally incident light, where k_0 and θ_0 is the wave-vector magnitude and AOI of the light in the incident medium, respectively. r_s, r_p, t_s and t_p are the Fresnel reflection and transmission coefficients of s – and p – polarized light (cf. Section 3.2).

The diffused reflectance and transmittance can be given from the above equations as

$$\left.\begin{aligned} \boldsymbol{R_d} &= Q_{sca} * \frac{1}{\pi}\int_0^{\pi} L_{\phi}(\theta)(reflected)\ d\theta \\ and & \\ \boldsymbol{T_d} &= Q_{sca} * \frac{1}{\pi}\int_0^{\pi} L_{\phi}(\theta)(transmitted)\ d\theta \end{aligned}\right\} \tag{4.6}$$

where Q_{sca} is the scattering efficiency of NPs (cf. Section 2.5). The sum of both reflectances (specular and diffuse) is the total reflectance from the front surface of the device such as

$$\boldsymbol{R} = f * \boldsymbol{R_d} + (1 - f) * \boldsymbol{R_s} \tag{4.7}$$

where f is a fraction of the cross-section area covered by NPs at the front surface. The dipole approximation is valid when the distance between NPs is of the order of or more than their diameters such that $f < 0.75$[§].

[§]*Here, f is a surface cross-section fraction and calculated as follows*

From Section 3.2, the dipole model is valid when the volume fraction (f_1) of NPs in the ARC layer is less than 50 %. So,

$$f_1 < 0.5$$

The volume fraction in terms of the device structure variables is given by

$$f_1 = \frac{N * (4\pi r^3/3)}{l * b * h}$$

where N is the NPs' no. density, and r is the radius of NPs. l, b, and h are the length, breadth, and height of the layer, respectively.

The surface cross-section area fraction can be given by

$$f_2 = \frac{N * (\pi r^2)}{l * b}$$

From the above equations,

$$f_2 = 1.5 * f_1$$

Hence, for the dipole model, the surface cross-section area fraction should be less than 75 % or $f_2 < 0.75$.

The ARCs in solar cells are designed to minimize the reflectance and maximize the transmittance across the wavelength range of interest. So that I have calculated weighted solar power transmittance (T_w):

$$T_w = \frac{\int_{\lambda_1}^{\lambda_2} T(\lambda) * S(\lambda)\, d\lambda}{\int_{\lambda_1}^{\lambda_2} S(\lambda)\, d\lambda} \tag{4.8}$$

where $T(\lambda)$ $(= 1 - R(\lambda) - A(\lambda))$ and $S(\lambda)$ are the transmittance and intensity of the AM1.5 solar spectrum at wavelength λ. λ_1 and λ_2 are the minimum and maximum allowed wavelengths. $A(\lambda)$ and $R(\lambda)$ are the absorption and reflection at wavelength λ, respectively.

The hybrid ARC made of a nanocomposite layer in which NPs are distributed in a 2D array of an equal period in a dielectric SiN matrix bounded with air and the substrate is investigated. A schematic of the simulated device structure is shown in Figure 4.1. Optical constants of metal NPs (cf. Figure 3.5) and refractive index of SiN (cf. Figure 4.2) for the calculations are taken from Palik [109]. Linear interpolation is used to fit the optical constants to desired step size. The solar spectrum used in the calculation is taken from Ref. [25] and is shown in Figure 3.3 (for Si, the absorption range is 300 nm – 1100 nm). An angular dependent solar spectrum is ignored as it has no effect on the reflectance calculation. The study has been done on four different NPs' densities in the nanocomposite layer. The nomenclature of the nanocomposite layer: Ag (40 %) / SiN refers to that 40 % surface cross-section area is covered by Ag – NPs and rest are SiN. In the simulation, the SiN layer thickness is kept at 70 nm and the NPs' radius at 35 nm.

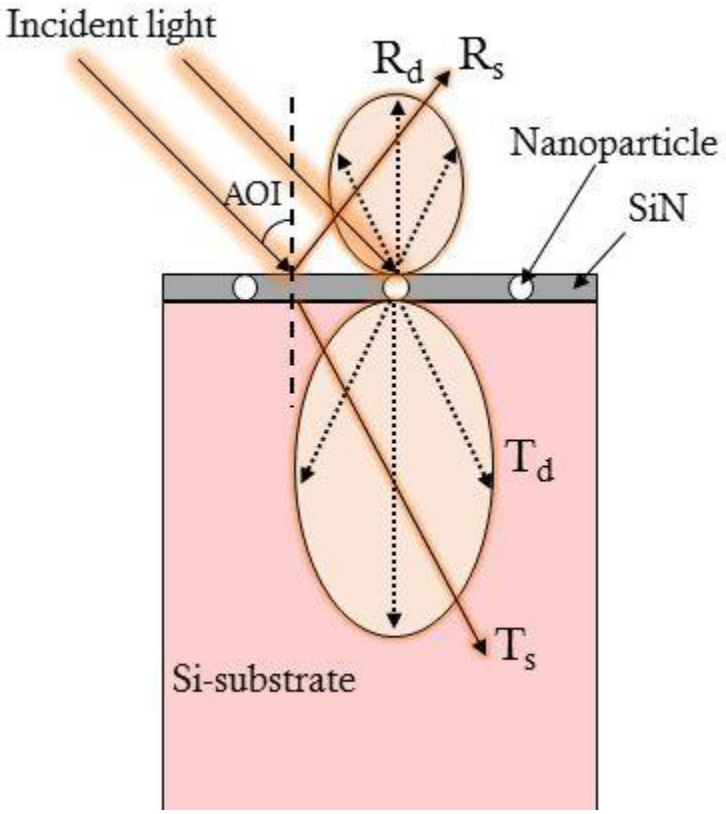

Figure 4.1 Schematic of the simulated device structure for specular and diffuse reflection/transmission.

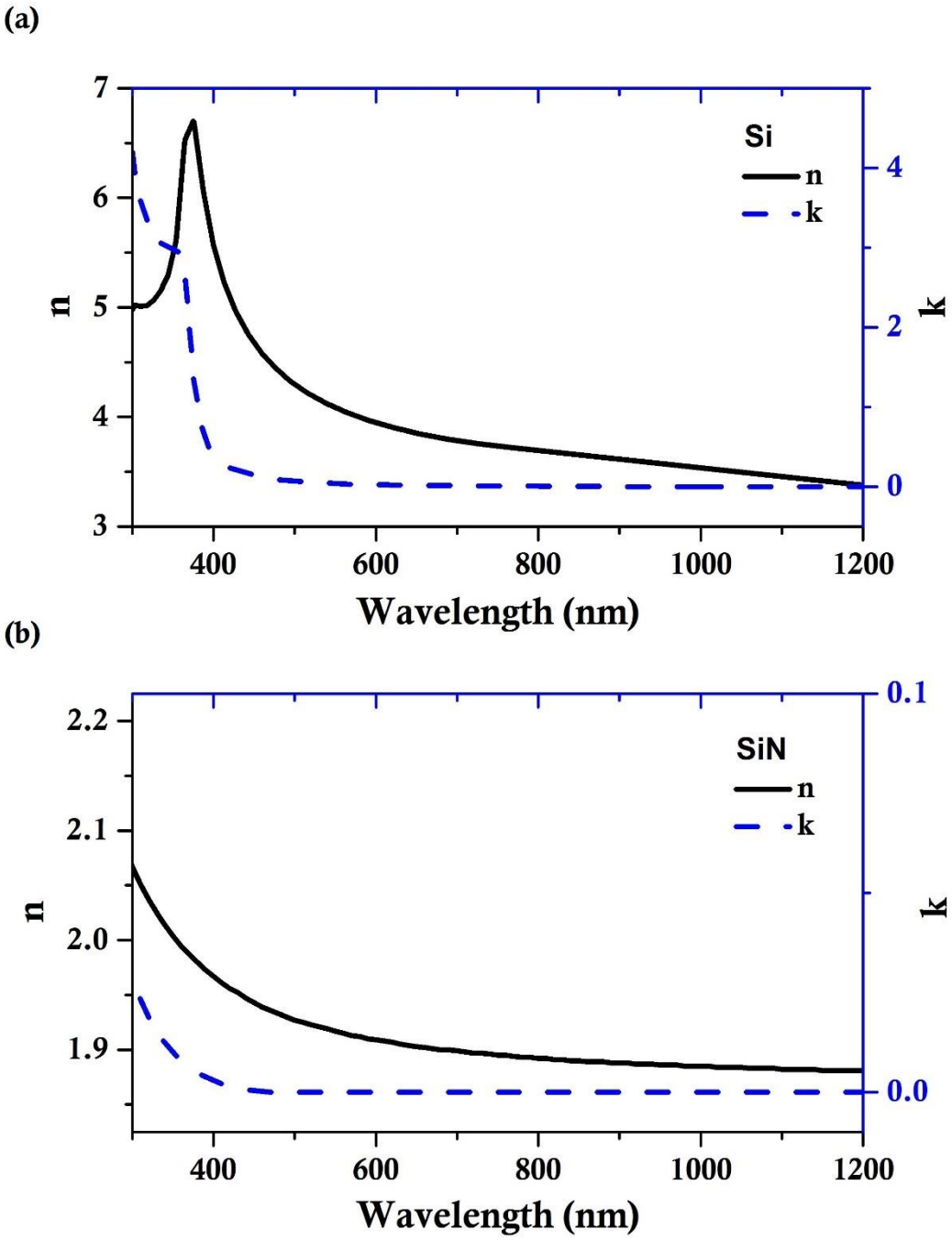

Figure 4.2 Complex refractive index of (a) Si (n & k), and (b) SiN (n & k).

4.3 RESULTS AND DISCUSSION

4.3.1 Metal Nanoparticles

Figure 4.3 shows the scattering and absorption efficiency of metal NPs of radius 35 nm. This has been calculated similarly as in Chapter 3. From the efficiency spectra, it is noticed that Ag – and Au – NPs show strong dipole resonance scattering peaks in the visible range at 589 nm and 666 nm, respectively. Cu – NP has a lower peak than Ag – and Au – NPs in the same range at 643 nm. Al – NP has a relatively weak resonance peak (cf. Figure 4.3 (a)). However, on average, Au – and Cu – NPs have shown more absorption than others (cf. Figure 4.3 (b)). A new peak for Ag – NP has been observed in the absorption spectra at 472 nm which corresponds to a higher-order resonance mode. In NPs, the primary resonance peak is known as a dipole mode resonance. Higher-order modes can also be excited for sufficiently large particles. The peak positions of higher-order modes are at a shorter wavelength than the primary one, and also narrower which can be seen in Figure 4.3 (b). In my case, the higher-order mode is only visible for Ag – NP in the absorption spectra.

The radiative efficiency of NPs is the most useful quantity of NPs for the ARC application. The efficiency spectra have been shown in Figure 4.4. It shows that Ag – NP has high radiation at 575 nm near to that the solar spectrum has maximum intensity. The higher-order modes have a negative effect on the radiative efficiency of NPs, however, they can still achieve large radiative efficiencies [117]. This is the reason that Ag – NP still shows the highest radiative efficiency. Al – NP also follows the solar spectrum curve same as the Ag – NP. This makes both promising to incorporate in the conventional SiN ARC.

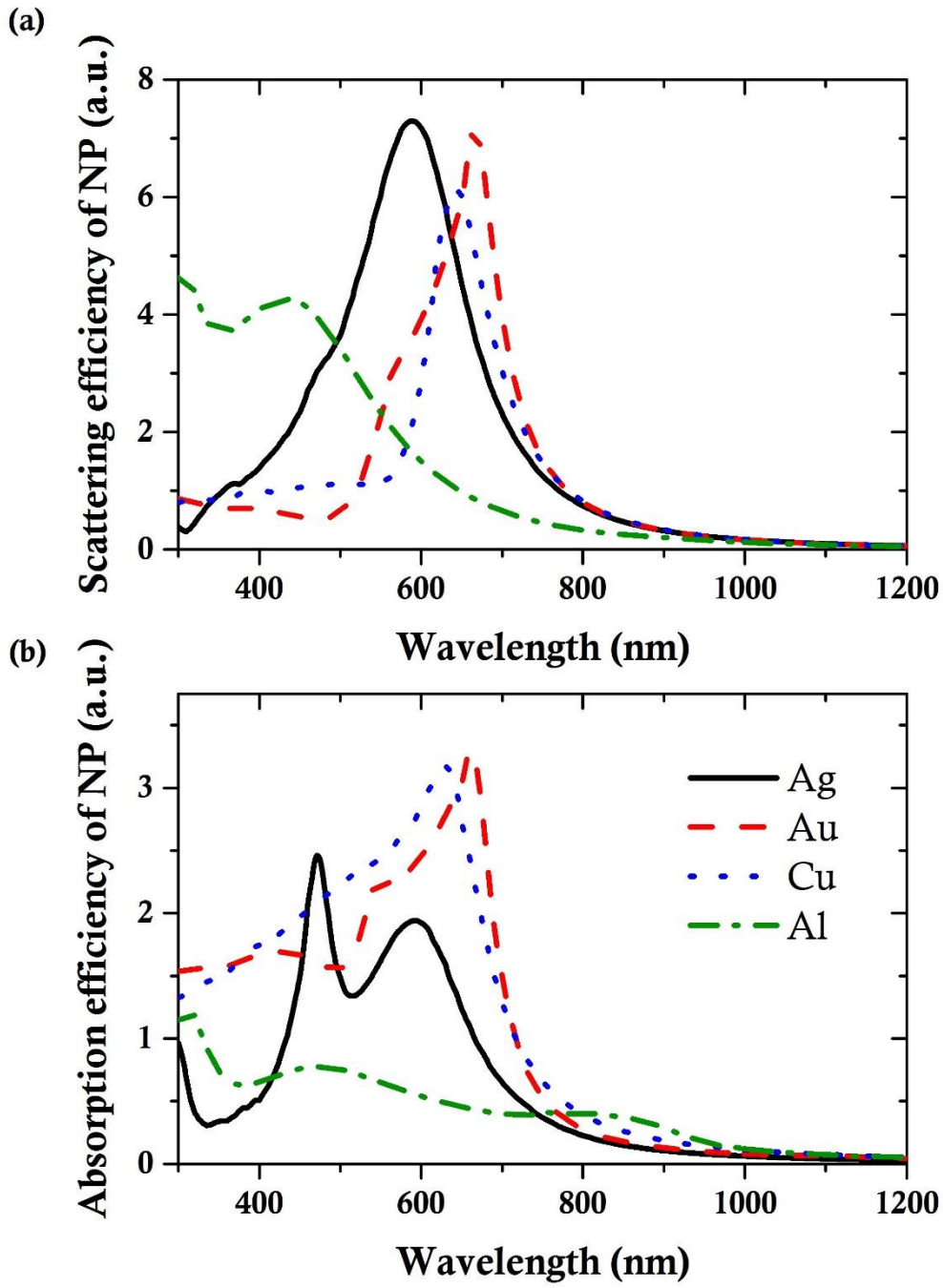

Figure 4.3 (a) Scattering, and (b) absorption efficiencies of NPs (radius = 35 nm)

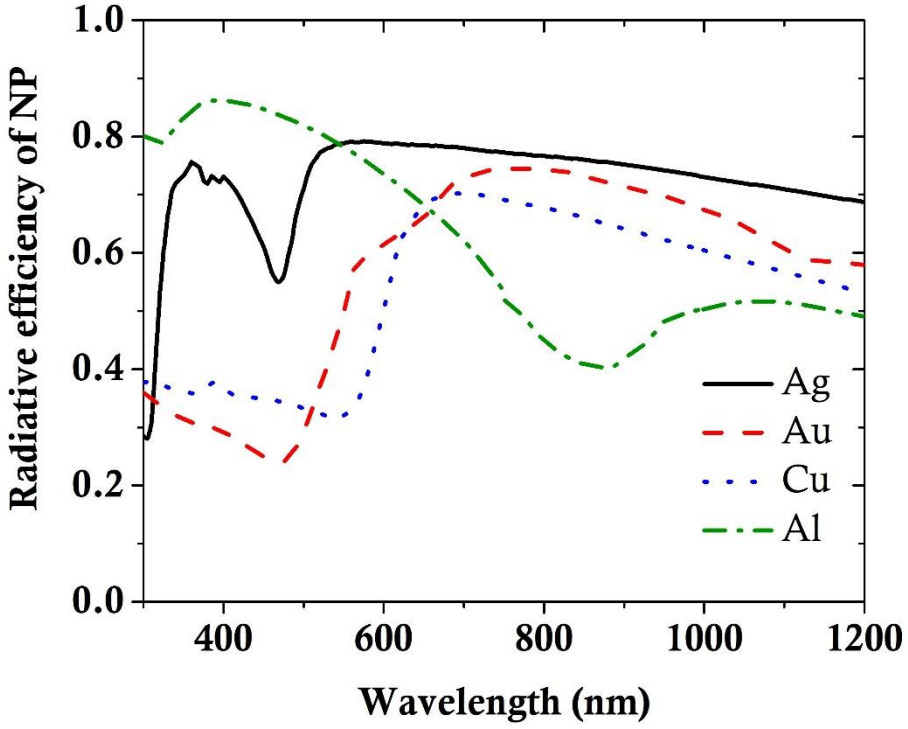

Figure 4.4 Radiative efficiency of NPs (radius = 35 nm)

Whereas Cu – and Au – NPs show weak radiative behavior in this region. Therefore, I didn't perform the simulation study on these NPs.

Figure 4.5 shows reflectance spectra of the simulated device structure with Ag – NPs in the SiN layer at various AOI. At normal incidence (AOI = 00°), the conventional SiN ARC shows the best performance. The reflectance minimum, in this case, is obtained at 536 nm. However, incorporation of NPs in the conventional ARC increases the reflection and the hybrid ARCs show the worst performance. The hybrid ARC (Ag (70%) / SiN) shows around 5 % reflection of the incident sunlight at normal incidence and 536 nm wavelength. On average, 10 % to 20 % reflection of the incident light from the entire solar spectrum has been noticed for the hybrid ARC layer (cf. Figure 4.5 (a)). The solar spectrum has maximum intensity near 536 nm wavelength. Therefore, Ag – NPs with SiN is not a good combination at normal incidence. As the AOI of the light changes from normal to non-normal angles, an increase in the reflection near the solar spectrum maxima has been noticed in the reflection spectra of SiN ARC. This is caused by constructive interference at the surface due to the reflected light from the internal interface (SiN/Si interface). The constructive interference is an angle-dependent physical phenomenon that is more effective when the incidence angle goes away from the normal incidence in this case (cf. Section 2.2). An increase in the reflection can be seen in every reflection spectra of SiN ARC, however, a relative decrease in the reflection has been noticed in the reflection spectra of hybrid ARC at non-normal angles. At 60° AOI, the reflectance spectra of SiN ARC and hybrid ARC become almost equal. And after this, the hybrid ARCs outperform SiN ARC. Ag (70%) / SiN

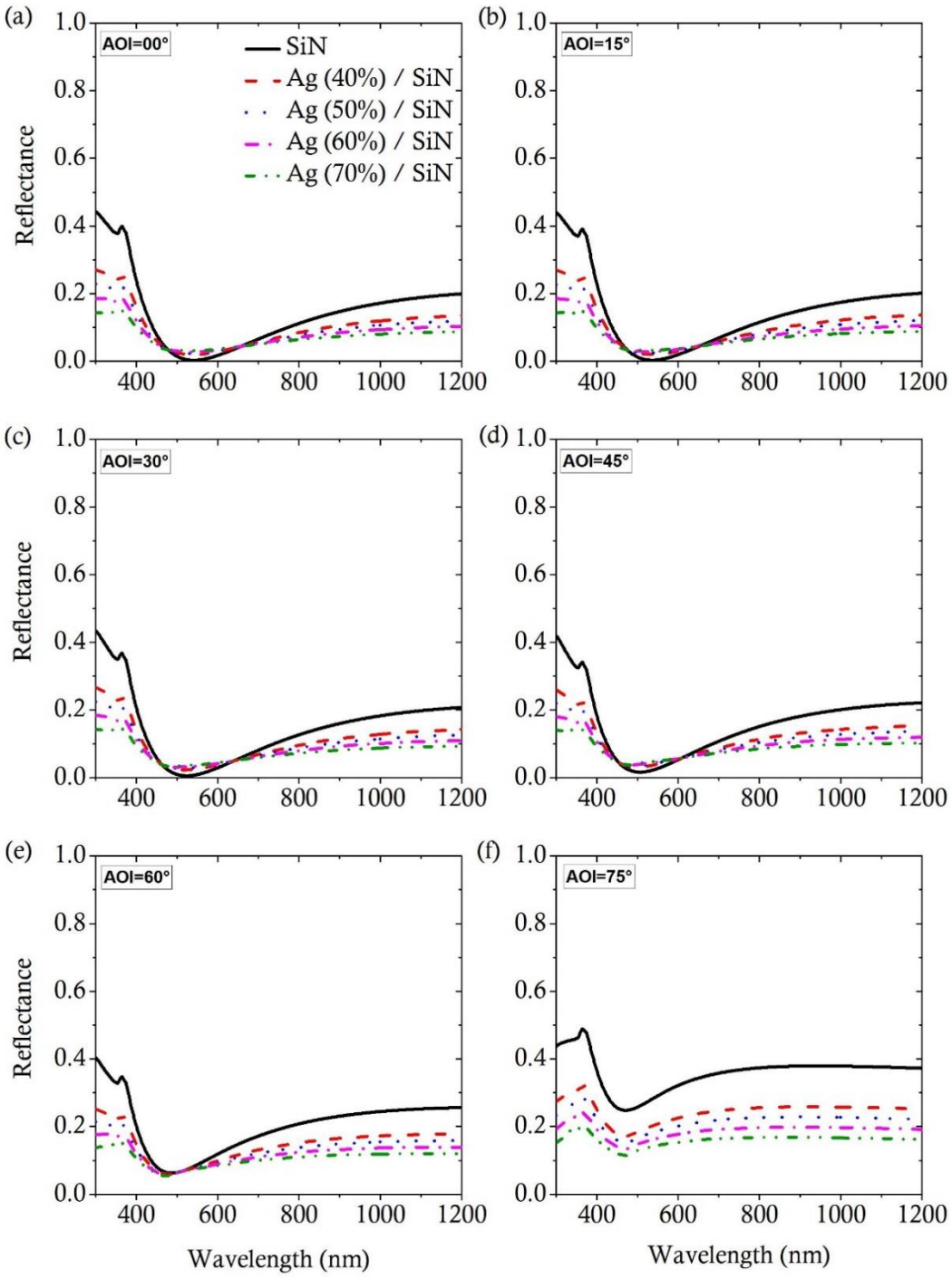

Figure 4.5 Reflectance spectra of Ag – NPs / SiN layer versus the light operating wavelength.

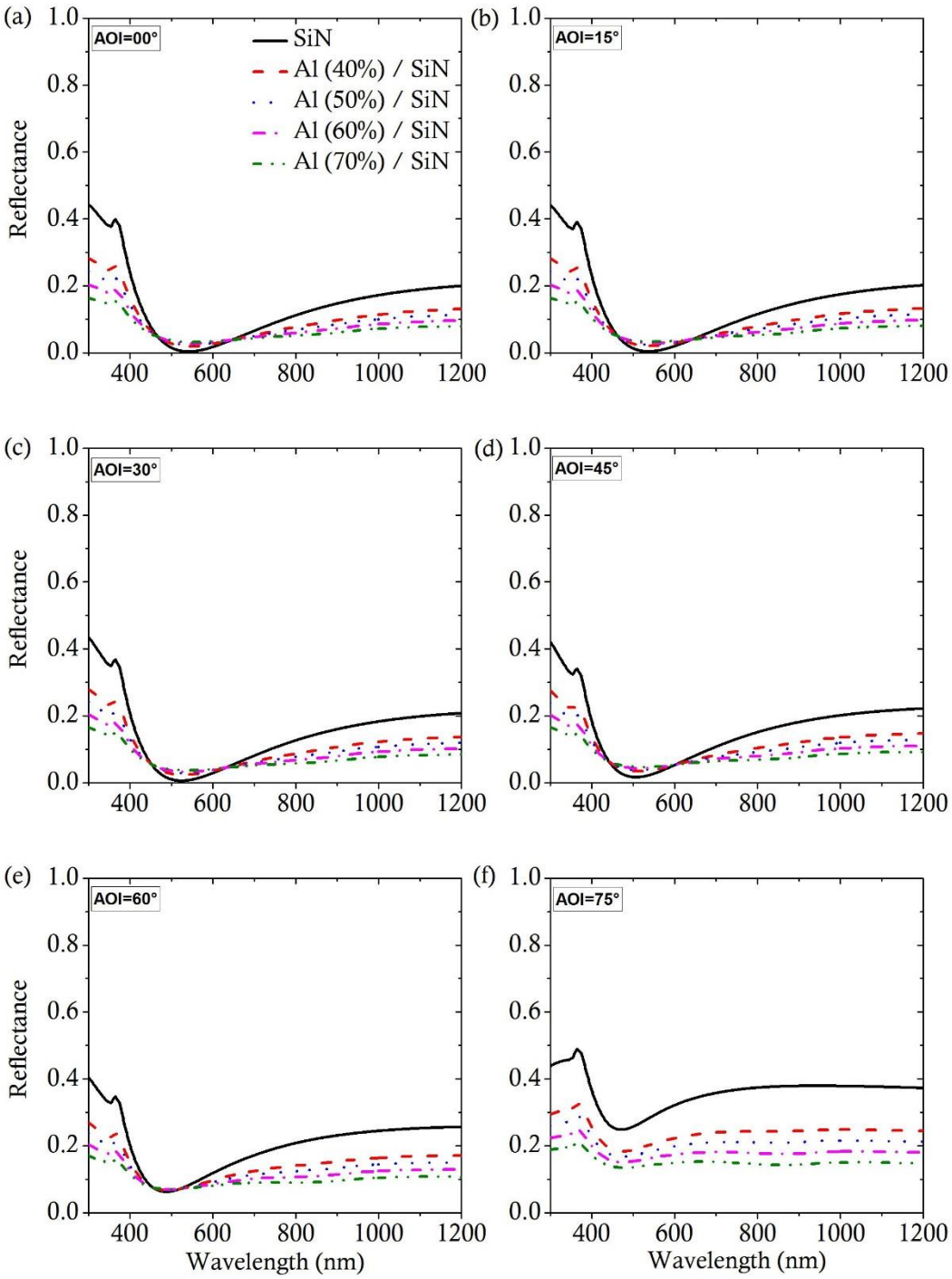

Figure 4.6 Reflectance spectra of Al – NPs / SiN layer versus the light operating wavelength.

ARC has shown the best performance among all the hybrid ARCs at ≥ 60° AOI. At 75° AOI, SiN ARC has shown around 40 % reflection, on average. However, Ag (70%) / SiN has the maximum reflection of 20 % at 350 nm. When the AOI of the light for SiN ARC reaches near to its critical angle, the reflectance becomes higher as the constructive interference becomes more prominent, whereas NPs don't show this behavior and perform better at higher AOI.

Figure 4.6 shows the reflectance spectra of the simulated device structure with Al – NPs at various AOI. Al – NPs have also exhibited improvement in ARC performance at higher AOI. This follows the same pattern as Ag – NPs embedded in SiN ARC. The difference in reflectance spectra between Ag – NPs and Al – NPs can be seen only at higher AOI, at which the reflectance spectra of NPs based ARC follows the same trend as the radiative efficiency curves of NP (cf. Figure 4.4). In the case of Al – NPs, the reflectance spectra of SiN ARC and hybrid ARC becomes equal at AOI = 60° near 500nm wavelength (cf. Figure 4.6 (e)).

The electric field distribution profile of the sunlight radiated from an Ag – NP in the neighboring substrate at various AOI is shown in Figure 4.7. The Ag – NP and the substrate are assumed as non-absorbing in the field distribution simulation. At higher AOI, it is noticed that the Ag – NP radiates with the same order of intensity as at normal incidence which is the reason that the NPs based ARC performs relatively better than SiN ARC at higher AOI. The distribution profile at normal incidence looks the same as reported in Ref. [118] where various structures such as air/ZnO:Al, $CuGaSe_2$ – SnO_2:F, and SnO_2:F/glass have been simulated with the Dipole model. The angular distribution of radiation in the substrate also benefits in waveguide-based trapping of the incident sunlight. Soller et al. reported that more than 80 % of the sunlight

radiated from a dipole directs into the waveguide mode of silicon-on-insulator [119]. And, Catchpole et al. reported an enhancement in absorption by a factor of 7.5 due to the waveguide mode coupling, experimentally [105].

Figure 4.8 shows T_w curves of SiN ARC and metal NPs based hybrid ARC. T_w curves have been obtained using the transmittance spectra of ARCs (cf. Figure 4.9 & Figure 4.10). In my case, SiN ARC have shown more than 90 % transmittance at normal incidence (0°), as expected. As AOI increases from 0°, T_w is almost constant up to 45° AOI. The light wavelength for maximum T_w value varies very little (between 550 nm to 600 nm) between 0° to 40° AOI and the solar spectrum have almost equal spectral irradiance value in this wavelength range (cf. Figure 3.3). This is the reason for almost constant T_w values up to 40°. And after this it start to decrease slowly. At 74° AOI, the hybrid ARC (Ag – NPs / SiN) and SiN ARC have equal values. After 74° AOI, Ag – NPs based hybrid ARC shows better performance than SiN ARC. In Al – NPs based hybrid ARC, this happens at 78° AOI (cf. Figure 4.8 (b)). Therefore, 74° AOI plays a threshold angle for Ag – NPs based hybrid ARC and 78° AOI for Al – NPs based hybrid ARC. Before this threshold point, SiN ARC performs better and after this threshold point, NPs based hybrid ARC performs better. For comparison, I have also computed T_w for SiN ARC optimized at AOI = 45° and AOI = 75° which are displayed as SiN(45) and SiN(75) curves in Figure 4.8 (a), respectively. Between Ag – NPs and Al – NPs, Ag – NPs performs better than Al – NPs at any AOI which contradicts the conclusions of Chapter 3. In the current model, the radiation from an NP has been calculated

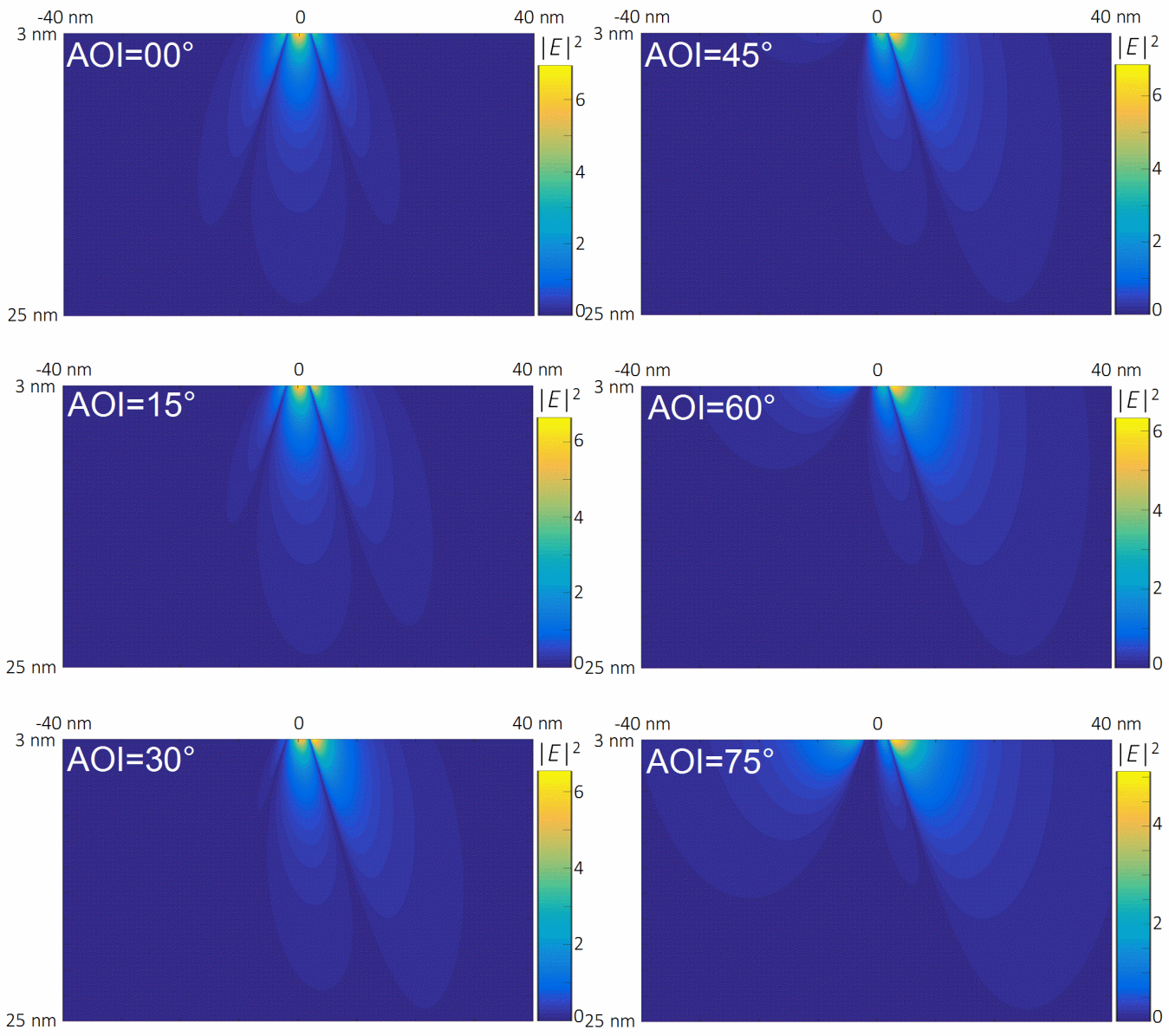

Figure 4.7 Electric field distribution patterns of sunlight (λ = 510 nm) radiated from Ag-NP (radius = 35 nm) in Si substrate. AOI = 00° corresponding to normal incidence.

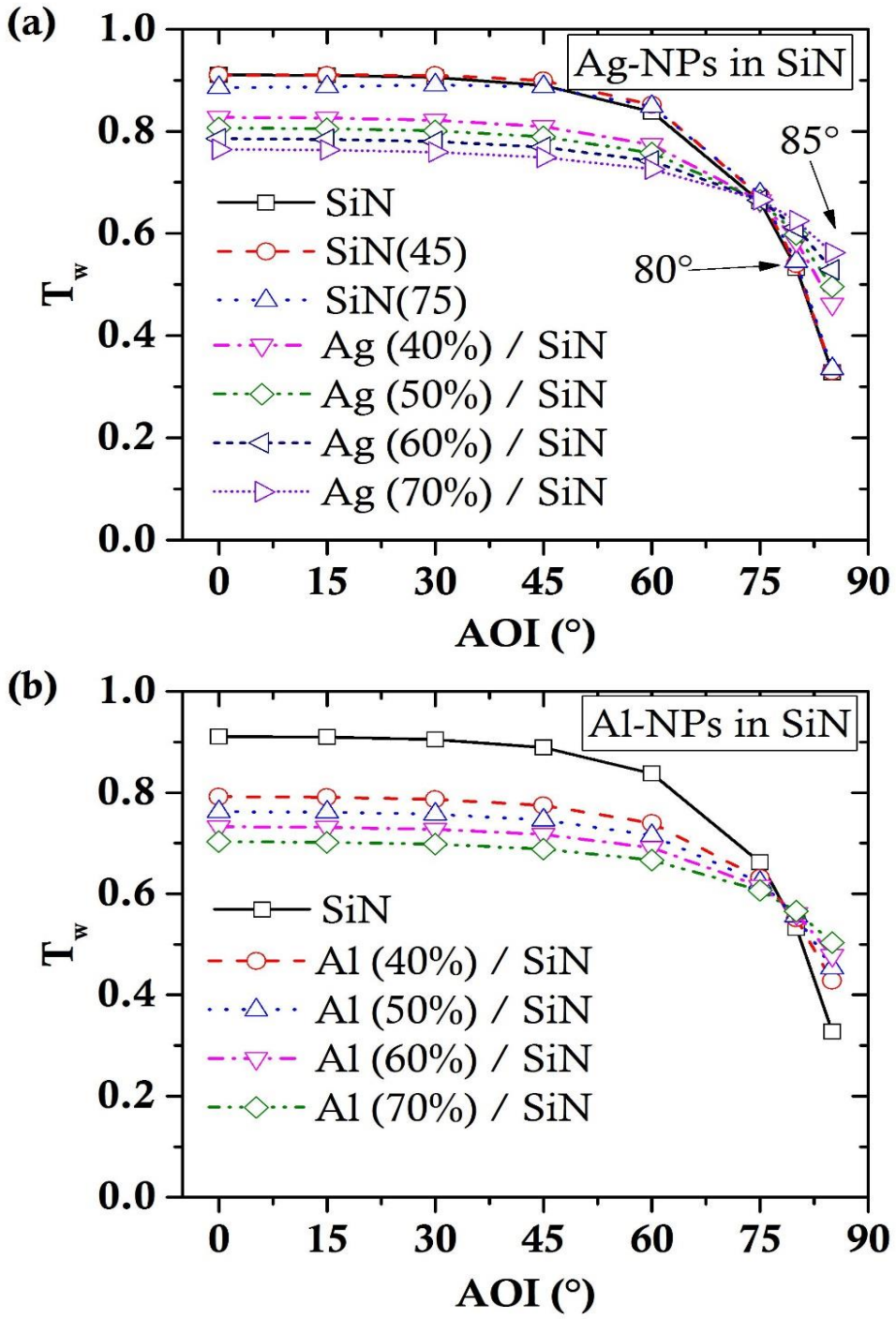

Figure 4.8 Weighted solar power transmittance (T_w) (a) from Ag-NPs/SiN layer, and (b) from Al-NPs/SiN into Si-substrate.

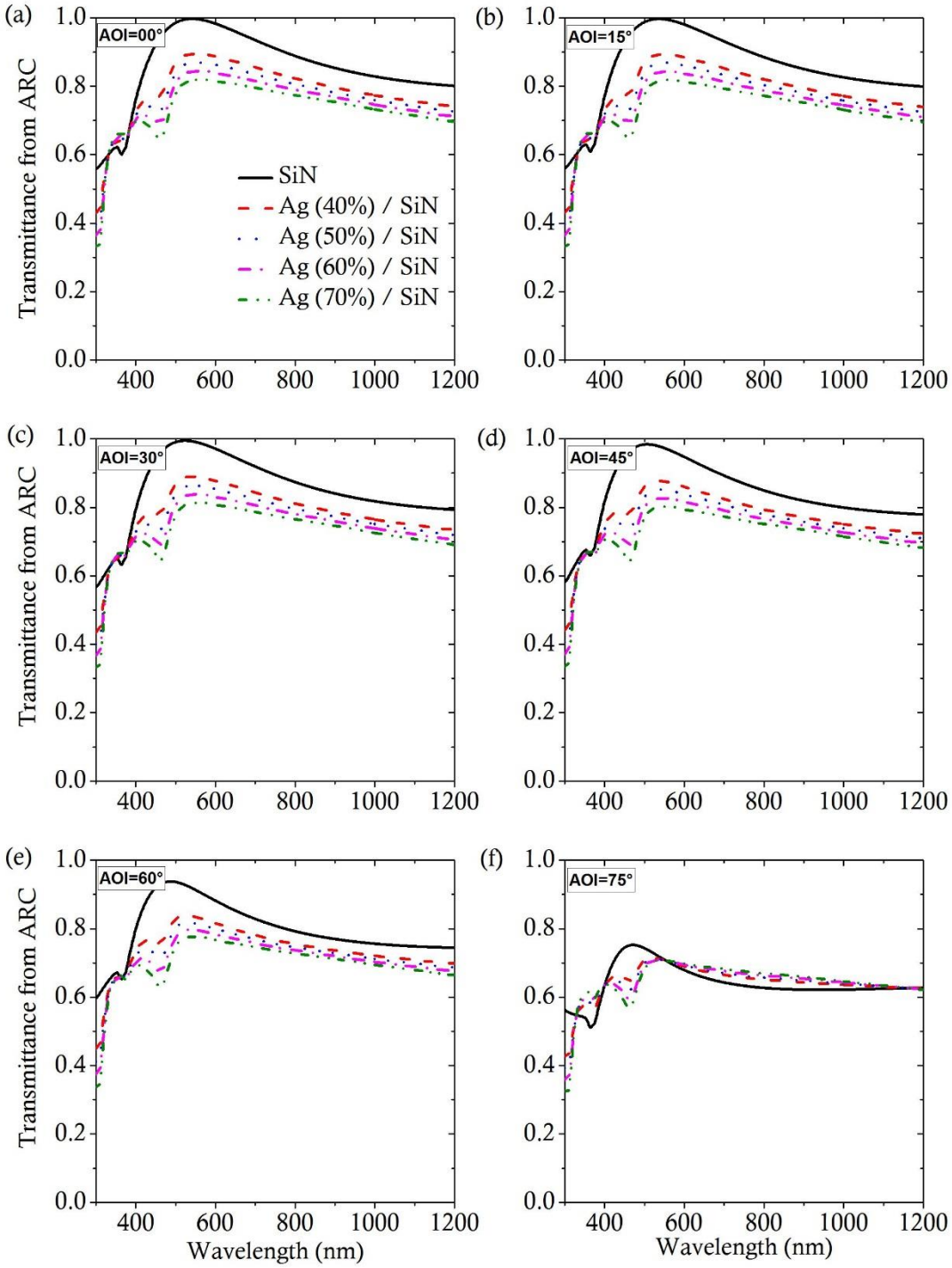

Figure 4.9 Transmittance spectra of Ag-NPs / SiN layer into Si-substrate versus the light operating wavelength.

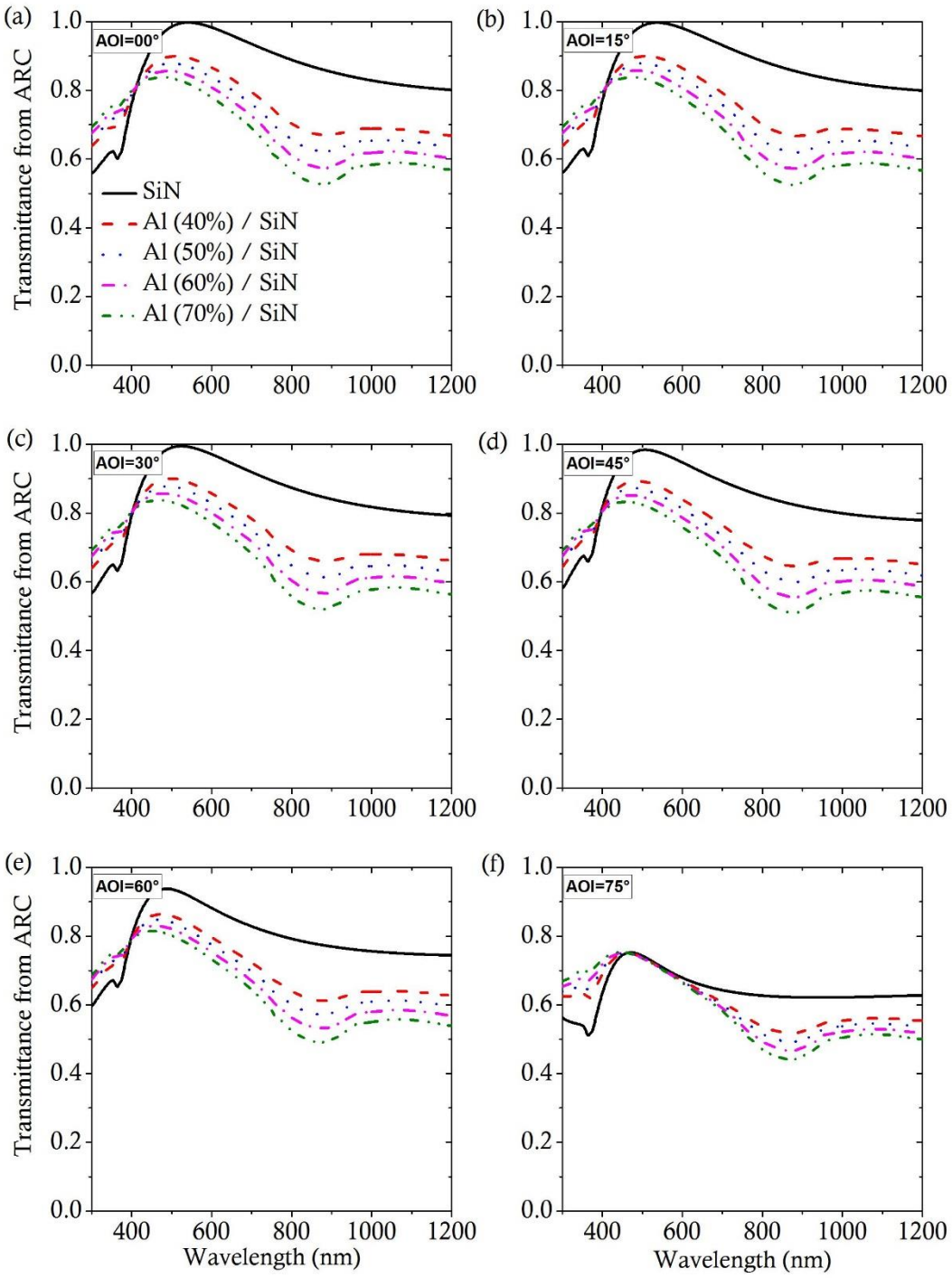

Figure 4.10 Transmittance spectra of Al-NPs / SiN layer into Si-substrate versus the light operating wavelength.

first and then used this to describe the property of a hybrid ARC. However, in extended MG effective medium theory, the radiation property of an NP has been suppressed by assuming an effective thin film medium with only specular reflection and transmission, which overlooks the high radiation property of Ag – NPs in the visible region. Furthermore, higher-order modes of metal NPs have also been neglected in the case of effective medium theory.

Comparing to the reflectance and transmission spectra of Ag –, and Al – NPs based hybrid ARC, it has been noticed that the hybrid ARC shows better performance than SiN ARC near 60° AOI in the reflection, but not in the transmission (Figure 4.9 (e) & Figure 4.10 (e)). This is because of the parasitic absorption in metal NPs, when in fact there is almost no absorption in SiN. This emphasizes the use of NPs with less parasitic absorption as an ARC. NPs with high absorption and scattering properties are good to use as a rear side reflector [120]–[122]. Mendes et al. have presented a study on gold NPs integrated into a plasmonic back reflector for thin-film solar cells and have shown up to 75 % diffuse reflectance in the red and near-infrared spectrum [120].

The scattering and absorption in metal NPs are highly influenced by the size and the host medium of NPs, as discussed in Chapter 3. The geometric cross-section of a metal NP is generally smaller than the optical cross-section, which means that smaller NPs absorb more fraction of the sunlight than the bigger ones [123]. On the other hand, an absorber layer in the solar cell has a different absorption range. Therefore, optimization of an ARC with metal NPs on the absorber layer is a primary task to avoid the parasitic absorption loss of the desired wavelength in NPs. The host medium also plays a major role in the optical properties of metal NPs. It has been reported that increasing the refractive index of the host medium broadens the scattering efficiency peak and

shifts the resonance wavelength to a higher value. This is a further way to alleviate the parasitic absorption loss of the desired wavelength in metal NPs [74].

4.3.2 Dielectric Nanoparticles

As discussed in the previous section, metal NPs face absorption loss at the resonance wavelength. However, dielectric NPs do not show this behavior in a narrow band range [81]. So, I performed the simulation study on the hybrid ARC structure in which SiO_2 – NPs are embedded in a SiN ARC on a GaAs substrate layer in place of metal NPs (cf. Figure 4.1). The calculation has been done the same as in the previous section.

Figure 4.11 (c) shows the contour plot of T_w of the hybrid ARC (SiO_2 – NPs (70%) / SiN) in the matrix of AOI and ARC layer thickness. NPs' diameter is equal to the ARC layer thickness in the contour plot. For comparison, I also calculated T_w of SiO_2 thin film ARC (cf. Figure 4.11 (d)). From the previous section, I have summarized the results of SiN thin film ARC and the hybrid ARC (Ag – NPs (70%) / SiN), for comparison in Figure 4.11 (a) & (b), respectively.

SiN ARC shows high transmittance (> 90 %) for the ARC thickness of 60 nm – 80 nm over a wide range of AOI (cf. Figure 4.11 (a)). When the ARC thickness increases more than 80 nm, the transmittance decreases slowly at normal incidence, however with AOI, the transmittance is constant up to 45° AOI and

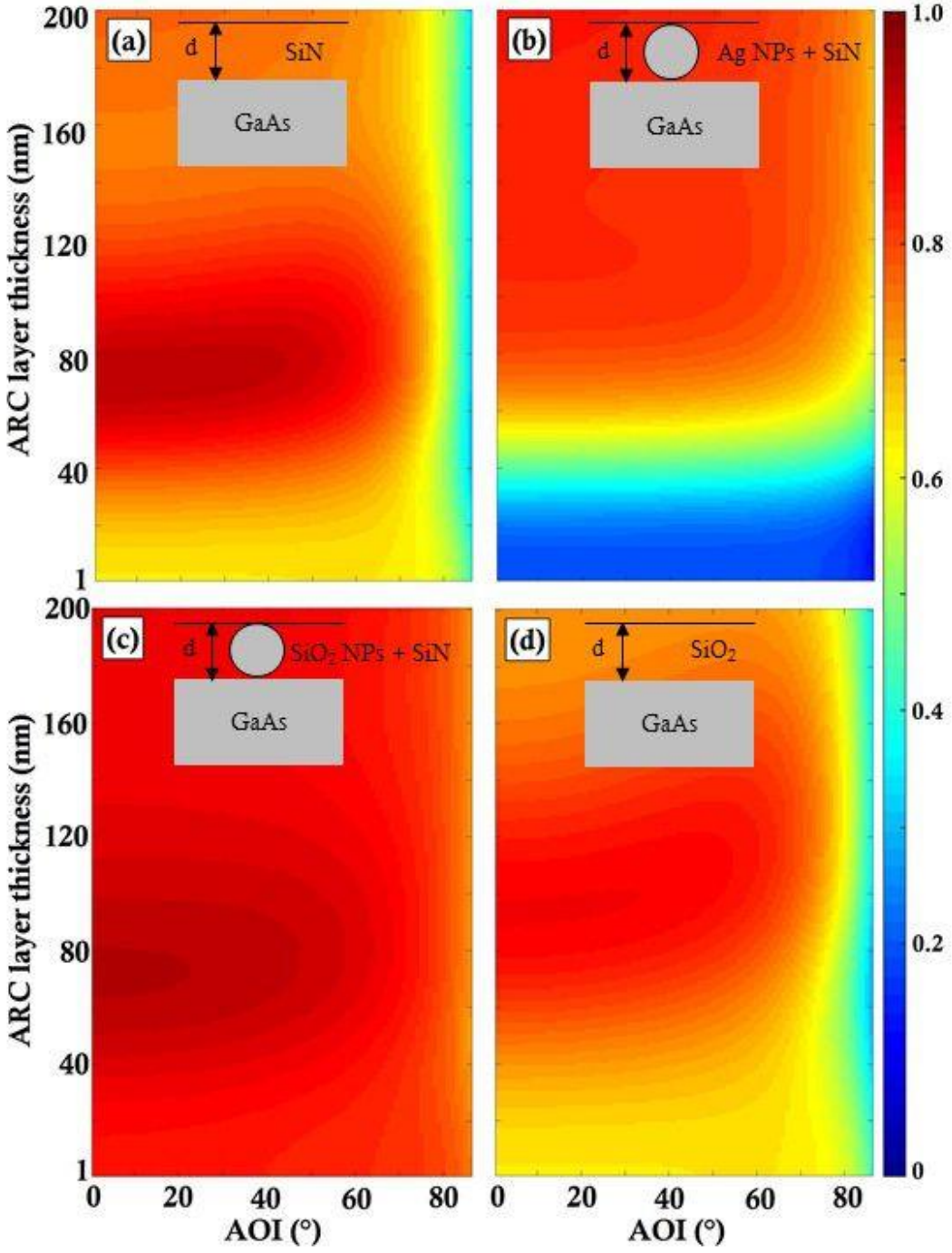

Figure 4.11 Weighted solar power transmittance (T_w) from (a) thin film SiN ARC, (b) hybrid ARC (Ag – NPs (70%) / SiN), (c) hybrid ARC (SiO_2 – NPs (70%) / SiN), and (d) thin film SiO_2 ARC.

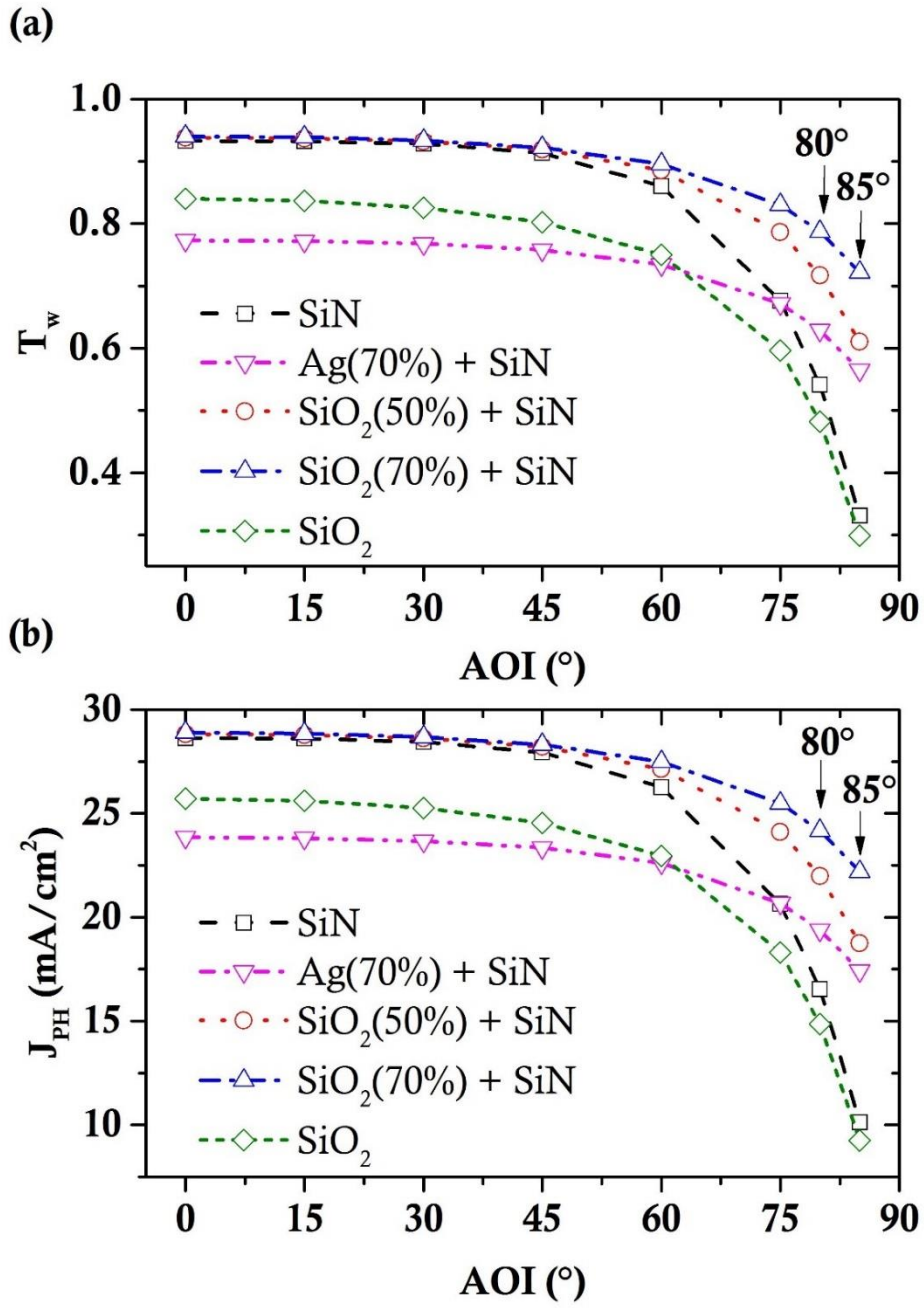

Figure 4.12 (a) Weighted solar power transmittance (T_w), and (b) Photocurrent density (J_{PH}) for 70 nm thick ARC layer. The diameter of NPs is equal to the thickness of the ARC layer.

then decreases slowly. As we know that a fixed solar cell on a house roof, receives sunlight throughout a day at various AOI. Thus, the ARC should perform better at higher AOI. From the metal NPs based hybrid ARCs' simulation, it was concluded that embedding Ag – NPs in the SiN ARC shows better performance at AOI larger than 74°, but not at normal or near-normal AOI.

From Figure 4.11 (a) & (c), it is noticed that the hybrid ARC (SiO_2 – NPs (70%) / SiN) shows the nearly same behavior as the SiN ARC for the ARC layer thickness interval of 60 nm – 80 nm at AOI 0° – 40°. However, the hybrid ARC (SiO_2 – NPs (70%) / SiN) doesn't show much decrease with AOI as the SiN ARC. Hence, the hybrid ARC (SiO_2 – NPs (70%) / SiN) performs better than the SiN ARC, and also, the improvement in T_w is omnidirectional. T_w of SiO_2 thin film ARC decreases at higher AOI (cf. Figure 4.11 (d)). From the principle of single layer ARC, the refractive index of a perfect ARC should follow the following expression: $n_{ARC} = \sqrt{n_{Air} * n_{Substrate}}$ (Section 2.4). If $n_{Substrate} = 3.5$ (for GaAs or Si), then n_{ARC} equals to 1.87. The refractive index of SiN (n_{SiN}) and SiO_2 (n_{SiO_2}) are 2.05 and 1.5 approx., respectively. Hence, n_{SiN} is near to n_{ARC}, but n_{SiO_2} is very far from that. According to the effective medium theory, embedding SiO_2 – NPs in the SiN dielectric matrix brings the effective refractive index nearer to n_{ARC}, therefore I obtained the best ARC performance in the SiO_2 – NPs based hybrid ARC (SiO_2 – NPs (70%) / SiN).

In solar cell applications, the photocurrent density (J_{PH}) is a more commonly discussed device property than the transmittance. So, I calculated J_{PH} with the following formula (cf. Chapter 1)

$$J_{PH} = q * \int_{300\,nm}^{870\,nm} T(\lambda) * PFD(\lambda) * IQE(\lambda)\, d\lambda \qquad (4.9)$$

where $PFD(\lambda)$ and $IQE(\lambda)$ are the photon flux density and the internal quantum efficiency at wavelength λ. The photon flux density is taken from Ref. [17] and shown in Figure 1.2. The operating wavelength is taken from 300 nm to 870 nm because GaAs absorbs the sunlight in this spectrum range. It is assumed in this calculation that all photons which reach the GaAs layer, got absorbed; hence $IQE(\lambda) = 1, for\ all\ \lambda$.

The T_w curve of optimum condition (ARCs with ARC layer thickness of 70 nm) from Figure 4.11 has been summarized in Figure 4.12 (a). I calculated J_{PH} for these optimum ARCs and have shown in Figure 4.12 (b). J_{PH} curves follow the same trend as T_w curves. J_{PH} is almost equal for the SiN ARC structure and the hybrid ARC (SiO_2 – NPs (70%) / SiN) structure till 40° AOI, and after that both curves split. J_{PH} and T_w curves of the hybrid ARC (SiO_2 – NPs (50%) / SiN) are in between of the SiN ARC and the hybrid ARC (SiO_2 – NPs (70%) / SiN). This means that when the surface filling factor goes to zero, the hybrid ARC acts like the SiN ARC (as expected). With the help of Figure 4.12 (b), I calculated the net normalized photocurrent density over the course of a year with respect to the normal incidence by using the following formula at different locations,

$$J_{PH(in\ one\ day)} = \frac{1}{day\ duration\ (in\ minutes)} \int_{sunrise}^{sunset} norm.J_{PH}\ dt(in\ minutes) \quad (4.10)$$

To calculate over the course of a year, average J_{PH} is calculated for each of the days of a year using equation 4.10 and summed over. The summation is divided by the total no. of days in a year. AOI of the sunlight for the solar cell layer changes at every minute of the day and is calculated by the following formula given in Section 2.3. The solar cell absorber layer (GaAs layer in my case) is assumed to face due south in the Northern Hemisphere, and due north in the Southern Hemisphere. The net normalized photocurrent density is summarized in Table 3. I compared the net normalized photocurrent density for two different tilt angles: optimum tilt angle and 45°. The optimum tilt angle is taken from Ref. [124]. Sun position calculation is performed by the method given in Ref. [125] which is based on Meeus formulae [126]. The improvement in current density for the hybrid ARC is clearly noticed at every location. The change in NPs based hybrid ARC is more when the tilt angle is far from the optimum tilt angle.

This study shows that with careful employment of SiO_2 – NPs in the SiN ARC layer improves the ARC property at non – normal AOI while keeping it constant at normal AOI. It follows the trend of previously published articles at higher AOI [93]. In the calculation, I also found that the current density enhancement is more than two times at 85° AOI (cf. Figure 4.12 (b)). Ha et al. reported that 20 mA/cm^2 of photocurrent density at 55° AOI can be achievable

by using only SiO_2 nanospheres of size 700 nm at the front surface [83]. However, I showed 28 mA/cm^2 at the same AOI with the combination of the SiN ARC layer. Sunrise to sunset calculation has also overpassed the previously reported results [17].

Table 3 Normalized Photocurrent density over the course of a year (2020) at different locations (Lat.: latitude; Op.: optimum tilt angle; Hybrid ARC: SiO_2 – NPs (70 %) + SiN; CLZ: Clausthal-Zellerfeld).

ARC type	Munich, Germany (Lat. = 48.13°)		CLZ, Germany (Lat. = 51.807°)		Chennai, India (Lat. = 13.07°)		Perth, Australia (Lat. = -31.93°)		Antofogasta, Chile (Lat. = -23.43°)	
	Op. = 33°	45°	Op. = 36°	45°	Op. = 13°	45°	Op. = 27°	45°	Op. = 22°	45°
SiN ARC	0.85	0.85	0.84	0.84	0.87	0.82	0.87	0.85	0.87	0.84
Hybrid ARC	0.89	0.88	0.89	0.88	0.93	0.88	0.92	0.89	0.92	0.89
% increase	**4.71**	**3.53**	**5.95**	**4.76**	**6.89**	**7.32**	**5.75**	**4.71**	**5.75**	**5.95**

In this study, I focused on SiN as a host medium to present the idea, albeit it's not limited. I have also restricted myself to spherical NPs for less complexity in NP structure and easy to model analytically. However, the shape of NPs plays a major role in the scattering of sunlight to the neighboring substrate. Atwater et al. have published a review article and have shown that the cylindrical shape of NPs scatters more fraction of the incident sunlight in the neighboring substrate than the spherical one [66]. The fraction of dipole radiation also varies with the position of NPs. The sunlight radiation is more in the substrate when NPs are in-contact with the substrate than to be suspended above that [67]. Therefore, NPs embedded in an ARC must be in contact with the substrate.

4.4 CONCLUSIONS

I performed a theoretical study on metal NPs (Ag & Al) based hybrid ARC with a Si-substrate and dielectric NPs (SiO_2) based hybrid ARC with a GaAs substrate over a wide AOI of the AM1.5 solar spectrum. NPs are embedded in a conventional SiN ARC. A point dipole approach with the TMM method was implemented to calculate the total reflectance by NPs based hybrid ARC. I found that embedding metal NPs in SiN ARC enhance the antireflection property of conventional SiN ARC at non-normal AOI. At normal incidence, SiN ARC still performs the best. Electric field distribution patterns of radiation by a metal NP in the substrate support improvements in the antireflection performance. I also obtained weighted solar power transmittance curves which show that Ag – NPs in SiN ARC performs better than SiN ARC over 74° AOI and Al – NPs in SiN ARC performs better over 78° AOI but both hybrid ARC performs less efficient at normal and near-normal AOI. On the contrary, the dielectric SiO_2 – NPs based hybrid ARC improves the weighted solar power transmittance at higher AOI while keeping it constant (insignificant change) at normal incidence. The improvements are also visible in the photocurrent density in the GaAs layer at higher AOI. It is more than two times enhancement at 85° AOI. Sunrise to sunset calculation of the normalized photocurrent density has also shown improvement in the dielectric SiO_2 – NPs hybrid ARC case.

5

SUMMARY

In summary, I presented a theoretical framework on the light photon management in Si and GaAs solar cells with hybrid ARCs using metal/dielectric NPs embedded in a traditional single-layer SiN thin film ARC.

The theoretical study on metal NPs (Ag, Au, Cu, and Al) with an absorber layer (n-GaAs) over a wide AOI of the AM1.5 solar spectrum revealed that Al – NPs gives the best performance among Ag –, Au –, Cu –, and Al – NPs at normal incidence with a 38.28 % increase in the reference power transfer value. Wide-angle improvement was also determined in this case. In this study, only the specular transmission of the incident sunlight was considered. Whereas an NP behaves like a dipole scatterer and causes a radiation pattern of the transmitted sunlight. To remove this shortcoming, I modified the model with a

dipole approach and designed NPs based ARCs (hybrid ARCs). I found out that embedding metal NPs in SiN ARC enhance the antireflection property of the SiN thin film ARC at non-normal AOI. However, SiN ARC still performs the best at normal incidence. I calculated weighted solar power transmittance curves which showed that Ag – NPs in SiN performs better than SiN over 74° AOI whereas Al-NPs in SiN performs better over 78° AOI. The weak performance of ARC at normal and near-normal AOI is related to the parasitic absorption in the metal NPs. Therefore, I performed the same analysis on dielectric SiO_2 – NPs because dielectric NPs don't show absorption in a narrow band spectrum. The analytical study on dielectric SiO_2 – NPs based hybrid ARC affirmed the enhancement in weighted solar power transmittance at higher AOI while keeping it constant (insignificant change) at normal AOI. I also performed the photocurrent density calculation and obtained more than two times enhancement in SiO_2 – NPs based ARC case at 85° AOI. Sunrise to sunset calculation of the normalized photocurrent density has also shown improvement in the SiO_2 – NPs based ARC case. Overall, the hybrid ARC (SiO_2 – NPs (70%) / SiN) improves the antireflection property and is recommended to use as an ARC in solar cells.

In the future, solar cells integrated into buildings, cars, etc. might become more important. In these cases, solar panels are typically not oriented toward the sun and they have to deal with AOI far from the normal incidence. Conventional thin-film ARC such as SiN ARC is generally optimized for a certain AOI (typically close to the normal incidence). Therefore, the hybrid ARC gives a route to lessen the unwanted reflection at higher AOI and increase the overall efficiency of a solar cell.

This study can also be used to guide future experimental design. Optimizations of experimental work such as the optimization of NPs' size, the optimization of nanostructures, etc. might lead to even better performance than that predicted by this simulation study [66].

6

OUTLOOK

6.1 QUANTUM – WELL (QW) AND WAVEGUIDE SOLAR CELLS

GaAs has a direct bandgap and a large absorption coefficient ($1x10^4$ /cm) in the visible range. These two major physical properties make it a promising material for high conversion efficiency solar cells for space applications or terrestrial scenarios. One of the major issues in achieving high efficiency is the recombination (non-radiative and radiative) of photon generated charge carriers inside the device structure (as discussed in Chapter 1). The non-radiative recombination consists of Auger recombination and SRH recombination. Since, in GaAs based solar cells, the Auger recombination can be easily minimized by the optimization of doping concentration and the SRH recombination is almost negligible in pure GaAs [127]. So, the efficiency of

these devices is mostly dictated by radiative recombination. Better photon management in the device designing is suggested to prevent the radiative recombination loss [24], [128] i.e. the usage of a highly reflective contact mirror at the rear side is proposed to minimize the effect of radiative recombination by recycling radiatively recombined electron-hole pairs and unabsorbed photons. The recycling mechanism significantly improved the efficiency of the solar cell resulting in a record efficiency of 28.8 % for a GaAs single-junction solar cell [128].

The efficiency of a single junction solar cell is determined by a single bandgap. Striving for highly efficient solar cells, Barnham et al. reported a multi-bandgap solar cell in which the absorption range was spanned from visible to infra-red [11]. It was reported that the incorporation of GaAs quantum well (QW) layers in the intrinsic region (i-region) of an $Al_XGa_{1-X}As$ p-i-n solar cell and $In_XGa_{1-X}As$ QW layers in the i-region of a GaAs p-i-n solar cell allow the absorption of low energy photons, increasing the short-circuit current density (J_{SC}), although it decreases the V_{OC} from the V_{OC} of baseline p-i-n solar cell. The decrease in V_{OC} is due to the increased space charge recombination trapped in QW layers [129]. The reduction of charge carrier recombination in a multi-bandgap solar cell is a big challenge. Welser et al. [130] suggested that the unwanted space-charge recombination can be minimized by incorporating a wide band gap material within the heterojunction depletion region and/or incorporating a step-graded QW layer.

6.1.1 Preliminary Results – one QW

I simulated a QW solar cell with one QW of $In_{0.2}Ga_{0.8}As$ of thickness 13 nm sandwiched between two unintentionally doped GaAs (i-GaAs) layers with a thickness of 460 nm and 470 nm. A 150 nm p-type ($p = 1 \times 10^{18}$ cm^{-3}) GaAs and a 230 nm n-type ($n = 2 \times 10^{17}$ cm^{-3}) GaAs layer are on both sides of i-GaAs. A contact layer of Silver (Ag) with a thickness of 100 nm is used on the backside of the device for a better back reflection. For the p-i-n solar cell, the total thickness of the i-GaAs layer is 943 nm.

The designed QW of $In_{0.2}Ga_{0.8}As$ material in i-layer have two discrete energy levels in the conduction band (CB), first at 1050 nm and second at 950 nm, calculated by the following formula [131]:

$$E_n = \frac{n^2\pi^2\hbar^2}{2ma^2} \tag{6.1}$$

where n is the energy level in the CB of QW, m is the effective mass of an electron in the QW layer, and a is the width of the QW layer. The band gap (E_g) of $In_{0.2}Ga_{0.8}As$ material has been calculated by using the following expression with doping concentration x in $Ga_XIn_{1-X}As$ compound semiconductor [132]:

$$E_g = (0.36 + 0.63x + 0.43x^2)\ eV \tag{6.2}$$

Hence, a photon absorption is only possible for the aforementioned two energy levels. The absorption of a photon inside any layer is directly proportional to the electric field intensity distribution in the layer [133]. Hence, I calculated the

normalized electric field intensity, $|\mathrm{E}|^2$, distribution (cf. Figure 6.1) for both wavelengths by using the following equation obtained from the TMM method. From Section 3.2.2, the electric field in j^{th} layer is given by

$$E_j(x) = E_j^+(x) + E_j^-(x)$$
$$= [t_j^+ . e^{i.(2\pi/\lambda).n_j.\cos(\theta_j).x} + t_j^- . e^{-i.(2\pi/\lambda).n_j.\cos(\theta_j).x}]E_0^+ \quad (6.3)$$

where $t_j^+ = \frac{t_{0j}}{1+r_{0j}.r_{js}.e^{2i.(2\pi/\lambda).d_j.n_j.\cos(\theta_j)}}$, $t_j^- = t_j^+ . r_{js} . e^{2i.(2\pi/\lambda).d_j.n_j.\cos(\theta_j)}$

and the transmission and the reflection coefficients for j^{th} layer can be obtained in terms of matrix elements as

$$t_{0j} = \frac{1}{M_{11}^{0j}}, r_{0j} = \frac{M_{21}^{0j}}{M_{11}^{0j}}, where\ M_{0j} = M_{01}.P_1.M_{12}.P_2 \dots \dots \dots \dots P_{j-1}.M_{j-1} \quad (6.4)$$

$$t_{js} = \frac{1}{M_{11}^{js}}, r_{js} = \frac{M_{21}^{js}}{M_{11}^{js}}, where\ M_{js}$$
$$= M_{j(j+1)}.P_{j+1}.M_{(j+1)(j+2)}.P_{j+2} \dots \dots \dots \dots \dots P_m.M_{ms} \quad (6.5)$$

t_{0j}, r_{0j}, t_{js} and r_{js} are the partial transmission and reflection coefficients (from 0^{th} to j^{th} and from j^{th} to substrate) for the j^{th} layer, respectively.

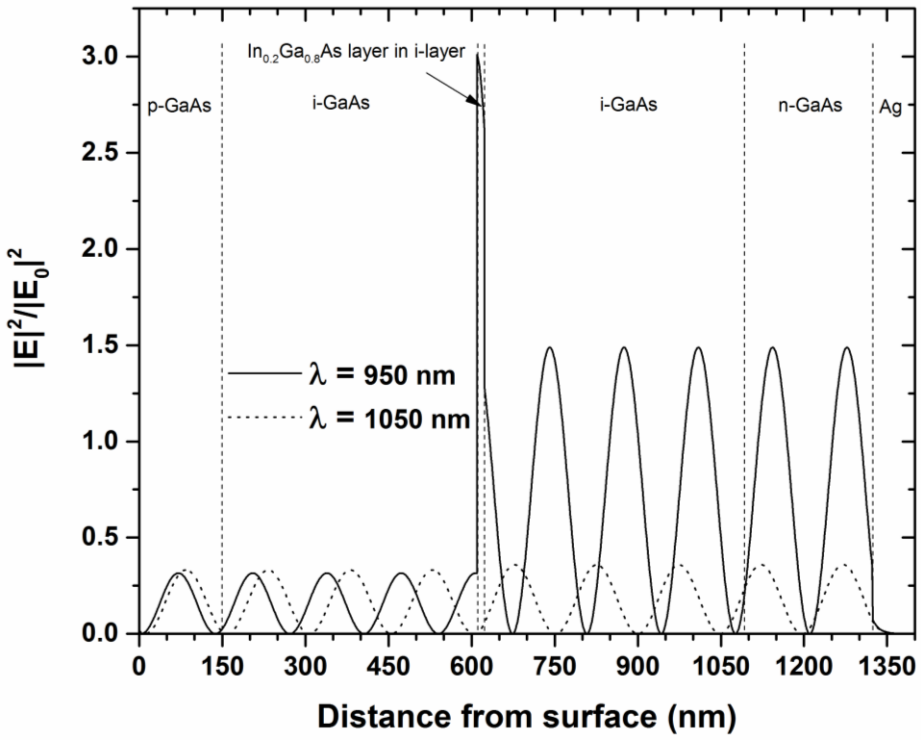

Figure 6.1 Electric field intensity inside a QW solar cell.

The barrier layers are very thick in the simulated device so that the escape of minority charge carriers via tunneling is almost negligible and is only possible via thermionic emission. This is a reason that I have optimized the device for the light of wavelength 950 nm. The maxima and minima in Figure 6.1 show that there is an existence of strong Fabry-Perot resonances and waveguide mode coupling effects inside the device. The multiple reflection and interference enhance the field intensity drastically in the QW layer. The electric field intensity distribution at the interfaces like GaAs/$In_{0.2}Ga_{0.8}As$ and GaAs/Ag become discontinuous which is because the complex refractive index changes at the interface. For the light of wavelength 950 nm, the electric field intensity inside the QW layer is higher than the rest of the device which

confirms that most of the light of this wavelength is concentrated in the QW layer which makes sure of high absorption in this layer. On the other hand, the electric field intensity for the wavelength of 1050 nm distribution inside the QW layer is nearly zero. For the simulated device, the absorption of light photons with a wavelength of 1050 nm is also undesirable.

6.1.2 Preliminary Results – multiple QWs

I took an optimum GaAs p-n solar cell structure from a published research article [128]. Since multiple QWs solar cells are p-i-n solar cells with QWs incorporated in the i-region. Therefore, using 1D Poisson solver, a GaAs p-i-n SC is designed from the p-n GaAs solar cell. In the i-region of p-i-n GaAs solar cell, three $In_XGa_{1-X}As$ QW layers are integrated each with a thickness of 13 nm separated by 10 nm GaAs barrier layers with 470.5 nm thick undoped GaAs immediately above and below the multiple QW region. The thicknesses of p-type GaAs ($p = 1 \times 10^{18}$ cm^{-3}) and n-type GaAs ($n = 2 \times 10^{17}$ cm^{-3}) layer are 150 nm and 230 nm, respectively (cf. Figure 6.2).

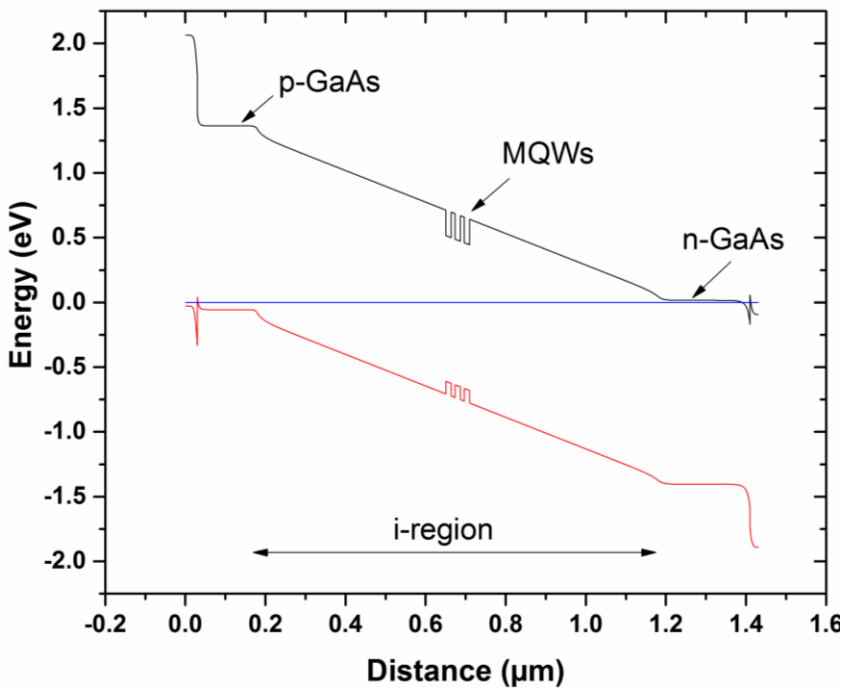

Figure 6.2 Simulated energy band diagram of multiple QW solar cell.

The multiple QWs solar cell has been simulated using the Silvaco TCAD simulation tool. Silvaco TCAD is a commercial device simulation tool based on the drift-diffusion model using the finite element method (FEM) for semiconductor devices. The flow diagram of the simulation model for a solar cell in Silvaco TCAD is shown in Figure 6.3. The structure of the device is generated in the structure editor and meshed for FEM simulation. Some material parameters are already in the TCAD database, which is not, they are provided manually from literature. Different models are used to execute the solar cell characteristics. In my case, carrier mobility models, carrier statistics model, and recombination model are used for multiple QWs solar cell simulation. The Poisson equation, drift-diffusion equation, and Schrödinger equation are solved for the I-V characteristics and EQE simulation. The TMM method is applied for the optical generation profile in the device.

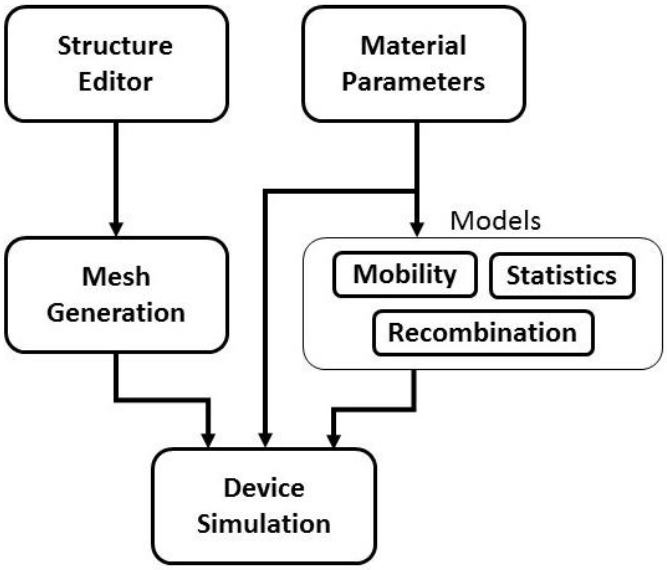

Figure 6.3 Flow diagram of Silvaco TCAD simulation model.

Table 4 Photovoltaic characteristics of the GaAs p-n solar cell devices under AM1.5 illumination (CE: conversion efficiency).

Device Structure	J_{SC} (mA/cm^2)	V_{OC} (V)	FF	CE (%)
GaAs p-n solar cell (ADEPT 2.0)	29.49	1.107	0.867	28.35
GaAs p-n solar cell (Silvaco TCAD)	29.87	1.071	0.887	28.39

Using Silvaco TCAD, I simulated EQE and the I-V characteristics of the device structure with various compositions of $In_XGa_{1-X}As$ QW layers (cf. Figure 6.4). To verify the accuracy of the Silvaco TCAD simulation tool, I first applied it to the

work presented in Ref. [128] in which a GaAs p-n solar cell device has been designed and calculated the photovoltaic characteristics, which is presented and

compared to my simulated results in Table 4. The comparison proves the accuracy of the Silvaco TCAD simulation model and advocates use for simulation.

From Figure 6.4, it has been clear that incorporation of QWs in the i-region enhances the absorption range from visible to the infra-red region (cf. green rectangle in Figure 6.4 (b)) and hence the photogenerated current density (cf. current axis in Figure 6.4 (a)). However, due to an increase in the radiative recombination in the QW layer, V_{OC} of the device decreases which causes an overall decrease in the efficiency of multiple QWs solar cell from the baseline (p-i-n) solar cell (cf. inset in Figure 6.4 (a)).

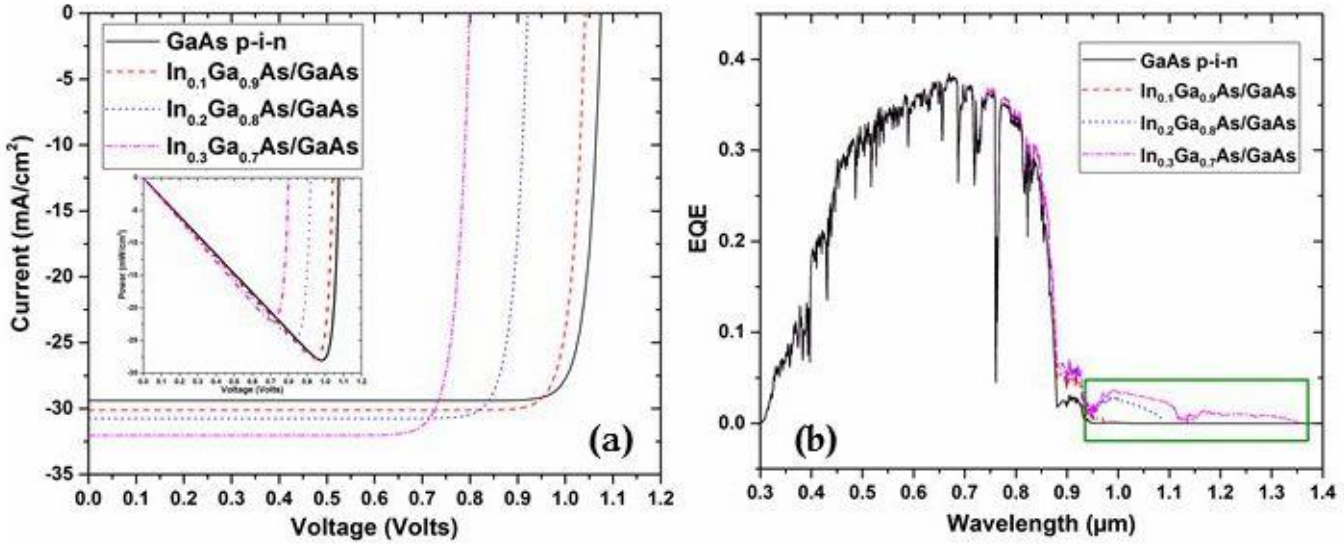

Figure 6.4 Simulated (a) I-V characteristics, and (b) EQE of $In_xGa_{1-x}As/GaAs$ multiple QWs solar cells.

Optical scattering via NPs and efficient coupling of the scattered sunlight in a waveguide mode of QWs can be used to improve the trapping of the sunlight. This will further increase the absorption in the solar cell by increasing the

optical path length through the solar cell absorber layer without changing the electronic path of photon generated charge carriers [133]–[136]. Li et al. [133] have demonstrated this phenomenon in $In_{0.3}Ga_{0.7}As/GaAs$ based quantum well solar cell and reported 2.9 % enhancement in EQE per QW for longer wavelength, experimentally. The hybrid ARC designs can be used in QW/waveguide solar cells which will not only promote the ARC property but also the waveguide mode coupling.

REFERENCES

[1] B. Singh, M. M. Shabat, and D. M. Schaadt, "Analytical modeling of power transfer via metallic nanoparticles in a solar cell absorber," *J. Quant. Spectrosc. Radiat. Transf.*, vol. 243, p. 106807, 2020.

[2] B. Singh, M. M. Shabat, and D. M. Schaadt, "Wide angle antireflection in metal nanoparticles embedded in a dielectric matrix for plasmonic solar cells," *Prog. Photovoltaics Res. Appl.*, vol. 28, pp. 682–690, 2020.

[3] B. Singh, M. M. Shabat, and D. M. Schaadt, "Silver nanoparticle-based anti-reflection coating for solar cells," in *SPIE Photonics for Solar Energy Systems VIII*, 2020, no. April, pp. 1–6.

[4] B. Singh, M. M. Shabat, and D. M. Schaadt, "Large photocurrent density enhancement assisted by non-absorbing spherical dielectric nanoparticles in a GaAs layer," *Sci. Rep.*,10:17107, 2020.

[5] M. Tsoskounoglou, G. Ayerides, and E. Tritopoulou, "The end of cheap oil: Current status and prospects," *Energy Policy*, vol. 36, no. 10, pp. 3797–3806, 2008.

[6] S. M. Sze and K. K. Ng, *Physics of Semiconductor Devices*, Third Edit. John Wiley & Sons, Inc., 2007.

[7] C. Battaglia, A. Cuevas, and S. De Wolf, "High-efficiency crystalline silicon solar cells: Status and perspectives," *Energy Environ. Sci.*, vol. 9, pp. 1552–1576, 2016.

[8] G. Lush and M. Lundstrom, "Thin film approaches for high-efficiency III-V cells," *Sol. Cells*, vol. 30, pp. 337–344, 1991.

[9] J. Ramanujam and U. P. Singh, "Copper indium gallium selenide based solar cells - A review," *Energy Environ. Sci.*, vol. 10, pp. 1306–1319, 2017.

[10] R. R. King *et al.*, "40% efficient metamorphic GaInP/GaInAs/Ge multijunction solar cells," *Appl. Phys. Lett.*, vol. 90, p. 183516, 2007.

[11] K. W. J. Barnham and G. Duggan, "A new approach to high-efficiency multi-band-gap solar cells," *J. Appl. Phys.*, vol. 67, p. 3490, 1990.

[12] N. G. Anderson, "Ideal theory of quantum well solar cells," *J. Appl. Phys.*, vol. 78, pp. 1850–1861, 1995.

[13] R. E. Welser, A. K. Sood, C. Park, J. S. Lewis, D. Mto, and N. R. Street, "Development of III-V Quantum Well and Quantum Dot Solar Cells," *Int. J. Eng. Res. Technol.*, vol. 9, no. 1, pp. 29–44, 2016.

[14] D. M. Schaadt, B. Feng, and E. T. Yu, "Enhanced semiconductor optical

absorption via surface plasmon excitation in metal nanoparticles," *Appl. Phys. Lett.*, vol. 86, p. 063106, 2005.

[15] M. A. Green, *Solar cells - Operating Principles, Technology and System Application*. Prentice-Hall, Inc., 1998.

[16] "Ideality Factor," 2020. [Online]. Available: https://www.pveducation.org/pvcdrom/solar-cell-operation/ideality-factor. [Accessed: 10-Sep-2020].

[17] S. A. Boden and D. M. Bagnall, "Sunrise to Sunset Optimization of Thin Film Antireflective Coatings for Encapsulated , Planar Silicon Solar Cells," *Prog. Photovoltaics Res. Appl.*, vol. 17, pp. 241–252, 2009.

[18] W. Shockley and H. J. Queisser, "Detailed Balance Limit of Efficiency of p-n Junction Solar Cells," *J. Appl. Phys.*, vol. 32, no. 3, pp. 510–519, 1961.

[19] J. Meier, R. Flückiger, H. Keppner, and A. Shah, "Complete microcrystalline pin solar cell - Crystalline or amorphous cell behavior ?," *Appl. Phys. Lett.*, vol. 65, pp. 860–862, 1994.

[20] N. J. Ekins-Daukes *et al.*, "Strain-balanced GaAsP/InGaAs quantum well solar cells," *Appl. Phys. Lett.*, vol. 75, pp. 4195–4197, 1999.

[21] R. E. Welser *et al.*, "High-voltage quantum well waveguide solar cells," in *SPIE Next Generation (Nano) Photonic and Cell Technologies for Solar Energy Conversion II*, 2011, vol. 8111.

[22] S. Rühle, S. Greenwald, E. Koren, and A. Zaban, "Optical waveguide enhanced photovoltaics," *Opt. Express*, vol. 16, no. 26, 2007.

[23] D. Bouhafs, A. Moussi, A. Chikouche, and J. M. Ruiz, "Design and simulation of antireflection coating for optoelectronic devices: Application to silicon solar cells," *Sol. Energy Mater. Sol. Cells*, vol. 52, no. 1, pp. 79–93, 1998.

[24] O. D. Miller, E. Yablonovitch, and S. R. Kurtz, "Strong internal and external luminescence as solar cells approach the Shockley-Queisser limit," *IEEE J. Photovoltaics*, vol. 2, no. 3, pp. 303–311, 2012.

[25] D. Buie, M. J. McCann, K. J. Weber, and C. J. Dey, "Full day simulations of anti-reflection coatings for flat plate silicon photovoltaics," *Sol. Energy Mater. Sol. Cells*, vol. 81, no. 1, pp. 13–24, 2004.

[26] D. B. Bushnell *et al.*, "Effect of well number on the performance of quantum-well solar cells," *J. Appl. Phys.*, vol. 97, pp. 124904–124908, 2005.

[27] M. K. Hedayati and M. Elbahri, "Antireflective coatings: Conventional stacking layers and ultrathin plasmonic metasurfaces, a mini-review," *Materials (Basel).*, vol. 9, p. 497, 2016.

[28] P. Yeh, *Optical waves in layered media*. John Wiley & Sons, Inc., 2005.

[29] S. A. Kalogirou, *Solar Energy Engineering: Processes and Systems*. Elsevier Inc., 2009.

[30] L. Rayleigh, "On Reflection of Vibrations at the Confines of two Media between which the Transition is Gradual," in *Proceedings of the London Mathematical Society*, 1880, pp. 51–56.

[31] J. Strong, "On a Method of Decreasing the Reflection from Nonmetallic Substances," *J. Opt. Soc. Am.*, vol. 26, no. 1, p. 73, 1936.

[32] H. K. Raut, V. A. Ganesh, A. S. Nair, and S. Ramakrishna, "Anti-reflective coatings: A critical, in-depth review," *Energy Environ. Sci.*, vol. 4, pp. 3779–3804, 2011.

[33] J. Sun, X. Cui, C. Zhang, C. Zhang, R. Ding, and Y. Xu, "A broadband antireflective coating based on a double-layer system containing mesoporous silica and nanoporous silica," *J. Mater. Chem. C*, vol. 3, no. 27, pp. 7187–7194, 2015.

[34] H. A. MacLeod, *Thin-Film Optical Filters*, Third Edit. Institute of Physics Publishing, 2001.

[35] K. Han and C. Chang, "Numerical Modeling of Sub-Wavelength Anti-Reflective Structures for Solar Module Applications," *Nanomaterials*, vol. 4, pp. 87–128, 2014.

[36] A. W. Smith and A. Rohatgi, "A new texturing geometry for producing high efficiency solar cells with no antireflection coatings," *Sol. Energy Mater. Sol. Cells*, vol. 29, no. 1, pp. 51–65, 1993.

[37] J. Zhao, A. Wang, M. A. Green, and F. Ferrazza, "19.8% efficient 'honeycomb' textured multicrystalline and 24.4% monocrystalline silicon solar cells," *Appl. Phys. Lett.*, vol. 73, no. 14, pp. 1991–1993, 1998.

[38] P. Papet *et al.*, "Pyramidal texturing of silicon solar cell with TMAH chemical anisotropic etching," *Sol. Energy Mater. Sol. Cells*, vol. 90, no. 15, pp. 2319–2328, 2006.

[39] A. J. Fresnel, "Mémoire sur la loi des modifications que la réflexion imprime à la lumière polarisée," *l'Academie des Sci.*, vol. T. XI., pp. 393–433, 1823.

[40] H. R. Philipp, "Optical Properties of Silicon Nitride," *J. Electrochem. Soc.*, vol. 120, no. 2, p. 295, 1973.

[41] K. Marszałek, P. Winkowski, and J. Jaglarz, "Optical properties of the Al_2O_3/SiO_2 and $Al_2O_3/HfO_2/SiO_2$ antireflective coatings," *Mater. Sci. Pol.*, vol. 32, no. 1, pp. 80–87, 2014.

[42] M. M. Shabat, D. M. El-Amassi, and D. M. Schaadt, "Design and analysis of multilayer waveguides containing nanoparticles for solar cells," *Sol. Energy*, vol. 137, pp. 409–412, 2016.

[43] M. Mazur, D. Wojcieszak, J. Domaradzki, D. Kaczmarek, S. Song, and F. Placido, "TiO_2/SiO_2 multilayer as an antireflective and protective coating deposited by microwave assisted magnetron sputtering," *Opto-Electronics Rev.*, vol. 22, no. 2, pp. 77–85, 2010.

[44] J. Szczyrbowski, G. Bräuer, G. Teschner, and A. Zmelty, "Antireflective coatings on large scale substrates produced by reactive twin-magnetron sputtering," *J. Non. Cryst. Solids*, vol. 218, pp. 25–29, 1997.

[45] D. Glöß *et al.*, "Multifunctional high-reflective and antireflective layer systems with easy-to-clean properties," *Thin Solid Films*, vol. 516, no. 14, pp. 4487–4489, 2008.

[46] X. Yan *et al.*, "Enhanced omnidirectional photovoltaic performance of solar cells using multiple-discrete-layer tailored- and low-refractive index anti-reflection coatings," *Adv. Funct. Mater.*, vol. 23, no. 5, pp. 583–590, 2013.

[47] S. Y. Lien, D. S. Wuu, W. C. Yeh, and J. C. Liu, "Tri-layer antireflection coatings (SiO_2/SiO_2-TiO_2/TiO_2) for silicon solar cells using a sol-gel technique," *Sol. Energy Mater. Sol. Cells*, vol. 90, no. 16, pp. 2710–2719, 2006.

[48] C. C. Chen, D. J. Lin, T. M. Don, F. H. Huang, and L. P. Cheng, "Preparation of organic-inorganic nano-composites for antireflection coatings," *J. Non. Cryst. Solids*, vol. 354, no. 32, pp. 3828–3835, 2008.

[49] X. Wang and J. Shen, "Sol-gel derived durable antireflective coating for solar glass," *J. Sol-Gel Sci. Technol.*, vol. 53, no. 2, pp. 322–327, 2010.

[50] J. Li *et al.*, "Design, preparation, and durability of TiO_2/SiO_2 and ZrO_2/SiO_2 double-layer antireflective coatings in crystalline silicon solar modules," *Sol. Energy*, vol. 89, pp. 134–142, 2013.

[51] L. Ye *et al.*, "Sol-gel preparation of $SiO_2/TiO_2/SiO_2$-TiO_2 broadband antireflective coating for solar cell cover glass," *Sol. Energy Mater. Sol. Cells*, vol. 111, pp. 160–164, 2013.

[52] Ö. Kesmez, H. Erdem Çamurlu, E. Burunkaya, and E. Arpaç, "Sol-gel preparation and characterization of anti-reflective and self-cleaning SiO_2-TiO_2 double-layer nanometric films," *Sol. Energy Mater. Sol. Cells*, vol. 93, no. 10, pp. 1833–1839, 2009.

[53] B. S. Richards, "Single-material TiO_2 double-layer antireflection coatings," *Sol. Energy Mater. Sol. Cells*, vol. 79, no. 3, pp. 369–390, 2003.

[54] J. Zhao, A. Wang, P. Altermatt, and M. A. Green, "Twenty-four percent

efficient silicon solar cells with double layer antireflection coatings and reduced resistance loss," *Appl. Phys. Lett.*, vol. 66, no. June, p. 3636, 1995.

[55] Z. Chen, P. Sana, J. Salami, and A. Rohatgi, "A Novel and Effective PECVD SiO_2/SiN Antireflection Coating for Si Solar Cells," *IEEE Trans. Electron Devices*, vol. 40, no. 6, pp. 1161–1165, 1993.

[56] S. Winderbaum, F. Yun, and O. Reinhold, "Application of plasma enhanced chemical vapor deposition silicon nitride as a double layer antireflection coating and passivation layer for polysilicon solar cells," *J. Vac. Sci. Technol. A Vacuum, Surfaces, Film.*, vol. 15, no. 3, pp. 1020–1025, 1997.

[57] S. K. Dhungel, J. Yoo, K. Kim, S. Jung, S. Ghosh, and J. Yi, "Double-layer antireflection coating of MgF_2/SiNx for crystalline silicon solar cells," *J. Korean Phys. Soc.*, vol. 49, no. 3, pp. 885–889, 2006.

[58] B. S. Chiou and J. H. Tsai, "Antireflective coating for ITO films deposited on glass substrate," *J. Mater. Sci. Mater. Electron.*, vol. 10, no. 7, pp. 491–495, 1999.

[59] S. A. Boden and D. M. Bagnall, "Optimization of moth-eye antireflection schemes for silicon solar cells," *Prog. Photovoltaics Res. Appl.*, vol. 18, pp. 195–203, 2010.

[60] L. Rayleigh, "On the scattering of light by small particles," *Philos. Mag. J. Sci.*, vol. 41, no. 275, pp. 447–454, 1871.

[61] X. Fan, W. Zheng, and D. J. Singh, "Light scattering and surface plasmons on small spherical particles," *Light Sci. Appl.*, vol. 3, no. March, pp. 1–14, 2014.

[62] J. D. Jackson, *Classical Electrodynamics*, Third Edit. John Wiley & Sons, Inc., 1998.

[63] M. Kerker, *The scattering of light and other electromagnetic radiation*. Academic Press.

[64] G. Mie, "Beiträge zur Optik trüber Medien, speziell kolloidaler Metallösungem," *Ann. Phys.*, vol. 25, no. 3, 1908.

[65] C. F. Bohren and J. Wiley, *Absorption and Scattering of Light by Small Particles*. John Wiley & Sons, Inc., 1983.

[66] H. A. Atwater and A. Polman, "Plasmonics for improved photovoltaic devices," *Nat. Mater.*, vol. 9, pp. 205–213, 2010.

[67] K. R. Catchpole and A. Polman, "Plasmonic solar cells," *Opt. Express*, vol. 16, no. 26, pp. 21793–21800, 2008.

[68] S. Pillai and M. A. Green, "Plasmonics for photovoltaic applications," *Sol. Energy Mater. Sol. Cells*, vol. 94, pp. 1481–1486, 2010.

[69] L. Hong *et al.*, "Design principles for plasmonic thin film GaAs solar cells with high absorption enhancement," *J. Appl. Phys.*, vol. 112, no. September, p. 054326, 2012.

[70] D. Derkacs, S. H. Lim, P. Matheu, W. Mar, and E. T. Yu, "Improved performance of amorphous silicon solar cells via scattering from surface plasmon polaritons in nearby metallic nanoparticles," *Appl. Phys. Lett.*, vol. 89, p. 093103, 2006.

[71] Z. Ouyang, X. Zhao, S. Varlamov, Y. Tao, J. Wong, and S. Pillai, "Nanoparticle - enhanced light trapping in thin - film silicon solar cells," *Prog. Photovoltaics Res. Appl.*, vol. 19, pp. 917–926, 2011.

[72] K. Nakayama, K. Tanabe, and H. A. Atwater, "Plasmonic nanoparticle enhanced light absorption in GaAs solar cells," *Appl. Phys. Lett.*, vol. 93, p. 121904, 2008.

[73] X. H. Li, P. C. Li, D. Z. Hu, D. M. Schaadt, and E. T. Yu, "Light trapping in thin-film solar cells via scattering by nanostructured antireflection coatings," *J. Appl. Phys.*, vol. 114, p. 044310, 2013.

[74] T. L. Temple and D. M. Bagnall, "Broadband scattering of the solar spectrum by spherical metal nanoparticles," *Prog. Photovoltaics Res. Appl.*, vol. 21, pp. 600–611, 2013.

[75] J. R. Cole and N. J. Halas, "Optimized plasmonic nanoparticle distributions for solar spectrum harvesting," *Appl. Phys. Lett.*, vol. 89, p. 153120, 2006.

[76] P. B. Johnson and R. W. Christy, "Optical Constants of the Noble Metals," *Phys. Rev. B*, vol. 6, no. 12, p. 4370, 1972.

[77] M. D. Mcmahon, R. Lopez, H. M. Meyer, L. C. Feldman, and R. F. Haglund, "Rapid tarnishing of silver nanoparticles in ambient laboratory air," *Appl. Phys. B Lasers Opt.*, vol. 80, no. 7, pp. 915–921, 2005.

[78] M. L. Brongersma, Y. Cui, and S. Fan, "Light management for photovoltaics using high-index nanostructures," *Nat. Mater.*, vol. 13, no. 5, pp. 451–460, 2014.

[79] P. Spinelli and A. Polman, "Light trapping in thin crystalline Si solar cells using surface mie scatterers," *IEEE J. Photovoltaics*, vol. 4, no. 2, pp. 554–559, 2014.

[80] A. E. Krasnok, A. E. Miroshnichenko, P. A. Belov, and Y. S. Kivshar, "All-dielectric optical nanoantennas," *Opt. Express*, vol. 20, no. 18, pp. 20599–20604, 2012.

[81] Y. A. Akimov, W. S. Koh, S. Y. Sian, and S. Ren, "Nanoparticle-enhanced thin film solar cells: Metallic or dielectric nanoparticles?," *Appl. Phys. Lett.*, vol. 96, p. 073111, 2010.

[82] P. Matheu, S. H. Lim, D. Derkacs, C. McPheeters, and E. T. Yu, "Metal and dielectric nanoparticle scattering for improved optical absorption in photovoltaic devices," *Appl. Phys. Lett.*, vol. 93, p. 113108, 2008.

[83] D. Ha, Y. Yoon, and N. B. Zhitenev, "Nanoscale imaging of photocurrent enhancement by resonator array photovoltaic coatings," *Nanotechnology*, vol. 29, p. 145401, 2018.

[84] D. Ha, C. Gong, M. S. Leite, and J. N. Munday, "Demonstration of Resonance Coupling in Scalable Dielectric Microresonator Coatings for Photovoltaics," *ACS Appl. Mater. Interfaces*, vol. 8, pp. 24536–24542, 2016.

[85] D. Wan, H. L. Chen, T. C. Tseng, C. Y. Fang, Y. S. Lai, and F. Y. Yeh, "Antireflective nanoparticle arrays enhance the efficiency of silicon solar cells," *Adv. Funct. Mater.*, vol. 20, pp. 3064–3075, 2010.

[86] D. Ha and N. B. Zhitenev, "Improving Dielectric Nanoresonator Array Coatings for Solar Cells," *Part. Part. Syst. Charact.*, vol. 35, p. 1800131, 2018.

[87] Y. Tong *et al.*, "Photonic enhanced thin-film solar cells with conformal nanostructure," *Sol. Energy*, vol. 173, pp. 504–510, 2018.

[88] J. R. Nagel and M. A. Scarpulla, "Enhanced absorption in optically thin solar cells by scattering from embedded dielectric nanoparticles," *Opt. Express*, vol. 18, no. S2, 2010.

[89] Y.-M. Yeh, Y.-S. Wang, and J.-H. Li, "Enhancement of the optical transmission by mixing the metallic and dielectric nanoparticles atop the silicon substrate," *Opt. Express*, vol. 19, no. S2, p. A80, 2011.

[90] K. V. Baryshnikova, M. I. Petrov, V. E. Babicheva, and P. A. Belov, "Plasmonic and silicon spherical nanoparticle antireflective coatings," *Sci. Rep.*, vol. 6, p. 22136, 2016.

[91] M. Ismail Abdelrahman, C. Rockstuhl, and I. Fernandez-Corbaton, "Broadband suppression of backscattering at optical frequencies using low permittivity dielectric spheres," *Sci. Rep.*, vol. 7, no. 1, p. 14762, 2017.

[92] Y. Zhao, F. Chen, Q. Shen, and L. Zhang, "Optimal structure of light trapping in thin-film solar cells: dielectric nanoparticles or multilayer antireflection coatings?," *Appl. Opt.*, vol. 53, no. 23, p. 5222, 2014.

[93] W. H. Huang *et al.*, "UV-visible light-trapping structure of loosely packed submicrometer silica sphere for amorphous silicon solar cells," *IEEE Electron Device Lett.*, vol. 33, no. 7, pp. 1036–1038, 2012.

[94] Y. H. Fu, A. I. Kuznetsov, A. E. Miroshnichenko, Y. F. Yu, and B. Luk'yanchuk, "Directional visible light scattering by silicon nanoparticles," *Nat. Commun.*, vol. 4, p. 1527, 2013.

[95] S. Person, M. Jain, Z. Lapin, J. J. Sáenz, G. Wicks, and L. Novotny, "Demonstration of zero optical backscattering from single nanoparticles," *Nano Lett.*, vol. 13, no. 4, pp. 1806–1809, 2013.

[96] M. Kerker, D. S. Wang, and C. L. Giles, "Electromagnetic Scattering By Magnetic Spheres.," *J. Opt. Soc. Am.*, vol. 73, no. 6, pp. 765–767, 1983.

[97] A. B. Evlyukhin *et al.*, "Optical spectroscopy of single Si nanocylinders with magnetic and electric resonances," *Sci. Rep.*, vol. 4, pp. 1–7, 2014.

[98] B. S. Luk'Yanchuk, N. V. Voshchinnikov, R. Paniagua-Domínguez, and A. I. Kuznetsov, "Optimum Forward Light Scattering by Spherical and Spheroidal Dielectric Nanoparticles with High Refractive Index," *ACS Photonics*, vol. 2, no. 7, pp. 993–999, 2015.

[99] M. Decker *et al.*, "High-Efficiency Dielectric Huygens' Surfaces," *Adv. Opt. Mater.*, vol. 3, no. 6, pp. 813–820, 2015.

[100] G. C. Papavassiliou, "Optical properties of small inorganic and organic metal particles," *Prog. Solid State Chem.*, vol. 12, no. 3–4, pp. 185–271, 1979.

[101] J. C. M. Garnett and L. Joseph, "VII. Colours in metal glasses, in metallic films, and in metallic solutions.-II," *Philos. Trans. R. Soc. London. Ser. A, Contain. Pap. a Math. or Phys. Character*, vol. 205, pp. 237–288, 1905.

[102] R. Ruppin, "Evaluation of extended Maxwell-Garnett theories," *Opt. Commun.*, vol. 182, pp. 273–279, 2000.

[103] T. Doyle, "Optical properties of a suspension of metal spheres," *Phys. Rev. B*, vol. 39, no. 14, pp. 9852–9858, 1989.

[104] J. Mertz, "Radiative absorption, fluorescence, and scattering of a classical dipole near a lossless interface: a unified description," *J. Opt. Soc. Am. B*, vol. 17, no. 11, pp. 1906–1913, 2000.

[105] K. R. Catchpole and S. Pillai, "Absorption enhancement due to scattering by dipoles into silicon waveguides," *J. Appl. Phys.*, vol. 100, p. 044504, 2006.

[106] K. Kluczyk, C. David, J. Jacak, and W. Jacak, "On Modeling of Plasmon-Induced Enhancement of the Efficiency of Solar Cells Modified by Metallic Nano-Particles," *Nanomaterials*, vol. 9, no. 3, 2019.

[107] V. G. Kravets, S. Neubeck, A. N. Grigorenko, and A. F. Kravets, "Plasmonic blackbody : Strong absorption of light by metal nanoparticles embedded in a dielectric matrix," *Phys. Rev. B*, vol. 81, p. 165401, 2010.

[108] J. Zoroofchi and J. K. Butler, "Refractive index of n -type gallium arsenide," *J. Appl. Phys.*, vol. 44, no. February, p. 3697, 1973.

[109] E. D. Palik, *Handbook of Optical Constants of Solids*. Academic Press, 1998.

[110] A. O. Pinchuk, "Size-Dependent Hamaker Constant for Silver Nanoparticles," *J. Phys. Chem. C*, vol. 116, pp. 20099–20102, 2012.

[111] P. Yu, Y. Yao, J. Wu, X. Niu, A. L. Rogach, and Z. Wang, "Effects of Plasmonic Metal Core-Dielectric Shell Nanoparticles on the Broadband Light Absorption Enhancement in Thin Film Solar Cells," *Sci. Rep.*, vol. 7, no. 1, pp. 1–10, 2017.

[112] C. Sönnichsen, T. Franzl, T. Wilk, G. Von Plessen, and J. Feldmann, "Plasmon resonances in large noble-metal clusters," *New J. Phys.*, vol. 4, no. 111, 2002.

[113] T. L. Temple and D. M. Bagnall, "Optical properties of gold and aluminium nanoparticles for silicon solar cell applications," *J. Appl. Phys.*, vol. 109, no. March, p. 084343, 2011.

[114] C. Langhammer, M. Schwind, B. Kasemo, and I. Zorić, "Localized surface plasmon resonances in aluminum nanodisks," *Nano Lett.*, vol. 8, no. 5, pp. 1461–1471, 2008.

[115] G. H. Chan, J. Zhao, E. M. Hicks, G. C. Schatz, and R. P. Van Duyne, "Plasmonic properties of copper nanoparticles fabricated by nanosphere lithography," *Nano Lett.*, vol. 7, no. 7, pp. 1947–1952, 2007.

[116] F. Leblanc, J. Perrin, and J. Schmitt, "Numerical modeling of the optical properties of hydrogenated amorphous- silicon-based p - i - n solar cells deposited on rough transparent conducting oxide substrates," *J. Appl. Phys.*, vol. 75, p. 1074, 1994.

[117] T. L. Temple, G. D. K. Mahanama, H. S. Reehal, and D. M. Bagnall, "Influence of localized surface plasmon excitation in silver nanoparticles on the performance of silicon solar cells," *Sol. Energy Mater. Sol. Cells*, vol. 93, pp. 1978–1985, 2009.

[118] M. Schmid, R. Klenk, M. C. Lux-steiner, M. Topič, and J. Krč, "Modeling plasmonic scattering combined with thin-film optics," *Nanotechnology*, vol. 22, p. 025204, 2011.

[119] B. J. Soller and D. G. Hall, "Energy transfer at optical frequencies to silicon-based waveguiding structures," *J. Opt. Soc. Am. A*, vol. 18, no. 10, pp. 2577–2584, 2001.

[120] M. J. Mendes, S. Morawiec, F. Simone, F. Priolo, and I. Crupi, "Colloidal plasmonic back reflectors for light trapping in solar cells," *Nanoscale*, vol. 6,

pp. 4796–4805, 2014.

[121] S. Morawiec, M. J. Mendes, S. Mirabella, F. Simone, F. Priolo, and I. Crupi, "Self-assembled silver nanoparticles for plasmon-enhanced solar cell back reflectors: Correlation between structural and optical properties," *Nanotechnology*, vol. 24, p. 265601, 2013.

[122] H. Tan, R. Santbergen, G. Yang, A. H. M. Smets, and M. Zeman, "Combined optical and electrical design of plasmonic back reflector for high-efficiency thin-film silicon solar cells," *IEEE J. Photovoltaics*, vol. 3, no. 1, pp. 53–58, 2013.

[123] C. F. Bohren, "How can a particle absorb more than the light incident on it ?," *Am. J. Phys.*, vol. 51, p. 323, 1983.

[124] M. Z. Jacobson and V. Jadhav, "World estimates of PV optimal tilt angles and ratios of sunlight incident upon tilted and tracked PV panels relative to horizontal panels," *Sol. Energy*, vol. 169, pp. 55–66, 2018.

[125] R. Droste, "MATLAB Central File Exchange, sunRiseSet(lat, lng, UTCoff, date, PLOT)," 2020. [Online]. Available: https://www.mathworks.com/matlabcentral/fileexchange/62180-sunriseset-lat-lng- utcoff-date-plot. [Accessed: 18-Apr-2020].

[126] Jean Meeus, *Astronomical algorithms*, Second Edi. Willmann-Bell, Inc., 1998.

[127] U. Strauss, W. W. Rühle, and K. Köhler, "Auger recombination in intrinsic GaAs," *Appl. Phys. Lett.*, vol. 62, no. 1, pp. 55–57, 1993.

[128] X. Wang, M. R. Khan, J. L. Gray, M. A. Alam, and M. S. Lundstrom, "Design of gaas solar cells operating close to the shockley-queisser limit," *IEEE J. Photovoltaics*, vol. 3, no. 2, pp. 737–744, 2013.

[129] S. M. Ramey and R. Khoie, "Modeling of multiple-quantum-well solar cells including capture, escape, and recombination of photoexcited carriers in quantum wells," *IEEE Trans. Electron Devices*, vol. 50, no. 5, pp. 1179–1188, 2003.

[130] R. E. Welser, O. A. Laboutin, M. Chaplin, and V. Un, "Reducing non-radiative and radiative recombination in InGaAs PL Energy (eV)," *IEEE Photovolt. Spec. Conf.*, pp. 2683–2686, 2011.

[131] D. J. Griffiths, *Introduction to Quantum Mechanics*. Prentice-Hall, Inc., 1995.

[132] K. H. Goetz *et al.*, "Optical and crystallographic properties and impurity incorporation of Ga $_{(x)}$ In $_{(1-x)}$ As (with x between 0. 44 and 0. 49) grown by liquid phase epitaxy, vapor phase epitaxy, and metal organic chemical vapor deposition," *J. Appl. Phys.*, vol. 54, no. August, pp. 4543–4552, 1983.

[133] X. H. Li, P. C. Li, D. Z. Hu, D. M. Schaadt, and E. T. Yu, "Angular dependence of light trapping in $In_{0.3}Ga_{0.7}As$ / GaAs quantum-well solar cells Angular dependence of light trapping in $In_{0.3}Ga_{0.7}As$ / GaAs quantum-well solar cells," *J. Appl. Phys.*, vol. 115, p. 044303, 2014.

[134] S. Rühle, S. Greenwald, E. Koren, and A. Zaban, "Optical waveguide enhanced photovoltaics," *Opt. Express*, vol. 16, no. 26, p. 21801, 2008.

[135] Z. Gai-Ge, J. Jian-Li, X. Feng-Lin, Q. Hai-Xia, W. Hong, and L. Xiang-Yin, "Design of periodic metal-insulator-metal waveguide back structures for the enhancement of light absorption in thin-film solar cells," *Chinese Phys. B*, vol. 20, no. 9, p. 094201, 2011.

[136] B. Mulla and C. Sabah, "Multiband Metamaterial Absorber Design Based on Plasmonic Resonances for Solar Energy Harvesting," *Plasmonics*, vol. 11, pp. 1313–1321, 2016.

ACKNOWLEDGMENTS

First of all, I would like to thank my advisor *Prof. Dr. Daniel M. Schaadt* for his guidance, his motivation, and his continuous support. I admire his insights and his inexhaustible pool of ideas. It was a valuable experience to have the freedom of trying out new ideas. I learned a lot about semiconductor devices (i.e. solar cells) and their components which helped me to overcome my shortcomings.

I also thank *Prof. Dr. Mohammed M. Shabat* for his input in the form of discussion and suggestions during this whole PhD work.

I gratefully acknowledge the financial support of the Ministry of Science and Culture of Lower Saxony, Germany in the form of Georg-Christoph-Lichtenberg Stipend and in the form of conference travel expenses during the initial years of my PhD work (2015 – 2018).

I would like to thank *MSc Sumeet Rohilla* for helping me out in the simulation work and asking me thought-provoking questions about my work which helped me to get a deep insight.

I would like to thank *MSc Waqas Saddique* who became a good friend and with whom I shared ups and downs during my PhD work. I also thank him for having a valuable discussion on semiconductor devices from the materials engineering point of view and introducing me to some experimental techniques (e – beam evaporation, and atomic force microscopy). I thank *MSc Nurhalis Majid* for enjoying coffee with me and having nice discussions on coffee. I also would like to thank all those people whose name is not here, but their presence made this journey easier.

I would like to thank *Ms. Carolina Contreras Soto* for her support during this whole duration and for being always present there to listen to me.

Last but not least, I would like to thank my parents for encouraging me, their continuous support, and their enthusiasm about my PhD.